Modeling Lifetime Performance of Ceramic Matrix Composites with Reduced Order Homogenization Multiscale Methods

Timothy Artz

Submitted in partial fulfillment of the
requirements for the degree of
Doctor of Philosophy
under the Executive Committee
of the Graduate School of Arts and Sciences

COLUMBIA UNIVERSITY

2022

© 2021

Timothy Artz

All Rights Reserved

Abstract

A Unified Approach to Time-Dependent Computational Modeling of Ceramic Matrix Composites at Intermediate and High Temperatures

Timothy Artz

Ceramic Matrix Composites (CMC) are attractive material systems for structural applications where resistance to intermediate (700 ^{0}C-950 ^{0}C) and high temperatures (900 ^{0}C-1400 ^{0}C) is required and low density is desired. There are currently barriers to a more widespread adoption of CMCs which include less robust simulation tools, which this dissertation seeks to address.

A novel unified reduced order homogenization model for initial quasi-static, creep, and fatigue loading of SiC/SiC CMCs at intermediate and high temperatures is proposed. Driven by a single set of parameters, the model can seamlessly transition between initial quasi-static, creep, and fatigue regimes while capturing the complex material response of SiC/SiC CMCs.

The reduced order homogenization approach provides a robust and efficient computational platform for analyzing composite behavior. Continuum damage mechanics provides the basis for the initial brittle CMC behavior while a hybrid damage-viscoplasticity model combined with an oxidation driven crack sealing effect drives the time-dependent brittle-ductile material behavior at high temperatures. A temporal multiscale approach extends the spatial multiscale model into fatigue regime at high temperatures, avoiding the computational complexity of modeling each cycle individually.

At intermediate temperatures, a one-dimensional model based on the slow crack growth model originally proposed by Iyengar and Curtin is generalized to three dimensions focusing on

a woven composite architecture. For this oxidation-assisted rupture model, the constitutive equation in the axial tow direction is governed by the continuum damage mechanics variant of the slow crack-growth model and the availability of oxygen to fibers, which in turn depends on the initial matrix pores and subsequent matrix cracking.

The model is verified on two SiC/SiC material systems, S200H and GEA SMI, in both initial quasi-static and time-dependent loading regimes at both high and intermediate temperatures.

Table of Contents

List of Figures iii
List of Tables v
Acknowledgments vi

Chapter 1: Introduction 1

1.1. Motivation 1
1.2. Ceramic Matrix Composite Behavior and Modeling 2

1.2.1. Time-Independent CMC Behavior and Modeling 2
1.2.2. Time-Dependent Intermediate Temperature CMC Behavior and Modeling 2
1.2.3. Time-Dependent High Temperature CMC Behavior and Modeling 4

1.3. Multiscale Modeling Approach 6
1.4. Experimental Data 6
1.5. S200H and GEA SMI Unidirectional SiC/SiC 8
1.6. Dissertation Outline 9

Chapter 2: Initial Quasi-Static Model 11

2.1. Orthotropic Continuum Damage 11
2.2. Equivalent Strain 13
2.3. Damage Evolution 14
2.4. Stress Update and Consistent Tangent Procedure 16
2.5. Numerical Examples 17

2.5.1. Short Duration Monotonic Tensile Tests for S200H 17
2.5.2. Short Duration Monotonic Tensile Tests for GEA SMI 27

Chapter 3: Oxidation Assisted Damage Model for Intermediate Temperatures 31

3.1. One-Dimensional Strength Degradation Model 31
3.2. One-Dimensional Oxidation Induced Damage Model 32
3.3. Integration of the One-Dimensional Oxidation Induced Damage Model 32
3.4. Generalization of Oxidation Induced Damage Model to Multidimensions 34
3.5. Stress Update and Consistent Tangent Operator 35
3.6. Numerical Examples 36

3.6.1. Uniaxial Tension Single Element Ultimate Time Comparison 36
3.6.2. Stress Rupture Test on a Plate-With-Hole with Varying χ_a Curves 38

Chapter 4: Creep Model for High Temperatures 44

4.1. Hybrid Damage-Viscoplasticity Constitutive Model 44
4.2. Damage Evolution 45

4.3. Viscoplasticity Model 46
4.4. Ductile Failure 46
4.5. Semi-Implicit Stress Update Procedure and Consistent Tangent Operator 47
4.6. High Temperature Crack Sealing and Strength Reduction 49
4.7. Numerical Examples 49
4.7.1. Creep of S200H 49
4.7.2. Creep of GEA SMI 54
Chapter 5: Fatigue Model for High Temperatures 57
5.1. Cycle Blocks 57
5.2. Fatigue Damage Accumulation 59
5.3. Stress Update and Consistent Tangent Operator 60
5.4. Numerical Examples – Fatigue of GEA SMI 63
Chapter 6: Conclusion 68
References 70
Appendix A – Reduced Order Homogenization 81
Appendix B – Model Parameters 87

List of Figures

Figure 1 – S200H eight-harness weave Representative Volume Element (RVE) mesh (matrix partially hidden). Matrix shown in blue, tows in both directions shown in pink and red..... 8

Figure 2- GEA SMI unidirectional fiber RVE mesh. Matrix shown in blue, fiber shown in pink. 9

Figure 3 - S200H featured test specimen..... 18

Figure 4 - Orientation of tows in tension tests..... 19

Figure 5 - Single element UNT loading..... 20

Figure 6 - Featured test finite element mesh and loading..... 20

Figure 7 – S200H 23C $[0,90]_{2s}$ UNT experiment-simulation stress/strain..... 21

Figure 8 – S200H 23C $[+45,-45]_{2s}$ UNT experiment-simulation stress/strain..... 21

Figure 9 – S200H 23C $[0,90]_{2s}$ UNT experiment-simulation for 815C Model stress/strain..... 22

Figure 10 – S200H 23C $[+45,-45]_{2s}$ UNT experiment-simulation for 815C Model stress/strain. 22

Figure 11 – S200H 1200C $[0,90]_{2s}$ UNT experiment-simulation stress/strain..... 23

Figure 12 – S200H 23C $[0,90]_{2s}$ FT experiment-simulation net-section stress vs extensometer displacement..... 23

Figure 13 – S200H 1200C $[0,90]_{2s}$ FT experiment-simulation net-section stress vs extensometer displacement..... 24

Figure 14 - S200H 23C FT DIC of axial surface strain at 100 MPa net-section stress..... 25

Figure 15 - S200H 23C FT simulation of axial surface strain at 100MPa net-section stress..... 25

Figure 16 - S200H 23C FT DIC of axial surface strain just before failure..... 26

Figure 17 - S200H 23C FT simulation of axial surface strain just before failure..... 26

Figure 18 - GEA SMI macroscopic mesh..... 27

Figure 19 – GEA SMI 23C [0,30,60,90]s UNT experiment-simulation stress/strain..... 28

Figure 20 - GEA SMI 1315C [0,30,60,90]s UNT experiment-simulation stress/strain..... 28

Figure 21 - GEA SMI 23C [0,90]2s UNT experiment-simulation stress/strain..... 29

Figure 22 - GEA SMI 1315C [0,90]2s UNT experiment-simulation stress/strain..... 29

Figure 23 - GEA SMI 23C [+45,-45]2s UNT experiment-simulation stress/strain..... 30

Figure 24 - GEA SMI 1315C [+45,-45]2s UNT experiment-simulation stress/strain..... 30

Figure 25 S200H ultimate allowable working time between theoretical and simulated results... 38

Figure 26 – S200H plate with hole macroscopic mesh for stress rupture test..... 39

Figure 27 – S200H 1088K $[0,90]_{2s}$ plate with hole experiment-simulation displacement vs time with varying χ_a 40

Figure 28 - S200H 1088K $[0,90]_{2s}$ tow damage variable ω_1^1 due to oxidation in open hole tension test at (a) 12 hours (b) 48 hours (c) 84 hours (d) 95 hours (e) 97 hours (f) 99 hours (g) 100 hours (h) 102 hours 42

Figure 29 - S200H 1088K $[0,90]_{2s}$ matrix damage variable ω_2^m due to oxidation in open hole tension test at (a) 12 hours (b) 48 hours (c) 84 hours (d) 95 hours (e) 97 hours (f) 99 hours (g) 100 hours (h) 102 hours 43

Figure 30 - S200H 1200C plate with hole specimen 50

Figure 31 - S200H 1200C OHT macroscopic mesh 50

Figure 32 - S200H 1200C $[0,90]_{2s}$ 150MPa creep UNT experiment-simulation strain/time 51

Figure 33 - S200H 1200C $[0,90]_{2s}$ 145MPa creep OHT experiment-simulation strain/time 52

Figure 34 – S200H 1200C $[0,90]_{2s}$ 145 MPa OHT creep 50 hr. interrupted experiment-simulations retained strength stress/strain 53

Figure 35 – S200H 1200C $[0,90]_{2s}$ 145 MPa OHT creep 50 hr. interrupted test retained strength axial surface strain simulation (left) and DIC of specimen (right) at 145MPa of reloading 54

Figure 36 - S200H 1200C $[0,90]_{2s}$ 145 MPa OHT creep 50 hr. interrupted test retained strength axial surface strain simulation (left) and DIC of specimen (right) just before failure..... 54

Figure 37 - GEA SMI 1315C [0,90]2s UNT creep experiment-simulation strain/time 55

Figure 38 -GEA SMI 1315C [0,30,60,90]S 165 MPa UNT creep experiment-simulation strain/time 56

Figure 39 - GEA SMI 1315C [0,30,60,90]S 165 MPa UNT creep 50 hr. interrupted experiment-simulations retained strength stress/strain 56

Figure 40 - Cycle block example 59

Figure 41 - Fatigue stress update procedure 63

Figure 42 - GEA SMI 1315C $[0,90]_{2s}$ 30Hz fatigue simulation-experiment peak stress vs time/cycles to failure..... 64

Figure 43 – GEA SMI double notch fatigue specimen..... 65

Figure 44 – GEA SMI 1315C double notch macroscopic mesh..... 65

Figure 45 - GEA SMI 1315C $[0,30,60,90]_s$ 104MPa DN fatigue experiment-simulation cycle peak extensometer displacement vs. time/cycles. X indicates failure determined by crack extension across specimen. 66

Figure 46 - GEA SMI 1315C $[0,30,60,90]_s$ 104MPa DN interrupted fatigue experiment-simulations retained strength net-section stress vs. extensometer displacement..... 67

List of Tables

Table 1 - S200H FT Specimen Geometry 18
Table 2 – OHT Dimensions 50
Table 3 - DN Dimensions 64
Table 4 - S200H Tow Material Model Parameters 87
Table 5 - S200H Matrix Material Model Parameters 87
Table 6 - GEA SMI Fiber Material Model Parameters 89
Table 7 - GEA SMI Matrix Material Model Parameters 89
Table 8 - GEA SMI Fatigue Model Parameters 90

Acknowledgments

First, I would extend my sincere thanks to Professor Jacob Fish for the many years of guidance and support. I will be forever grateful for the opportunities I was given under his mentorship and the perspective I have gleaned from his scholarship.

I would also thank the other members of my dissertation committee: Professor Steve WaiChing Sun, Professor Haim Waisman, Larry Zawada and Dr. Colin McAuliffe. Their perspectives, time and effort are all greatly appreciated.

For encouraging and inspiring me to pursue this path, I would thank Drs. Stahl, Gilbertsen, Liedtke, Might, Artz, and Friedman.

For endless and eager support, Scott Kelly deserves all of my gratitude.

To the SWC UAW Local 2110 – Solidarity Forever.

My love and appreciation to my parents Colleen and Steve, and my siblings Angie, Arin, Jon, Kristin, Kurt, Laura, and Lea for building me.

The world of CMCs was opened to me by Larry Zawada, Rajesh Kumar, and George Jefferson. For that, as well as enriching correspondence, I thank them.

Untold hours of mentorship, comradery, and teaching occurred in and out of MUDD 642 and I would thank my research group Zifeng, Yang J., David, Dimitrios, Wentao, Innocent, Andrew, Yang Y., Panpan, and Farhad for their kinship.

I would offer a special thanks to my friends Jonathan Russ, Lampros Svolos, and Neslihan Gençkal– without whom I would not have made it this far.

Margaret Artz, your partnership, trust, affirmation, optimism, labor, kindness, and joy give me all.

Chapter 1: Introduction

1.1. Motivation

Ceramic Matrix Composite (CMC) materials have been extensively studied due to their promising characteristics for high temperature structural applications and low density. Stress rupture and creep resistance are critical due to the application of these materials in combustor liners for gas turbine engines [1]–[4], nuclear reactor components [5]–[7], and filters for the energy and chemical industries [8], which require CMC materials maintain these exceptional properties at intermediate (700 ^{0}C-950 ^{0}C) and high (950 ^{0}C-1400 ^{0}C) temperatures over extended periods of time.

The high cost of producing these materials, as well as limited public experimental data, inhibits more widespread adoption and slows development, a recursive problem. Development of robust computational CMC life prediction techniques is necessary to drive down costs and ease adoption.

The purpose of this dissertation is to develop a unified computational approach based on the reduced-order homogenization [9]–[15] that can accurately predict the behavior of SiC/SiC CMCs at intermediate and high temperature under initial quasi-static, creep and fatigue loading. The material model has a single set of parameters defining model behavior that is consistent across all three loading regimes. Model compatibility in the transition between various loading regimes allows mixed loading such as a creep test which can be interrupted sometime before failure, unloaded and reloaded to failure to determine midlife retained strength – all within a single simulation. The creep section of the test could be swapped for a fatigue section seamlessly, with material parameters consistent between analyses. While there are many CMC

models for initial quasi-static, creep, and fatigue analyses, this model's capability to perform all three interchangeably is novel.

1.2. Ceramic Matrix Composite Behavior and Modeling

1.2.1. Time-Independent CMC Behavior and Modeling

There are several approaches to modeling time-independent damage in CMCs. This work was greatly aided by previous efforts to model CMCs using reduced ordered homogenization and continuum damage mechanics as outlined in Kumar et al. as well as Shojaei et al. [16], [17]. Marcin et al. [18] proposed a continuum damage mechanics model based on Helmholtz free energy. Progressive damage analysis with a secant-modulus scheme for the pre-peak nonlinear damage evolution and a smeared crack approach for the post peak softening was demonstrated by Zhang et al. [19]. Kumar [20], Tal and Fish [21] and Skinner et al. [22] developed multiscale models for CMCs that incorporate initial manufacturing defects. Arnold et al., Bednarcyk and Aboudi have done extensive work developing the multiscale generalized method of cells [23]–[25]. Bednarcyk et al. [26] as well as Nemeth et al. [27] have applied this method to time-independent damage in SiC/SiC CMCs.

1.2.2. Time-Dependent Intermediate Temperature CMC Behavior and Modeling

In SiC/SiC composites, oxidation-assisted stress rupture has been observed [28]–[32] at intermediate (700 ^{0}C-950 ^{0}C) temperatures. Oxidation-assisted rupture in CMCs at an intermediate temperature is where severe embrittlement and fracture occur at stresses that are well below their ultimate strength in the pristine state, a phenomenon commonly known as "pesting" [33]–[37]. The present understanding is that embrittlement of fibers occurs due to chemical and thermomechanical processes that ultimately lead to time-dependent stress rupture of SiC fibers [38]–[41]. Various stress rupture models have been proposed. One such model

suggests [34], [42], [43] that oxidation of the BN coating and the formation of silica at the interface causes the fibers to fuse to the matrix and to one another, and consequently, failure of any fused fibers will result in a stress concentration in the nearest intact fiber, making it more likely that the nearest neighbor will also fail. The second model suggests [38], [42] that growth of a silica scale on the fiber surface induces a tensile stress in the SiC fibers, which causes rupture. A third model suggests that oxide growth within a matrix crack may act as a wedge that pries the matrix crack open and ultimately induces a tensile stress in the crack bridging fibers [38]. In the latter two scenarios, the tensile stress in the fibers increases with time and ultimately causes rupture since the magnitude of the tensile stress is a function of the amount of oxide growth. Finally, a fourth model assumes that fiber strength degradation is caused by the slow growth of flaws within the fibers, which is facilitated by oxidation of either SiC or the free carbon at the grain boundaries [44]–[46].

As discussed in the foregoing, a number of modeling approaches are available to model damage and failure of CMC components subjected to mechanical loads. Even so, relatively limited research has been conducted on modeling the oxidation degradation mechanism and its coupling with mechanical damage processes such as matrix cracking. Parthasarathy et al. [47] reviewed various micromechanics-based models for oxidation induced degradation of CMCs and outlined an approach for integrating such models within FEA for component analysis; however, the FE integration was not demonstrated. Similarly, models proposed by Xu et al. [38], Sullivan [40], Gauthier et al. [45] are all one-dimensional models that include specific oxidation mechanisms in detail, but have not been extended for multiaxial stress states suitable for FEA of CMC components. Notable departures from the one-dimensional models for oxidation degradation include the work of Cluzel et al [48] and Genet et al.[49], where oxidation damage is

coupled with mechanical damage state within the context of FEA for component-scale lifetime analysis.

1.2.3. Time-Dependent High Temperature CMC Behavior and Modeling

The present understanding of the primary creep mechanism of SiC/SiC CMCs is load transfer between disparately creep resistant matrix and fiber phases where the less creep resistant phase transfers load to the more creep resistant phase. This induces cracking in the more resistant phase, transferring load back to the less resistant phase furthering creep in that phase. This cycle continues until one of the phases is completely cracked and total rupture occurs [50]–[53]. Under fatigue loading, a similar damage mechanism due to disparate creep resistance has been observed[54], [55]. Oxidation embrittlement has also been observed playing a role in fiber degradation under fatigue[55], [56]. Additionally, it has been found that fiber crushing and delamination due to debonding and fiber sliding as well as shear stress due to nonuniform stress distribution contribute to material degradation under fatigue in woven SiC/SiC CMCs [57]. At high temperatures, cracked SiC/SiC CMCs can undergo crack sealing due to a glassy phase formed by the interphase or oxides such as SiO_2 filling the cracks[31], [58]–[60]. And while the elastic properties of the material with sealed cracks may increase due to cracks closure, the ultimate strength of the CMC may decrease since the glassy phase that fills the cracks is weaker than the parent material [61].

A number of modeling approaches have been proposed to model the behavior of SiC/SiC CMCs under high temperature creep loading. Rugg et al. [50], Almansour et al. [62], and Jing et al. [63] developed one-dimensional micromechanical models of SiC/SiC composites at high temperatures under a creep regime and used these models to successfully investigate micromechanical behavior but did not extend the model to multiaxial stress states suitable for

FEA of CMC components. Khafagy et al. [64] developed a three-dimensional viscoplasticity model with progressive damage and utilized the method of cells to model single fiber SiC/SiC microcomposites. Grujicic et al. [65] developed a single-scale three-dimensional material model that couples a creep-deformation model and creep-rupture model which was demonstrated by modeling the creep deformation and rupture of a gas turbine engine blade. In an extension to their time-independent damage models, Arnold et al., Bednarcyk et al., and Aboudi et al. modeled SiC/SiC CMCs under creep loading utilizing lamination theory and their multiscale generalized method of cells [26], [66], [67] developing tools such as FEAMAC, HyperMAC and HyperSizer to drive analysis as well establishing best practices for tracking material properties and experimental data across temporal and spatial scales.

Similar to high temperature creep, there are a number of phenomenological and one-dimensional models for fatigue such as Lamon et al. [68] with a slow crack growth technique investigating microcomposites and Li Longbiao [69] utilizing a hysteresis energy dissipation based damage model.

Arnold et al. [70] extended the method of cells framework to fatigue analysis of SiC/SiC CMCs, incorporating random microstructures to reflect the disorderly structure common to unidirectional fiber CMCs. Zhang et al. [71] also utilized a method of cells approach with a temporal multiscale jump cycle technique and extended the fatigue analysis to bending of SiC/SiC CMCs. Another multiscale approach to modeling fatigue in CMCs was presented by Zheng et al. [72] based on a sub-model relying on shear lag theory which aligned with experimental results, though the sub-model enhanced macroscale model was presented without experimental verification.

1.3. Multiscale Modeling Approach

At the core of the proposed modelling approach is multiscale modeling based on the reduced order homogenization (ROH) as described in [11]. ROH provides a framework by which microscale composite constituent behavior can be upscaled to the macroscale at a fraction of computational cost that would be required by the direct computational homogenization approach that fully resolves microstructural details. The salient feature of ROH is that it coincides with the direct computational homogenization approach in the linear elastic regime, whereas in the inelastic regime it effectively substitutes finite element nodal degrees of freedom with a degree of freedom of a phase eigenstrain that describes an average that enforces equilibrium equation at a level of each phase. This is accomplished by assuming that an eigenstrain in each phase is constant. Computational cost of multiscale simulations can be further reduced using a so-called pseudo-nonlocal finite element formulation that employs reduced integration for stress updates but full integration for element matrices (residual and its consistent tangent stiffness) [73]. Further details on this scheme can be found in [11], [15] as well as in Appendix A. With the ROH framework providing a platform by which the composite behavior is modeled, individual phase constitutive behavior must be determined to complete the material modeling.

1.4. Experimental Data

Much of the research for this dissertation was conducted as part of the Enhanced Physics-Based Prognosis and Inspection of CMCs (EPPIC) program which was conducted to investigate the state-of-the-art in the lifing of CMCs as described in Jefferson et al [74]. Under the program, an array of CMC lifing experiments were performed and blind simulations of these experiments were conducted. The numerical examples in this dissertation represent the simulation of both calibration experiments provided to participating modeling teams to drive their blind predictions,

and the novel experiments performed as part of the program. None of the numerical examples included represent the blind predictions performed as part of the program as the material models were updated and improved both during the program and after its conclusion.

The experiments performed as part of the EPPIC program were conducted on the woven S200H and the unidirectional GEA SMI material systems. One of the most impactful challenges facing CMC model development is the relative rapidity with which CMC material system manufacturing changes over time. Individual manufacturers of a material system might change the way a fiber coating for that system is produced, significantly affecting the material response, but the manufacturer will continue to identify the material system with the same nomenclature. It is common to find sets of experimental data regarding what is purportedly the same material with significantly different material responses under similar conditions due to changes in manufacturing techniques which may or may not be reported. An effort has been made in this experimental validation to compare material systems with as similar material response as possible. Testing performed as part of the EPPIC program provided experimental results across initial quasi-static, high temperature creep, and high temperature fatigue loading regimes with specimens produced from the same CMC panels guaranteeing consistent material system response. This allows validation of the described material modeling scheme across these loading regimes.

Experimental data for intermediate temperatures was initially provided prior to the EPPIC program but was also included in the program's calibration data. Due to limited experimental data at intermediate temperatures, there was not an opportunity to model transitions between loading regimes at intermediate temperatures. While this capability is possible for the model, it has not been validated.

As part of the EPPIC program, a model for fatigue at intermediate temperatures based on the oxidation-assisted slow crack growth model described in Chapter 3 was developed and utilized for the blind prediction portion of the program. However, due to various challenges including the COVID-19 pandemic and material systems that are difficult to perform these complex experiments on reliably, experimental data sufficient to validate the intermediate temperature fatigue model was unavailable to include in this dissertation.

1.5. S200H and GEA SMI Unidirectional SiC/SiC

To demonstrate the capabilities of the material models presented, simulations are performed on two SiC/SiC CMC systems. The S200H material system consists of Hi-Nicalon^{TM} fiber tows woven in an 8-harness satin weave architecture and coated with a BN/Si3N4 interface coating. The matrix consists of Si, N, and C derived via Polymer Impregnation and Pyrolysis (PIP) process. In the PIP process the ceramic matrix is formed by multiple cycles of impregnation of the fiber preform with pre-ceramic polymer followed by pyrolysis. The PIP cycles are continued until a dense composite with open porosity of less than 10-15% is achieved. An idealized unit cell of this composite is shown in Figure 1.

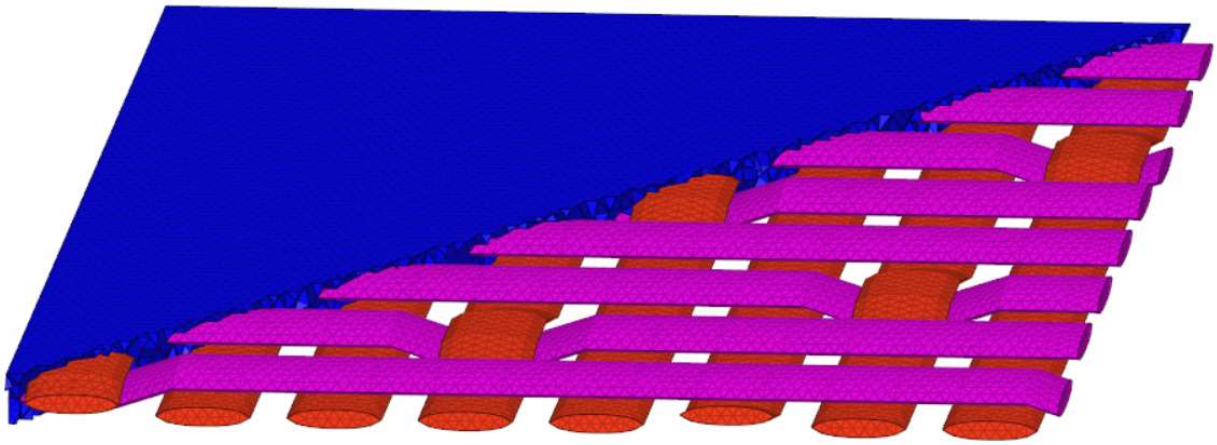

Figure 1 – S200H eight-harness weave Representative Volume Element (RVE) mesh (matrix partially hidden). Matrix shown in blue, tows in both directions shown in pink and red.

The second material system employed is the GE Aviation Silicon Melt Infiltrated SiC/SiC (GEA SMI) which consists of unidirectional boron nitride coated Hi-Nicalon^{TM} fiber passed through a SiC slurry for pre-infiltration and dried to create a tape that is stacked in custom orientations and melt infiltrated with liquid silicon to form the matrix. Further description of this material system can be found in [75] and limited durability testing can be found in [76], [77]. An idealized RVE of this composite is shown in Figure 2.

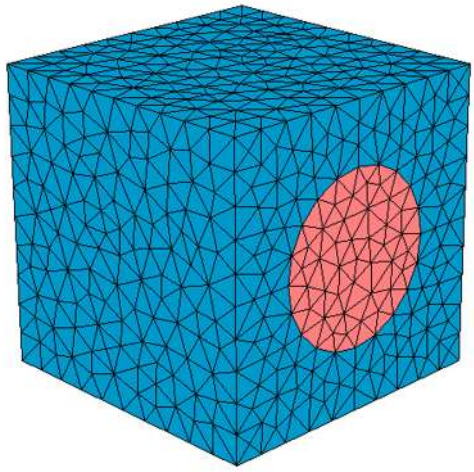

Figure 2- GEA SMI unidirectional fiber RVE mesh. Matrix shown in blue, fiber shown in pink.

1.6. Dissertation Outline

The remainder of this dissertation describes the development of the phase constitutive models that are implemented within the ROH modeling approach. These phase constitutive models are interlinked in the sense that the fatigue model is an extension of the creep model, which in turn is an extension of the initial quasi-static model. Chapter 2 describes the model in the initial quasi-static regime, where an orthotropic continuum damage model provides the baseline time-independent damage model upon which the subsequent time-dependent models are

built. In Chapter 3, the time-dependent oxidation assisted damage model for intermediate temperatures is developed. Chapter 4 contains the time-dependent hybrid damage-viscoplasticity model for high temperature creep. Chapter 5 extends this hybrid model into the fatigue regime with a computationally efficient cycle block system as well as an additional fatigue damage mechanism. Chapters 2-5 each contain numerical examples which utilize the experimental data described in Section 1.4. Chapter 6 contains conclusions with a summary of the work presented as well as thoughts on future work in CMC modeling. Finally, Appendix A contains a more detailed explanation of ROH and Appendix B contains the material model parameters used in the validation simulations.

Chapter 2: Initial Quasi-Static Model

The initial quasi-static phase constitutive model describes the time-independent behavior of the phases. This model is utilized in time-independent simulations such as simulating the uniaxial tension test as well as initial quasi-static stages of time-dependent simulations. It forms the basis for a brittle portion of the hybrid ductile-brittle time-dependent phase behavior.

2.1. Orthotropic Continuum Damage

Herein, we consider a variant of an orthotropic continuum damage model proposed by Chow and Wang [9]. An orthotropic damage tensor $W_{ijkl}\left(\omega_I\right)$ expressed in terms of damage parameters $\omega_I \in [0,1]$ where $I = 1,2,3$ represent the local material direction, is introduced to relate effective $\tilde{\sigma}_{ij}$ and microstructural σ_{kl} stresses as

$$\tilde{\sigma}_{ij} = W_{ijkl}\left(\omega_I\right)\sigma_{kl} \tag{1}$$

where the fourth order damage tensor in Voigt notation, $\left[W_{ijkl}\right]$, is a diagonal matrix

$$\left[W_{ijkl}\right] = \begin{bmatrix} \sqrt{1-\omega_1} & & & & & \\ & \sqrt{1-\omega_2} & & & & \\ & & \sqrt{1-\omega_3} & & & \\ & & & \sqrt[4]{1-\omega_2}\sqrt[4]{1-\omega_3} & & \\ & & & & \sqrt[4]{1-\omega_1}\sqrt[4]{1-\omega_3} & \\ & & & & & \sqrt[4]{1-\omega_1}\sqrt[4]{1-\omega_2} \end{bmatrix} \tag{2}$$

To construct the coarse-scale constitutive equations, Lemaitre and Chaboche [78] proposed to employ the postulate of strain equivalence, which leads to asymmetry of the stiffness matrix when anisotropic damage is considered. To obtain the symmetric form, we adopt herein the Sidoroff postulate [79] of elastic energy density equivalence

$$\Phi = \tilde{\sigma}_{ij}\left(L_{ijkl}\right)^{-1}\tilde{\sigma}_{kl} = \sigma_{ij}\left(L^{in}_{ijkl}\right)^{-1}\sigma_{kl} \tag{3}$$

that leads to the symmetric stress-strain relation

$$\varepsilon_{ij} = \frac{\partial \Phi}{\partial \sigma_{in}} = \left(L^{in}_{ijmn} \right)^{-1} \sigma_{mn}$$
$$L^{in}_{ijmn} = W_{ijkl} L_{klpq} W_{mnpq} \tag{4}$$

where L_{klpq} and $L^{in}_{ijmn}\left(\omega_I\right)$ are the fourth-order anisotropic constitutive tensor for elastic crack-free material and damage-induced material. The undamaged orthotropic elastic tensor in the matrix form denoted as $\mathbf{L}$ has the following non-zero terms

$$\mathbf{L} = \begin{bmatrix} L_{11} & L_{12} & L_{13} & & & \\ L_{21} & L_{22} & L_{23} & & & \\ L_{31} & L_{32} & L_{33} & & & \\ & & & L_{44} & & \\ & & & & L_{55} & \\ & & & & & L_{66} \end{bmatrix} \tag{5}$$

From (4) the non-zero terms of the damage-induced constitutive tensor in matrix form $\mathbf{L}^{in}$ are given as

$$\mathbf{L}^{in} = \begin{bmatrix} (1-\omega_1)L_{11} & \sqrt{1-\omega_1}\sqrt{1-\omega_2}L_{12} & \sqrt{1-\omega_1}\sqrt{1-\omega_3}L_{13} & & & \\ \sqrt{1-\omega_1}\sqrt{1-\omega_2}L_{21} & (1-\omega_2)L_{22} & \sqrt{1-\omega_2}\sqrt{1-\omega_3}L_{23} & & & \\ \sqrt{1-\omega_1}\sqrt{1-\omega_3}L_{31} & \sqrt{1-\omega_2}\sqrt{1-\omega_3}L_{32} & (1-\omega_3)L_{33} & & & \\ & & & \sqrt{1-\omega_2}\sqrt{1-\omega_3}L_{44} & & \\ & & & & \sqrt{1-\omega_1}\sqrt{1-\omega_3}L_{55} & \\ & & & & & \sqrt{1-\omega_1}\sqrt{1-\omega_2}L_{66} \end{bmatrix} \tag{6}$$

For thermodynamical consistency, the evolution of damage parameters is given in terms of thermodynamic forces conjugated to their respective damage variables

$$Y_I = \frac{\partial \Phi}{\partial \omega_I} \geq 0 \tag{7}$$

where it can be shown that $Y_1 = Y_1\left(\varepsilon_{11}, \varepsilon_{12}, \varepsilon_{13}\right)$, $Y_2 = Y_2\left(\varepsilon_{22}, \varepsilon_{12}, \varepsilon_{23}\right)$ and $Y_3 = Y_3\left(\varepsilon_{33}, \varepsilon_{13}, \varepsilon_{23}\right)$.

Damage growth is controlled by the damage loading functions

$$f_I\left(\tilde{\varepsilon}_I,\kappa_I\right)=\tilde{\varepsilon}_I-\kappa_I \tag{8}$$

where κ_I are the history dependent parameters which reflect the loading history and $\tilde{\varepsilon}_I$ are the corresponding equivalent strains. The history parameters κ_I range from initial values $\kappa_I^{\,0}$ where damage initiates and grow by memorizing the maximum values of the corresponding effective strains $\tilde{\varepsilon}_I$. The structure of the loading function can, just as for plasticity, be formalized using the Kuhn-Tucker conditions

$$f_I\le 0,\ \ \kappa_I\ge 0,\ \ f_I\kappa_I=0 \tag{9}$$

An alternative, which has not been pursued herein, is to consider an isotropic damage model for the matrix phase by inserting $\omega_1=\omega_2=\omega_3=\omega$ in (6) in which case the thermodynamic force (and thus equivalent strain) conjugate with a single damage variable would be a function of six strain components [80].

2.2. Equivalent Strain

The equivalent strains are defined similarly to the isotropic damage model proposed by Mazars [80]

$$\begin{aligned}
\tilde{\varepsilon}_1&=\sqrt{\sum_{N=1}^{3}\left\langle\varepsilon_N\left(\varepsilon_{11},c_{12}\varepsilon_{12},c_{13}\varepsilon_{13}\right)\right\rangle^2}\\
\tilde{\varepsilon}_2&=\sqrt{\sum_{N=1}^{3}\left\langle\varepsilon_N\left(\varepsilon_{22},c_{12}\varepsilon_{12},c_{23}\varepsilon_{23}\right)\right\rangle^2}\\
\tilde{\varepsilon}_3&=\sqrt{\sum_{N=1}^{3}\left\langle\varepsilon_N\left(\varepsilon_{33},c_{23}\varepsilon_{23},c_{13}\varepsilon_{13}\right)\right\rangle^2}
\end{aligned} \tag{10}$$

where $c_{12}>1, c_{13}>1,\ c_{23}>1$ are shear correction factors, material constants introduced to weight shear contributions to damage; $\langle x\rangle=x$ if $x>0$ and $\langle x\rangle=0$ otherwise; $\varepsilon_N\left(A,B,C\right)$ denotes

eigenvalues of the symmetric second-order strain tensor with A,B,C being the only nonzero matrix terms

$$\begin{bmatrix} A & B & C \\ B & 0 & 0 \\ C & 0 & 0 \end{bmatrix}, \begin{bmatrix} 0 & B & 0 \\ B & A & C \\ 0 & C & 0 \end{bmatrix}, \begin{bmatrix} 0 & 0 & C \\ 0 & 0 & B \\ C & B & A \end{bmatrix} \tag{11}$$

It is instructive to point out that the above matrices have one zero eigenvalue, one negative eigenvalue and one positive eigenvalue given as

$$\frac{A+\sqrt{A^2+4\left(B^2+C^2\right)}}{2}>0 \tag{12}$$

Taking advantage of (12), the equivalent effective strains can then be written in the close form as

$$\begin{aligned} \tilde{\varepsilon}_1 &= \frac{1}{2}\left(\varepsilon_{11}+\sqrt{{\varepsilon_{11}}^2+4\left(c_{12}{\varepsilon_{12}}^2+c_{13}{\varepsilon_{13}}^2\right)}\right) \\ \tilde{\varepsilon}_2 &= \frac{1}{2}\left(\varepsilon_{22}+\sqrt{{\varepsilon_{22}}^2+4\left(c_{12}{\varepsilon_{12}}^2+c_{23}{\varepsilon_{23}}^2\right)}\right) \\ \tilde{\varepsilon}_3 &= \frac{1}{2}\left(\varepsilon_{33}+\sqrt{{\varepsilon_{33}}^2+4\left(c_{13}{\varepsilon_{13}}^2+c_{23}{\varepsilon_{23}}^2\right)}\right) \end{aligned} \tag{13}$$

The model outlined in this section represents a computational enhancement in terms of speed and stability of the previously model developed in [16], [81] where the material coordinate system that detects the pattern of initial cracking is computed first and the progression of damage is then evolved in that material coordinate system. That model requires calculation of principal directions at each load increment/iteration and rotation from and to the material coordinated system.

2.3. Damage Evolution

Following [15], damage growth is defined with the damage evolution and loading history variable such that:

$$\omega_I = {}^eG_I\left(\kappa_I\right) \tag{14}$$

where κ_I is the history dependent damage threshold which reflects the loading history for each material direction. The damage threshold κ_I grows by memorializing the maximum value of the corresponding equivalent strain $\tilde{\varepsilon}_I$ at any material point. The damage threshold κ_I does not decrease so its rate $\dot{\kappa}_I$ is strictly positive.

The continuous piecewise linear damage function ${}^eG_I\left(\tilde{\varepsilon}_I\right)$ defines a simple damage to equivalent strain relation using a list of stress/strain points $(\bar{\varepsilon}^k, \bar{\sigma}^k)$ and a maximum allowable damage $\omega_{\max}$ which define a linear evolution:

$${}^eG_I(\tilde{\varepsilon}_I) = \begin{cases} 0, & \tilde{\varepsilon}_I \le \bar{\varepsilon}_I^0 \\ {}^eG_I^1(\tilde{\varepsilon}_I), & \bar{\varepsilon}_I^0 < \tilde{\varepsilon}_I \le \bar{\varepsilon}_I^1 \\ {}^eG_I^2(\tilde{\varepsilon}_I), & \bar{\varepsilon}_I^1 < \tilde{\varepsilon}_I \le \bar{\varepsilon}_I^2 \\ \cdots & \\ {}^eG_I^n(\tilde{\varepsilon}_I) & \bar{\varepsilon}_I^{n-1} < \tilde{\varepsilon}_I \le \bar{\varepsilon}_I^n \\ \omega_{\max} & \bar{\varepsilon}_I^n < \tilde{\varepsilon}_I \end{cases} \tag{15}$$

where:

$${}^eG_I^k(\tilde{\varepsilon}_I) = \frac{\hat{\varepsilon}_I^{k-1}}{\bar{\varepsilon}_I^{k-1}} + \left(\frac{\hat{\varepsilon}_I^k}{\bar{\varepsilon}_I^k} - \frac{\hat{\varepsilon}_I^{k-1}}{\bar{\varepsilon}_I^{k-1}}\right)\frac{1/\tilde{\varepsilon}_I - 1/\bar{\varepsilon}_I^{k-1}}{1/\bar{\varepsilon}_I^k - 1/\bar{\varepsilon}_I^{k-1}} \tag{16}$$

$$\hat{\varepsilon}_I^k = \bar{\varepsilon}_I^k - \bar{\sigma}_I^k / L_{II} \tag{17}$$

The maximum allowable damage parameter is included for numerical stability and is a value just below 1 which represents total failure. The damage evolution law is flexible and can be adapted to use cases as needed. In modeling CMCs, the damage function for the matrix phase is isotropic while the damage functions for tows and fibers is transverse isotropic.

A viscous stabilization method generalized from Duvaut and Lions [82] is also employed in the damage evolution for numerical stability:

$$\dot{\omega}_I = \frac{1}{\eta}\left(\omega_I^{inv} - \omega_I\right) \tag{18}$$

where ω_I^{inv} is the inviscid damage before any viscous regularization has been performed, and η is the viscosity coefficient defining the relaxation time.

Backward Euler integration of (18) yields

$${}_{n+1}\omega_I = \beta\, {}_{n+1}\omega_I^{inv} + \left(1-\beta\right) {}_n\omega_I \tag{19}$$

where

$$\beta = \frac{\Delta t}{\eta + \Delta t} \tag{20}$$

For initial quasi-static simulations considered herein β is chosen directly as 0.87.

2.4. Stress Update and Consistent Tangent Procedure

Given phase strain ${}_{n+1}\varepsilon_{ij}$ and state variables ${}_n\kappa_I$

1. Compute equivalent strain:

$$\begin{aligned}
\tilde{\varepsilon}_1 &= \frac{1}{2}\left({}_{n+1}\varepsilon_{11} + \sqrt{{}_{n+1}\varepsilon_{11}{}^2 + 4\left(c_{12}\, {}_{n+1}\varepsilon_{12}{}^2 + c_{13}\, {}_{n+1}\varepsilon_{13}{}^2\right)}\right) \\
\tilde{\varepsilon}_2 &= \frac{1}{2}\left({}_{n+1}\varepsilon_{22} + \sqrt{{}_{n+1}\varepsilon_{22}{}^2 + 4\left(c_{12}\, {}_{n+1}\varepsilon_{12}{}^2 + c_{23}\, {}_{n+1}\varepsilon_{23}{}^2\right)}\right) \\
\tilde{\varepsilon}_3 &= \frac{1}{2}\left({}_{n+1}\varepsilon_{33} + \sqrt{{}_{n+1}\varepsilon_{33}{}^2 + 4\left(c_{13}\, {}_{n+1}\varepsilon_{13}{}^2 + c_{23}\, {}_{n+1}\varepsilon_{23}{}^2\right)}\right)
\end{aligned} \tag{21}$$

2. Update maximum equivalent strain:

$${}_{n+1}\kappa_I = \max({}_n\kappa_I, \tilde{\varepsilon}_I) \tag{22}$$

3. Compute damage variable and apply viscous stabilization:

$${}_{n+1}\omega_I = \beta\, {}_{n+1}{}^eG_I\left({}_{n+1}\kappa_I\right) + \left(1-\beta\right) {}_n\omega_I \tag{23}$$

4. Calculate damage-induced constitutive matrix L_{ijkl}^{in} per equation (6). L_{ijkl}^{in} is also used as the consistent tangent.

5. Update stress:

$${}_{n+1}\sigma_{ij} = {}_{n+1}\, L_{klmn}^{in}\, {}_{n+1}\varepsilon_{ij} \tag{24}$$

2.5. Numerical Examples

The methods described in the preceding sections are demonstrated here by modeling experiments in the initial quasi-static regime.

Simulations of the experiments are performed using a combination of Altair Multiscale Designer (MDS) [83] and Finite Element Solver in Object Oriented Fortran (FOOF) [84]. Precomputation of the influence functions (see Appendix A) which provide relations between the coarse-scale strain, eigenstrain, and microstructural phases is performed in MDS. The inputs to this computation include the RVE geometry and elastic properties of the microstructure phases. These influence functions are then imported into FOOF where nonlinear analysis with the described phase material models is performed.

For the development of the reduced order model, an RVE is developed with MDS where the geometry is described by parameters developed from physical specimens. For S200H, these parameters are an elliptical tow major radius of 0.0152, minor radius of 0.00315, tow spacing of 0.0421 and tow volume fraction of 42%. The resulting RVE mesh can be seen in **Figure 1**. As the material is a unidirectional fiber, the only parameter for the RVE of GEA SMI depicted in **Figure 2** is the fiber volume fraction of 0.25. Note that the dimensions of the RVE parameters are unitless as the dimensions of the RVE do not have any effect on the solution.

2.5.1. Short Duration Monotonic Tensile Tests for S200H

Short duration monotonic tensile experiments available for the S200H material system include unnotched tension tests (UNT) and featured tension tests (FT). The FT consists of a uniaxial tension test with two small holes as shown in **Figure 3** where the test specimen's dimensions are presented in **Table 1**.

Table 1 - S200H FT Specimen Geometry

	mm
Length	150
Width	14
Radius	317
Hole Diameter	2
Lengthwise Hole Center	3
Widthwise Hole Center	3
Hole Center to Edge	3.5
Thickness	2.3

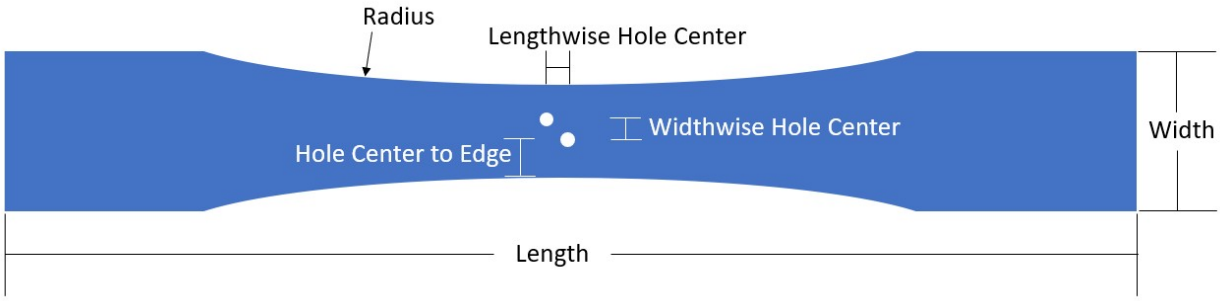

Figure 3 - S200H featured test specimen

The tests include UNT and FT with an $[0,90]_{2s}$ layup at 23°C and 1200°C as well as UNT with a $[+45,-45]_{2s}$ layup at 23°C. The $[0,90]_{2s}$ and $[+45,-45]_{2s}$ layups are arranged with the tow angles oriented with respect to the direction of loading is shown in **Figure 4**:

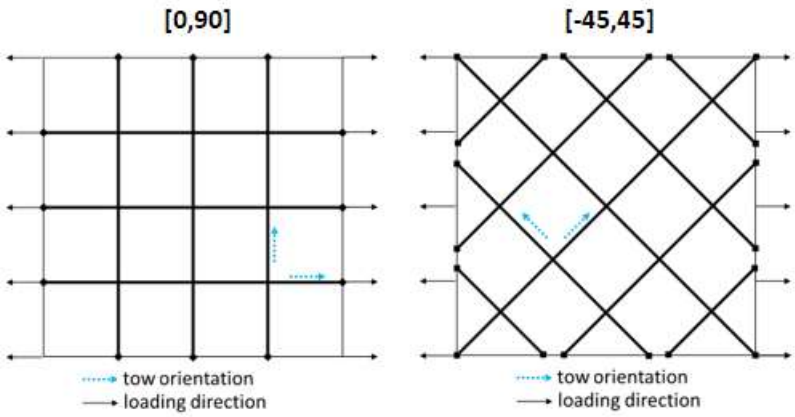

Figure 4 - Orientation of tows in tension tests

Tests at 23°C are not high temperature, but are considered to demonstrate the effectiveness of the initial quasi-static model at a wide range of temperatures. Due to limited data availability, room temperature tests were used to calibrate the quasi-static behavior for the 815°C model which is further explored in Chapter 3. Additionally, there are tests featured in Chapters 4 and 5 where a specimen is held under a creep or fatigue load at high load temperatures, unloaded and then reloaded at room temperature where room temperature behavior is important. There are four sets of data that the experimental data is pulled from which are referenced by year conducted. The 2020 experiments were conducted for the EPPIC program and include the FT. The 2018 experiments are comprised of $[0,90]_{2s}$ UNT that are the closest in material system composition to the 2020 experiments. The 2011 experiments contain $[0,90]_{2s}$ and $[+45,-45]_{2s}$ UNT at 23°C. The 2015 experiments contain $[0,90]_{2s}$ and $[+45,-45]_{2s}$ UNT at 23°C but are utilized for the 815°C material model.

The macroscopic finite element mesh for the UNT consists of a single 8-node hexahedron element mesh that is symmetrically constrained on an x, y, and z face with traction applied on the x face opposite the constraint as shown in **Figure 5**.

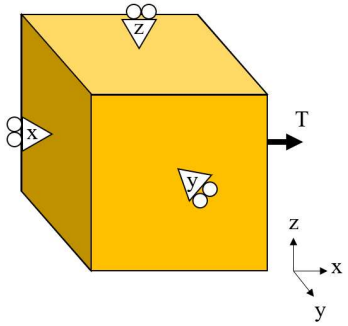

Figure 5 - Single element UNT loading

The macroscopic finite element mesh for the FT is also meshed with 8-node hexahedrons and is shown in **Figure 6**. An x face is constrained in x with its lower edge begin constrained in z and an outer edge constrained in y while traction is applied to the opposite x face. The stress vs strain curves for the simulation-experiment comparisons of the UNT can be seen in **Figure 7** - **Figure 12**.

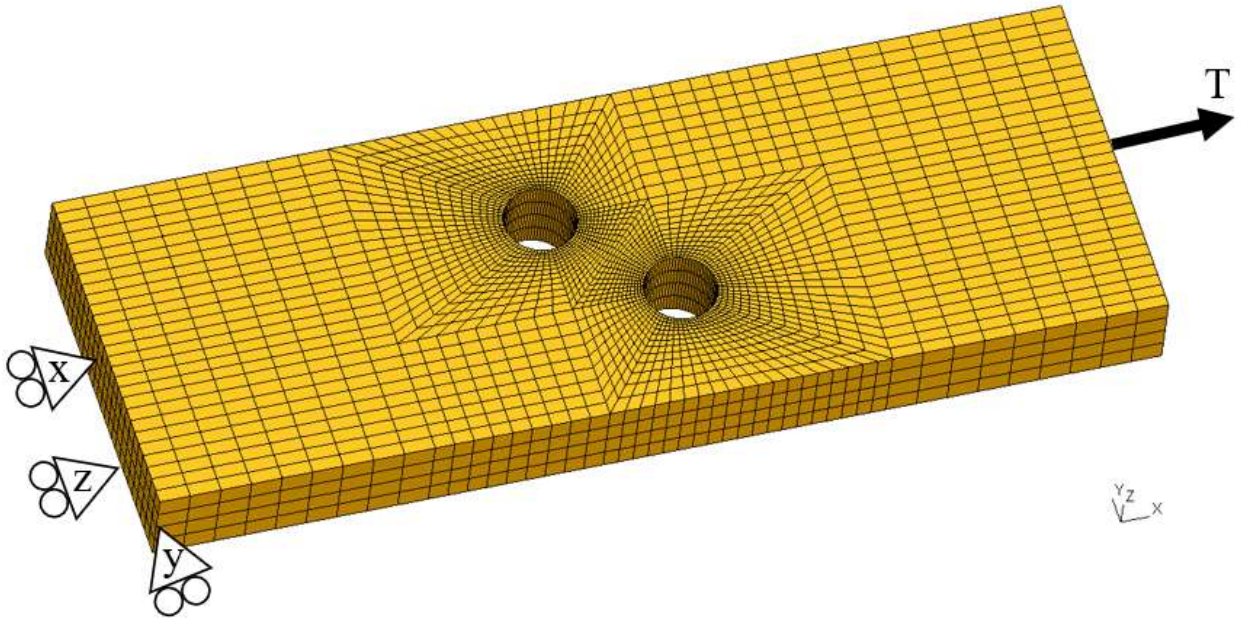

Figure 6 - Featured test finite element mesh and loading

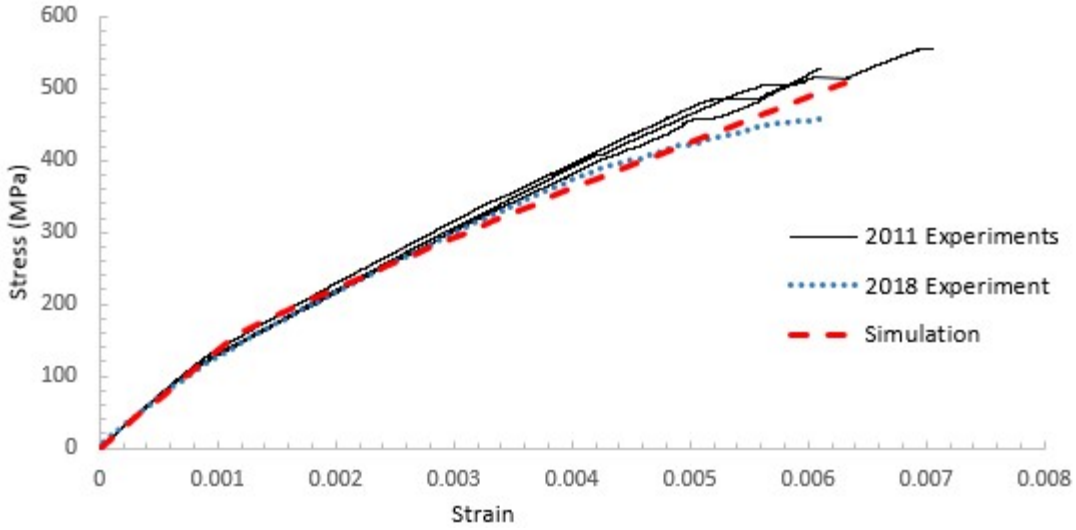

Figure 7 – S200H 23C $[0,90]_{2s}$ UNT experiment-simulation stress/strain

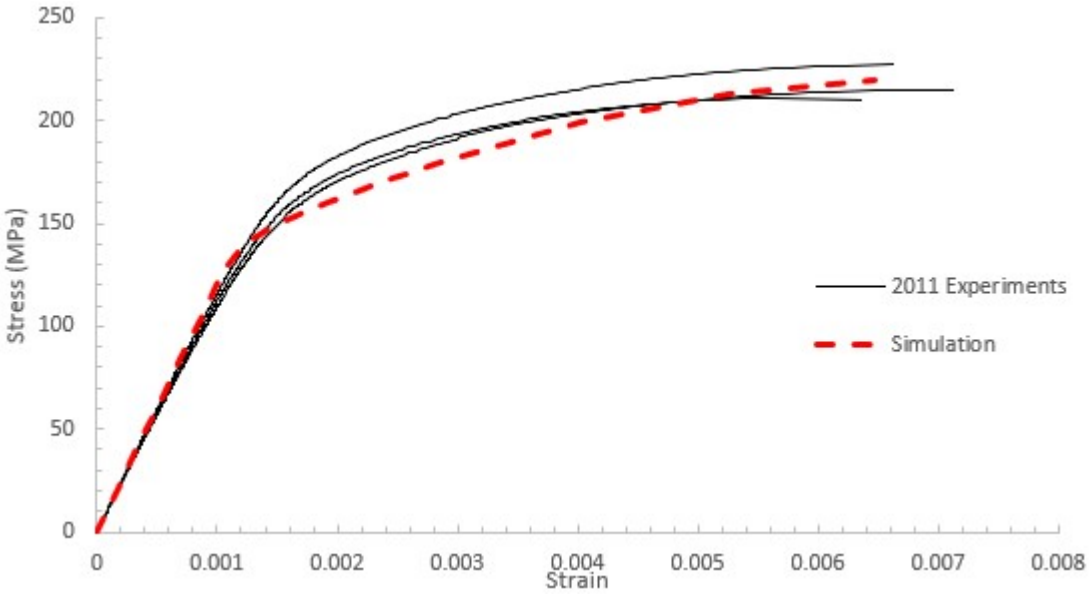

Figure 8 – S200H 23C $[+45,-45]_{2s}$ UNT experiment-simulation stress/strain

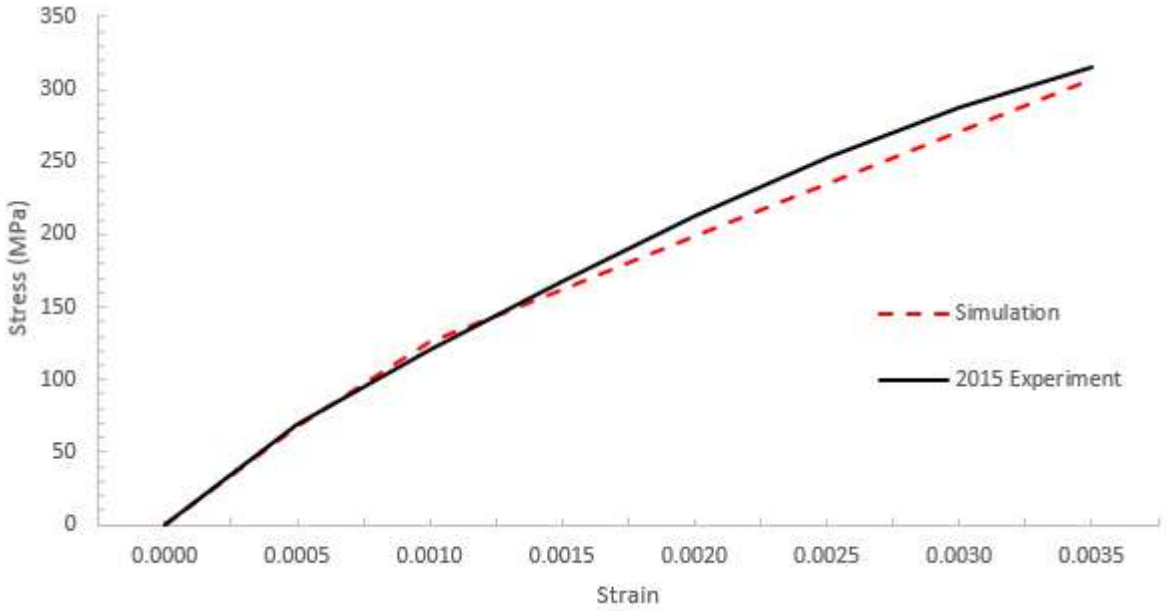

Figure 9 – S200H 23C $[0,90]_{2s}$ UNT experiment-simulation for 815C Model stress/strain

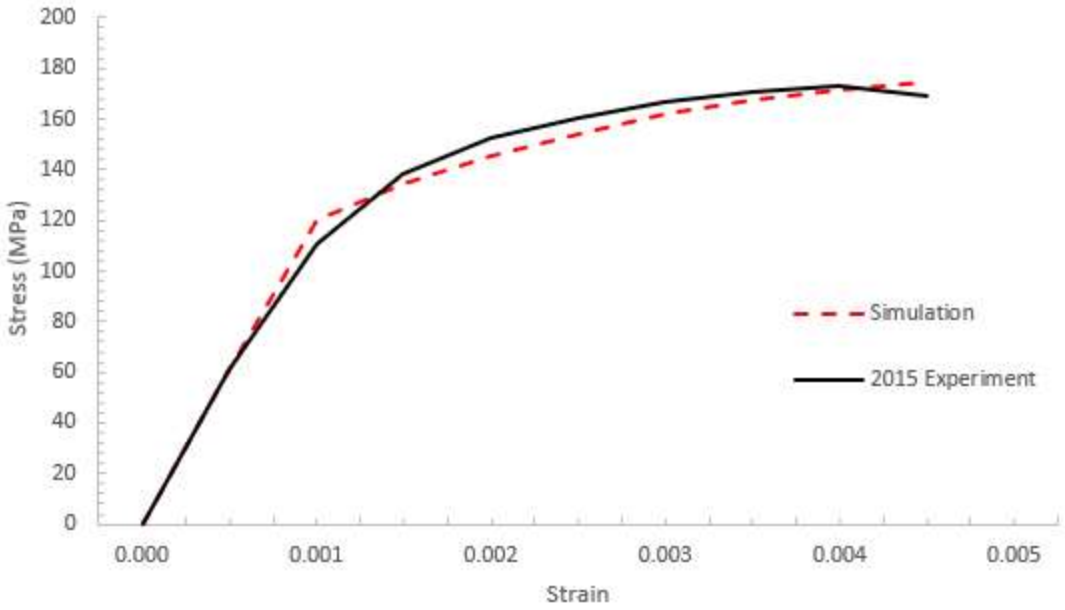

Figure 10 – S200H 23C $[+45,-45]_{2s}$ UNT experiment-simulation for 815C Model stress/strain

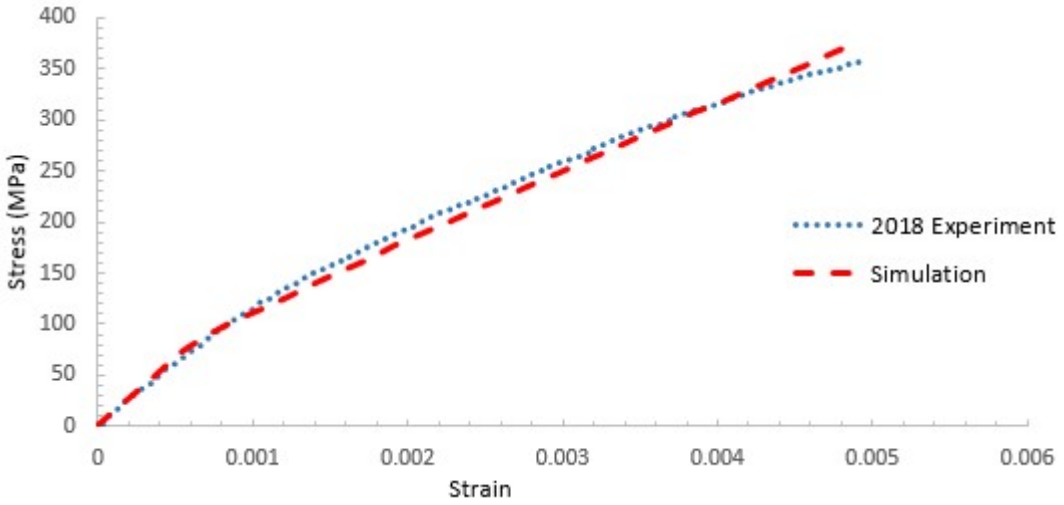

Figure 11 – S200H 1200C $[0,90]_{2s}$ UNT experiment-simulation stress/strain

For the FT, a 12.5mm extensometer was placed at the center of the machined edge of the specimen. A plot of the net-section stress of a cross section including one of the holes vs. the extensometer displacement is provided in **Figure 12-Figure 13**

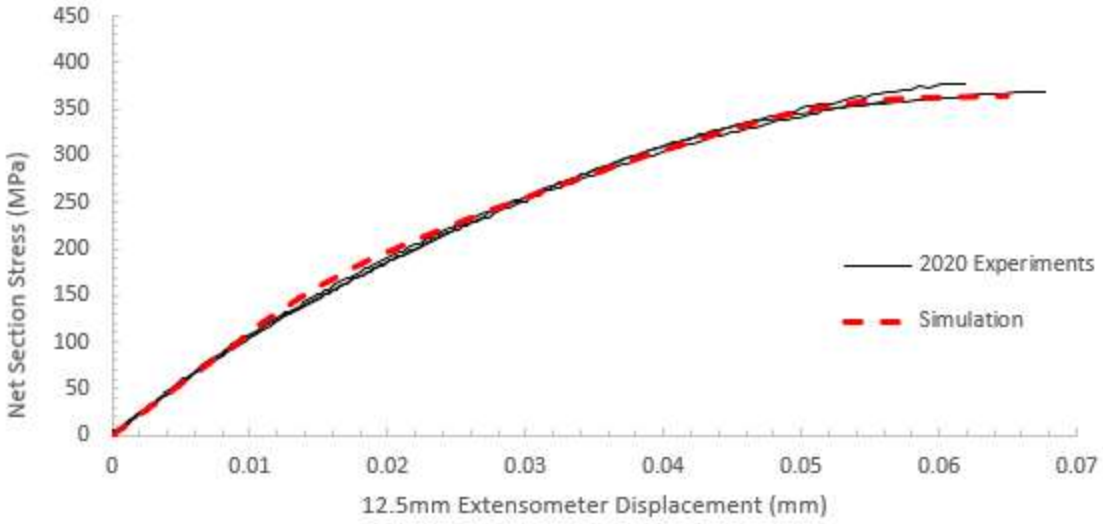

Figure 12 – S200H 23C $[0,90]_{2s}$ FT experiment-simulation net-section stress vs extensometer displacement

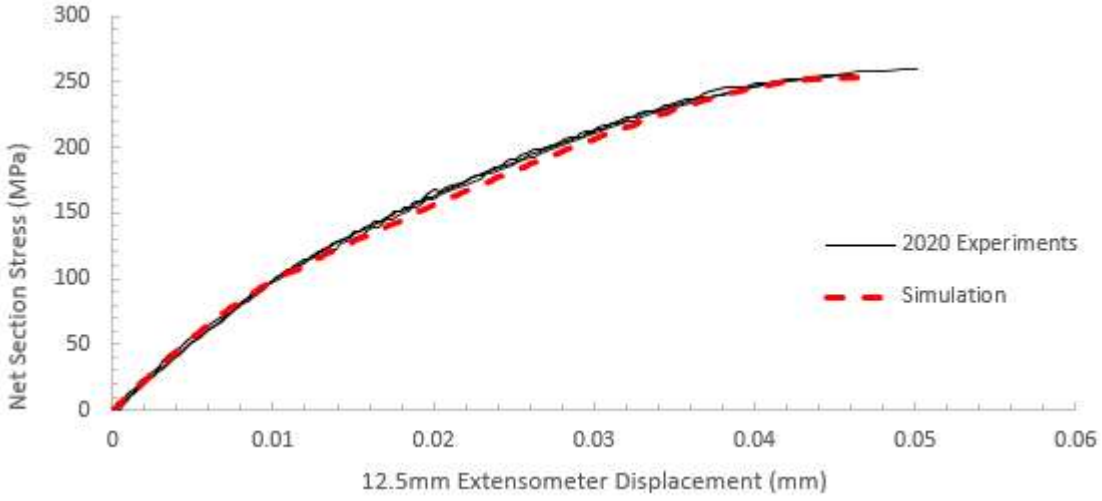

Figure 13 – S200H 1200C $[0,90]_{2s}$ FT experiment-simulation net-section stress vs extensometer displacement

At 23°C, Digital Image Correlation (DIC) was used to measure the axial surface strain of the FT specimen while it was loaded. DIC at 100 MPa Net-Section Stress, is shown in **Figure 14**. The simulation axial surface strain at the same Net-Section Stress is displayed in **Figure 15**. Similarly, **Figure 16** - **Figure 17** show the DIC and simulation surface strain just before failure. There is no DIC data available for the high temperature specimen.

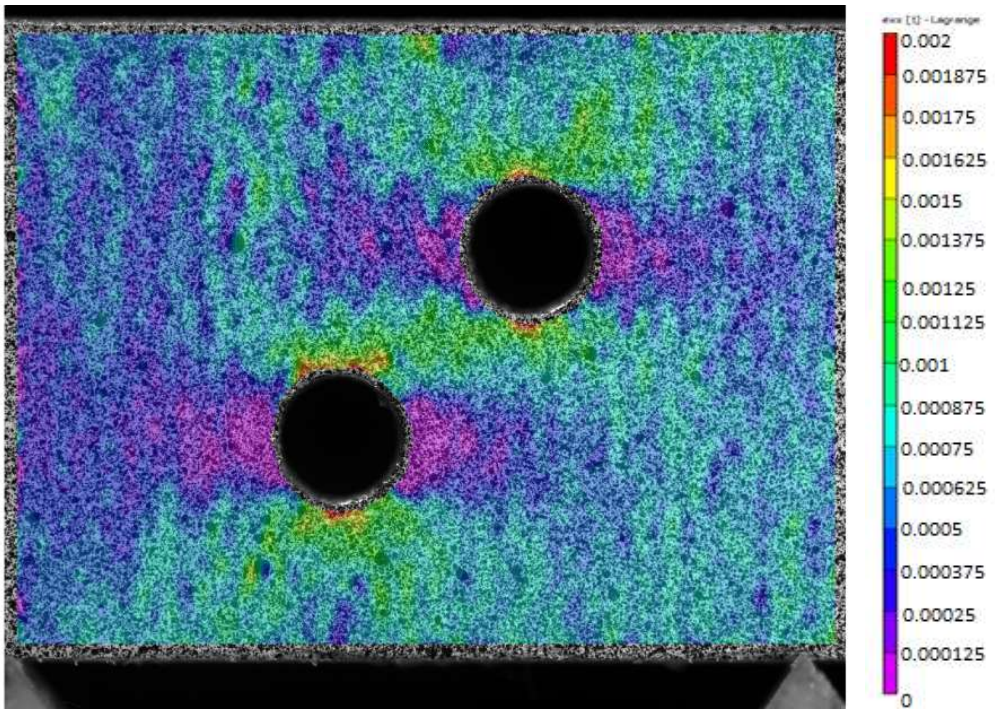

Figure 14 - S200H 23C FT DIC of axial surface strain at 100 MPa net-section stress

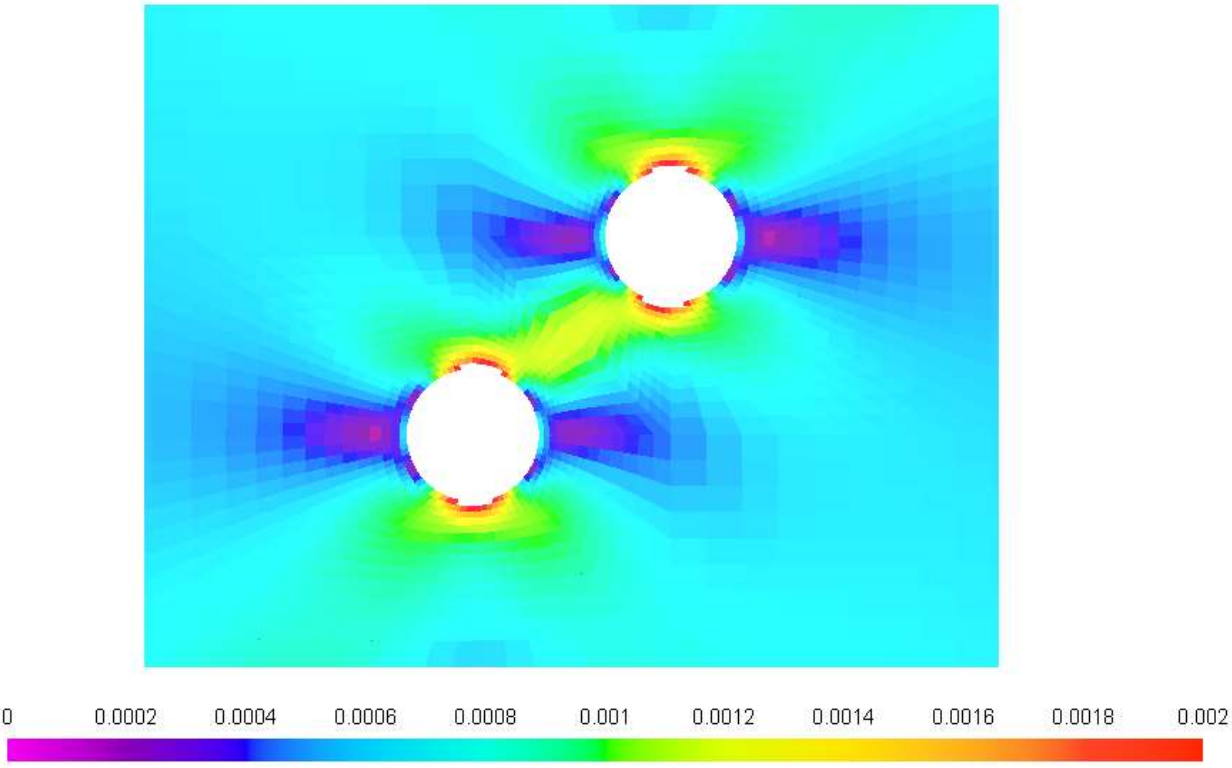

Figure 15 - S200H 23C FT simulation of axial surface strain at 100MPa net-section stress

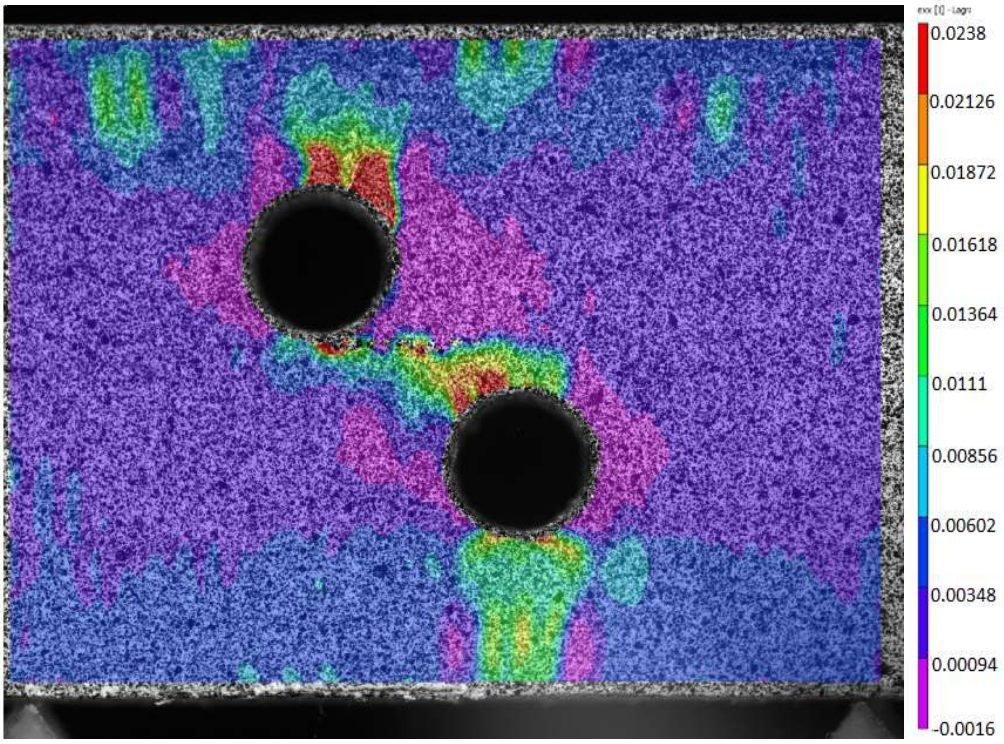

Figure 16 - S200H 23C FT DIC of axial surface strain just before failure

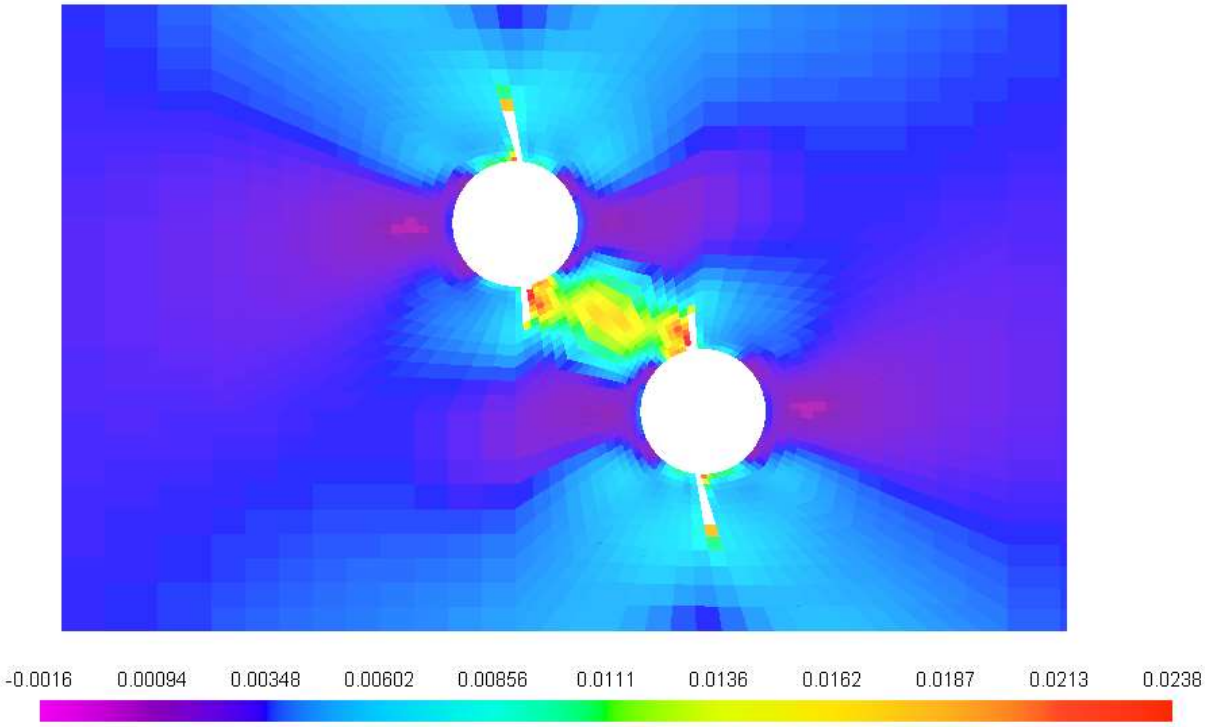

Figure 17 - S200H 23C FT simulation of axial surface strain just before failure

2.5.2. Short Duration Monotonic Tensile Tests for GEA SMI

Monotonic tensile experiments for the GEA SMI material system consist of UNT at 23°C and 1315°C with layups of $[0,90]_{2s}$, $[+45,-45]_{2s}$, and $[0,30,60,90]_s$. The $[0,90]_{2s}$ and $[0,30,60,90]_s$ experiments come from the 2020 EPPIC program, while the $[+45,-45]_{2s}$ experiments come from a prior testing program where the material system was an earlier generation of GEA SMI. The macroscopic finite element mesh for the UNT consists of a four layer 8-node hexahedron mesh that is constrained as in section 2.5.1 which can be seen in **Figure 18**. The $[0,30,60,90]_s$ layup is examined most closely through the initial quasi-static, creep, and fatigue analyses and the stress vs. strain curves for this unique layup can be seen in **Figure 19** and **Figure 20**.

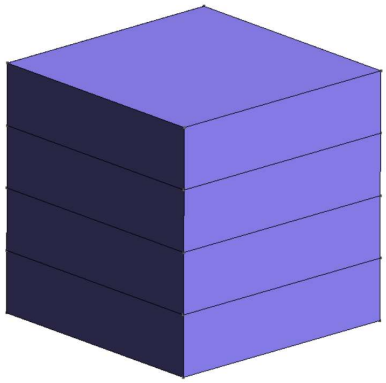

Figure 18 - GEA SMI macroscopic mesh

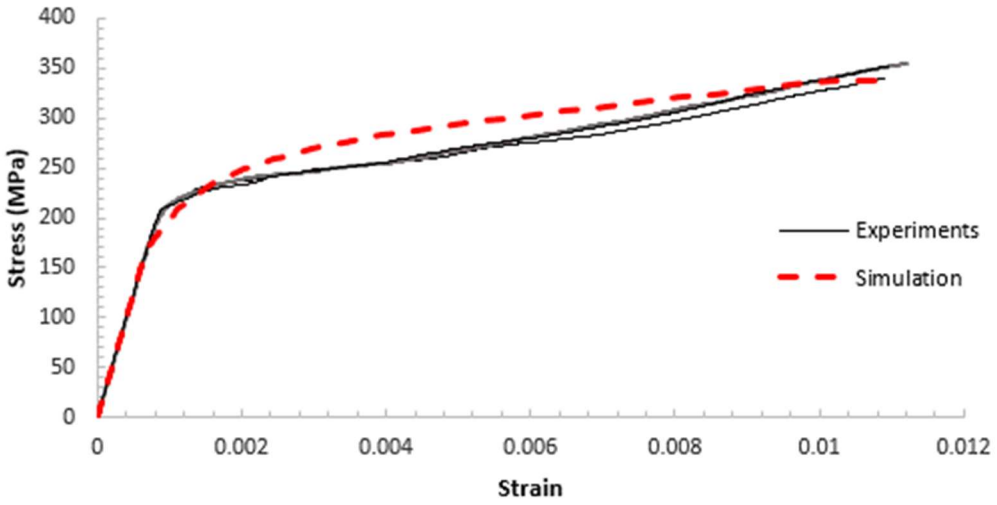

Figure 19 – GEA SMI 23C [0,30,60,90]s UNT experiment-simulation stress/strain

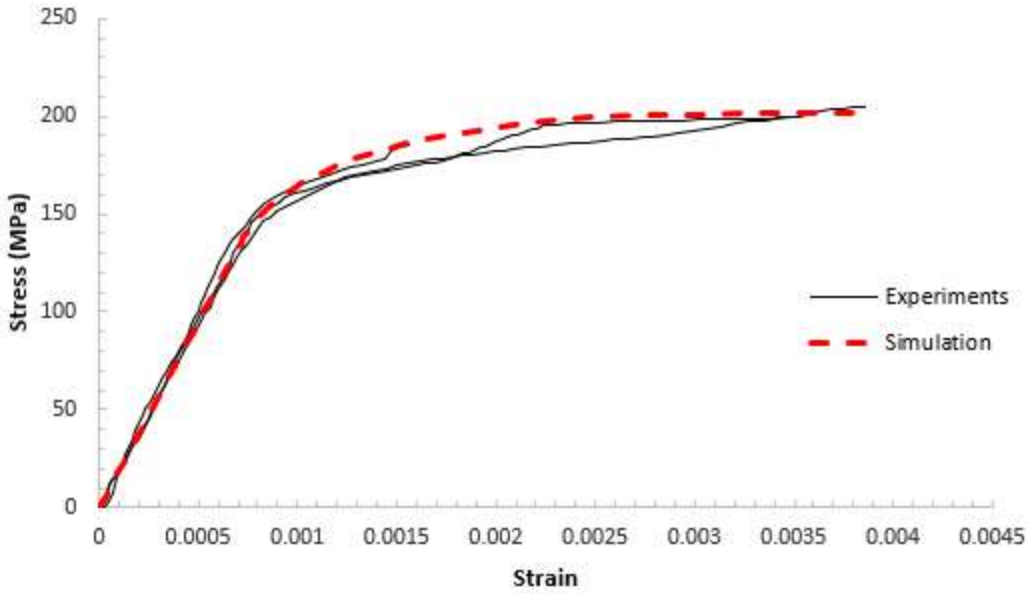

Figure 20 - GEA SMI 1315C [0,30,60,90]s UNT experiment-simulation stress/strain

The $[0,90]_{2s}$ UNT stress vs. strain curves can be seen in **Figure 21** - **Figure 22**.

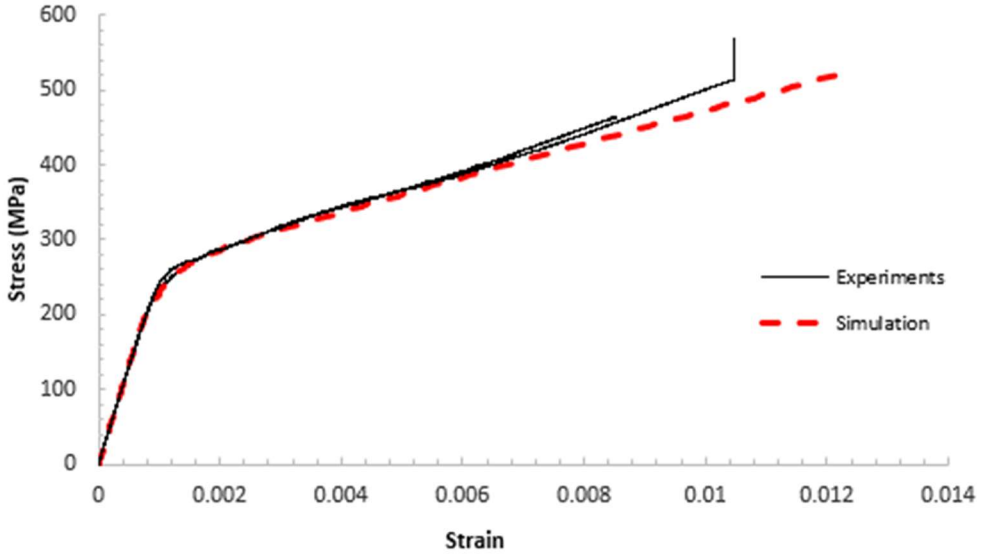

Figure 21 - GEA SMI 23C [0,90]2s UNT experiment-simulation stress/strain

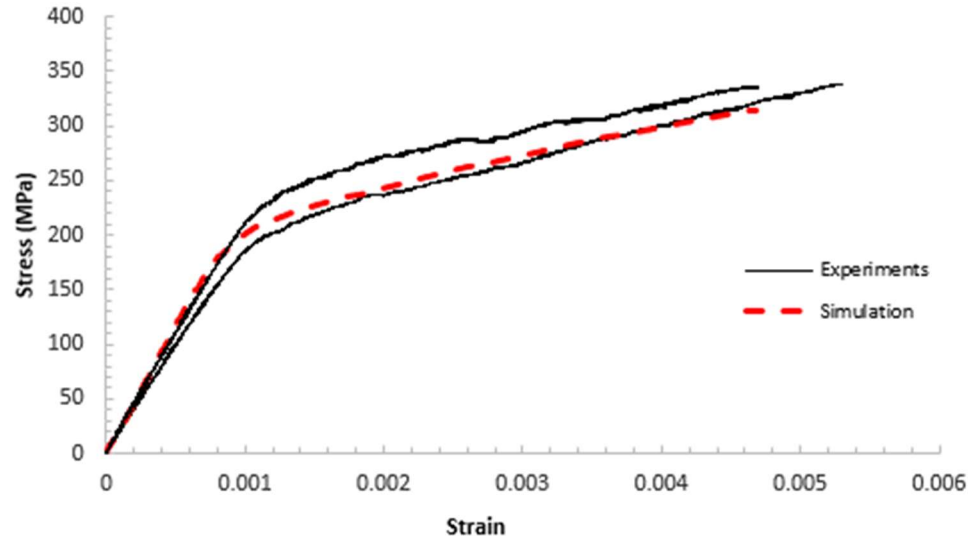

Figure 22 - GEA SMI 1315C [0,90]2s UNT experiment-simulation stress/strain

The $[+45,-45]_{2s}$ UNT stress vs. strain curves can be seen in **Figure 23** and **Figure 24**. The notable difference between simulation and test results can be attributed to the fact that the $[+45,-45]_{2s}$ experiments were conducted on the earlier generation of the material, which is consistent with the differences observed in the earlier generation material and the EPPIC program material.

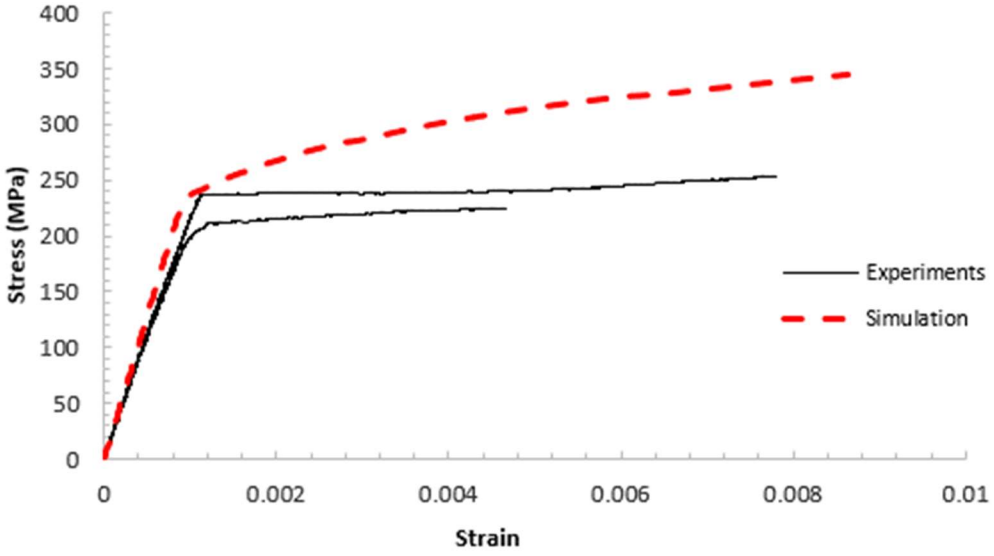

Figure 23 - GEA SMI 23C [+45,-45]2s UNT experiment-simulation stress/strain

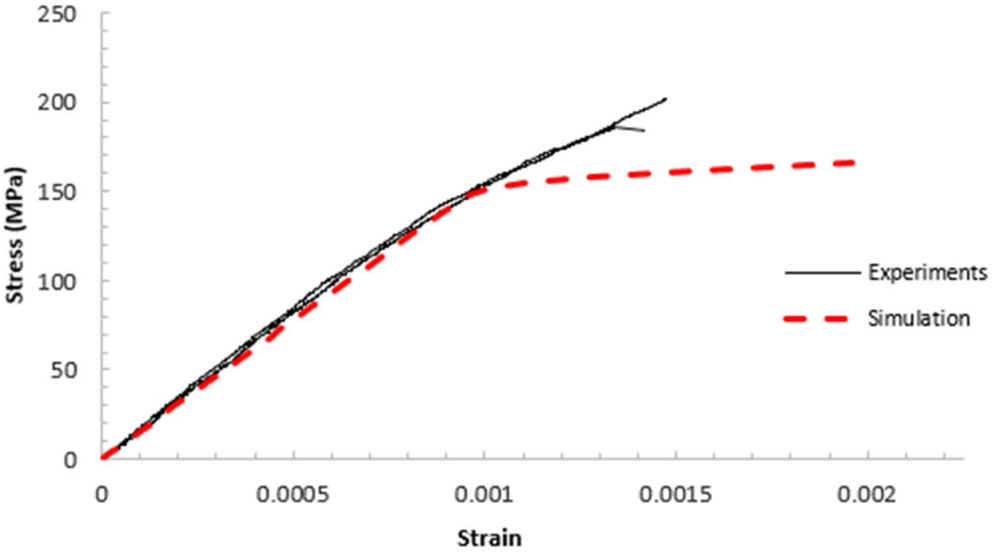

Figure 24 - GEA SMI 1315C [+45,-45]2s UNT experiment-simulation stress/strain

Chapter 3: Oxidation Assisted Damage Mode for Intermediate Temperatures

In this chapter we first describe a one-dimensional oxidation-assisted damage model of SiC fiber which assumes that the fiber is exposed to oxygen from the beginning due to as manufactured matrix pores and subsequent cracking. We then generalize the one-dimensional model to three-dimensions. In the three-dimensional model, the oxygen exposure of fibers will depend on the amount of matrix damage. We will assume the existence of a parameter χ_a based on the amount of damage in the matrix between the fibers and oxygenated environment that relates the degree of oxidation fiber strength degradation due to oxidation-assisted damage.

3.1. One-Dimensional Strength Degradation Model

The degradation of strength of CMC fibers under slow crack growth has been described in Iyengar and Curtin [44] as:

$$s(t) \equiv \left[s_0^{\beta-2} - \left(\frac{\beta}{2} - 1 \right) AY^2 \pi K_{Ic}^{\beta-2} \int_0^t \sigma_f^{\beta}(\tau) \mathrm{d}\tau \right]^{1/(\beta-2)} \tag{25}$$

where $s(t)$ is the strength of the fiber at time t; $\sigma_f(t)$ is the stress in the fiber direction at time t; s_0 is the initial mean strength of the fiber; β is the slow crack growth exponent; A is the coefficient defined as $A = A_0 \exp\{-E_a/RT\}$, A_0 is a material constant; T is the absolute temperature; E_a is the activation energy related to reaction at the crack tip; R is the universal gas constant; K_{Ic} is the mode I fracture toughness of the fiber; Y is the geometric parameter of crack shape. The geometric parameter for a penny shaped crack [44] is $Y = 2/\sqrt{\pi}$.

Equation (25), can be generalized to tows by approximating the stress in the fiber as

$$\sigma_f = \sigma_{tow}/v_f \tag{26}$$

where σ_{tow} is the stress in the axial tow direction and v_f is the volume fraction of fiber within the tow.

3.2. One-Dimensional Oxidation Induced Damage Model

The scalar damage state variable of the fiber ω_f is defined as the percentage of decrease of tensile strength

$$\omega_f \equiv 1 - s/s_0 \tag{27}$$

with the initial damage-free condition satisfying

$$\omega_f(0) = 1 - s(0)/s_0 = 0 \tag{28}$$

3.3. Integration of the One-Dimensional Oxidation Induced Damage Model

The time domain is decomposed into a series of sub-intervals. We label the start and end points for the current sub-interval as t_n and t_{n+1}, respectively. In addition, we assume all the information at t_n including ${}_n\omega_f$, ${}_n\sigma_f$, ${}_n\Sigma \equiv \int_0^{t_n} \sigma_f^\beta(\tau)\,\mathrm{d}\tau$ is converged and known.

The strength at the end of current increment is then given as

$${}_{n+1}s \equiv \left[s_0^{\beta-2} - c_1 \left({}_n\Sigma + \Delta\Sigma \right) \right]^{1/(\beta-2)} \tag{29}$$

where $c_1 \equiv 4(\beta/2-1) A K_{Ic}^{\beta-2}$ and $\Delta\Sigma \equiv \int_{t_n}^{t_{n+1}} \sigma_f^\beta(\tau)\,\mathrm{d}\tau$. Within the current increment, we assume the stress evolves linearly as

$$\sigma_f(t) = {}_n\sigma_f + \frac{t - t_n}{t_{n+1} - t_n} \left({}_{n+1}\sigma_f - {}_n\sigma_f \right), \quad t \in [t_n, t_{n+1}] \tag{30}$$

A trapezoidal integration method is used to evaluate $\Delta\Sigma$ that

$$\begin{aligned}\int_{t_n}^{t_{n+1}} \sigma_f^{\beta}(\tau)\,\mathrm{d}\tau &= (t_{n+1}-t_n)\int_0^1 \left[{}_n\sigma_f + \xi\left({}_{n+1}\sigma_f - {}_n\sigma_f \right)\right]^{\beta} \mathrm{d}\,\xi \\ &= \frac{t_{n+1}-t_n}{\beta+1}\frac{\left({}_{n+1}\sigma_f \right)^{\beta+1} - \left({}_n\sigma_f \right)^{\beta+1}}{{}_{n+1}\sigma_f - {}_n\sigma_f}\end{aligned} \tag{31}$$

If ${}_{n+1}\sigma_f = {}_n\sigma_f$, the integration in equation (31) reduces to

$$\int_{t_n}^{t_{n+1}} \sigma_f^{\beta}(\tau)\,\mathrm{d}\tau = (t_{n+1}-t_n)\left({}_n\sigma_f \right)^{\beta} \tag{32}$$

The nonlinear equation for ${}_{n+1}\sigma_f$ is given by

$$\begin{aligned}{}_{n+1}\sigma_f &= \left(1 - {}_{n+1}\omega_f\right) E_f\, {}_{n+1}\varepsilon_f = \frac{{}_{n+1}s}{s_{0,\delta c}} E_f\, {}_{n+1}\varepsilon_f \\ {}_{n+1}s &= \left[s_0^{\beta-2} - c_1\left({}_n\Sigma + \Delta\Sigma \right)\right]^{1/(\beta-2)}\end{aligned} \tag{33}$$

where E_f and ${}_{n+1}\varepsilon_f$ are the elastic modulus and a known strain at t_{n+1} in the fiber direction, respectively. Equation (33) can be rewritten as

$$h\left({}_{n+1}\sigma_f \right) = \left(\frac{{}_{n+1}\sigma_f}{E_f\, {}_{n+1}\varepsilon_f} \right)^{\beta-2} + c_1\left({}_n\Sigma + \Delta\Sigma \right) - 1 \tag{34}$$

where $\Delta\Sigma\left({}_{n+1}\sigma_f \right)$ is given in equation (31) or (32).

It is natural to satisfy the inequality that ${}_{n+1}\sigma_f < {}_{n+1}s$, i.e., the stress is less than the strength in the fiber direction. Accordingly, from equation (33), we have the constraint

$${}_{n+1}\varepsilon_f < s_0 / E_f \tag{35}$$

Alternatively, $\varepsilon_f \geq s_0 / E_f$ denotes fiber failure that implies

$${}_{n+1}\sigma_f = 0, \quad {}_{n+1}s = 0 \tag{36}$$

Otherwise, the axial stress ${}_{n+1}\sigma_f$ is solved by a local Newton iteration method of (34) and the damage parameter ${}_{n+1}\omega_f$.

3.4. Generalization of Oxidation Induced Damage Model to Multidimensions

It is assumed that the evolution of damage in the axial tow direction is governed by slow crack-growth model described in Sections 3.1-3.3 whereas the damage in the transverse direction of the tow as well in the matrix phase outside the tow is assumed to remain *time-independent* governed by the continuum damage mechanics model outlined in Chapter 2. The three-dimensional oxidation-assisted damage model of the tow in multidimensions is formulated based on equation (6) by advancing the evolution of the axial tow damage parameter with a damage parameter driven by the slow crack growth model.

A parameter χ_a is introduced which relates the degree of oxidation fiber strength degradation due to oxidation-assisted damage. This parameter will modify the oxidation-assisted damage variable ω_f by

$$\omega_1 = \chi_a \cdot \omega_f \tag{37}$$

The parameter χ_a is defined as

$${}_{n+1}\chi_a = \begin{cases} c_\chi + \dfrac{1-c_\chi}{\omega_\chi} \cdot {}_n\omega_p & c_\chi + \dfrac{1-c_\chi}{\omega_\chi} \cdot {}_n\omega_p < 1 \\ 1 & c_\chi + \dfrac{1-c_\chi}{\omega_\chi} \cdot {}_n\omega_p \geq 1 \end{cases} \tag{38}$$

where c_χ denotes volume fraction of initial matrix pores; ω_χ is the amount of matrix damage which will induce the full oxidation-assisted damage as developed in Sections 3.1-3.3 and ${}_n\omega_p$ is the amount of damage in the matrix representing cracks perpendicular to the fiber direction of

the tow being modified by χ_a from the previously converged increment. It is assumed that initial pores in the ceramic matrix will initiate a low level of oxidation induced damage [85], [86].Throughout the simulation, damage that accumulates in the matrix phase will increase the value of parameter χ_a, i.e. availability of oxygen to fibers due to matrix cracking.

3.5. Stress Update and Consistent Tangent Operator

Given phase strain ${}_{n+1}\varepsilon_{ij}$ and state variables ${}_{n}\kappa_I$, ${}_{n}\omega_f$, ${}_{n}\omega_p$, ${}_{n}\Sigma$

1. Compute equivalent strain:

$$\begin{aligned}\tilde{\varepsilon}_2 &= \frac{1}{2}\left({}_{n+1}\varepsilon_{22} + \sqrt{{}_{n+1}\varepsilon_{22}{}^2 + 4\left(c_{12}\,{}_{n+1}\varepsilon_{12}{}^2 + c_{23}\,{}_{n+1}\varepsilon_{23}{}^2\right)}\right)\\ \tilde{\varepsilon}_3 &= \frac{1}{2}\left({}_{n+1}\varepsilon_{33} + \sqrt{{}_{n+1}\varepsilon_{33}{}^2 + 4\left(c_{13}\,{}_{n+1}\varepsilon_{13}{}^2 + c_{23}\,{}_{n+1}\varepsilon_{23}{}^2\right)}\right)\end{aligned} \tag{39}$$

2. Update maximum equivalent strain:

$$\begin{aligned}{}_{n+1}\kappa_2 &= \max({}_{n}\kappa_2, \tilde{\varepsilon}_2)\\ {}_{n+1}\kappa_3 &= \max({}_{n}\kappa_3, \tilde{\varepsilon}_3)\end{aligned} \tag{40}$$

3. Using Newton method, solve for the oxidation-effected fiber stress and $\Delta\Sigma$ with an initial guess of ${}_{n+1}\sigma_f = \left(1 - {}_{n}\omega_f\right)E_f\,{}_{n+1}\varepsilon_f$:

$$\begin{aligned}h\left({}_{n+1}\sigma_f\right) &= \left(\frac{{}_{n+1}\sigma_f}{E_f\,{}_{n+1}\varepsilon_f}\right)^{\beta-2} + c_1\left({}_{n}\Sigma + \Delta\Sigma\right) - 1 = 0\\ \Delta\Sigma &= \frac{t_{n+1} - t_n}{\beta+1}\frac{\left({}_{n+1}\sigma_f\right)^{\beta+1} - \left({}_{n}\sigma_f\right)^{\beta+1}}{{}_{n+1}\sigma_f - {}_{n}\sigma_f}\end{aligned} \tag{41}$$

4. Compute axial fiber damage and update ${}_{n+1}\Sigma$:

$$\begin{aligned}{}_{n+1}\omega_f &= 1 - \frac{{}_{n+1}\sigma_f}{E_f\,{}_{n+1}\varepsilon_f}\\ {}_{n+1}\Sigma &= {}_{n}\Sigma + \Delta\Sigma\end{aligned} \tag{42}$$

5. Compute χ_a with the perpendicular damage state variable ${}_{n}\omega_p$ as per equation (38)

6. Compute damage variable:

$$\begin{aligned} {}_{n+1}\omega_1 &= \chi_a \cdot \omega_f \\ {}_{n+1}\omega_2 &= {}^{e}G_2\left({}_{n+1}\kappa_2\right) \\ {}_{n+1}\omega_3 &= {}^{e}G_3\left({}_{n+1}\kappa_3\right) \end{aligned} \tag{43}$$

7. Calculate damage-induced constitutive matrix L^{in}_{ijkl} per equation **(6)**. L^{in}_{ijkl} is also used as the consistent tangent.

8. Update stress:

$${}_{n+1}\sigma_{ij} = {}_{n+1}\, L^{in}_{klmn}\, {}_{n+1}\varepsilon_{ij} \tag{44}$$

3.6. Numerical Examples

3.6.1. Uniaxial Tension Single Element Ultimate Time Comparison

To verify that the stress update procedure correctly simulates the strength degradation equation (25), simulation results are compared with a theoretical strength degradation curve. When the load is constant, equation (25) can be simplified as

$$s(t) \equiv \left[s_0^{\beta-2} - 2(\beta-2) A K_{Ic}^{\beta-2} \sigma_0^{\beta} t \right]^{1/(\beta-2)} \tag{45}$$

where the relations $Y = 2/\sqrt{\pi}$ and $A = A_0 e^{\frac{E_a}{RT}}$ are utilized. Accordingly, the ultimate allowable time t_u is evaluated at $s(t_u) = 0$, i.e.

$$t_u = s_0^{\beta-2} \Big/ \left[2(\beta-2) A K_{Ic}^{\beta-2} \sigma_0^{\beta} \right] \tag{46}$$

Equation (46) can be used to define theoretical values for t_u under different conditions. Two sets of example problems are tested in order to verify the ultimate allowable time t_u. Two reference

temperatures are selected, $T = 1111K°$ and $T = 1389\,K°$. At each temperature level, four different levels of constant load are tested.

The elastic and inelastic material properties of the fiber model being compared are the same as those used to model the tows of the weave employed in the other numerical examples. In addition to the previously defined properties, the oxidation driven damage parameters for this material can be found in Appendix B. The constants for the oxidation model, as listed in Appendix B are for Hi-Nicalon^{TM} fiber identified by fitting fiber and tow oxidation lifetime data of Gauthier and Lamon [87] to the slow crack growth model of Iyengar and Curtin [44] and Gauthier and Lamon [87].

These material properties are applied to the fiber material model with a χ_a set to 1.0 to immediately initiate full degradation and a single element was loaded to match the theoretical calculation. **Figure 25** depicts the comparison of theoretical and simulation results of failure time t_u, which are in agreement:

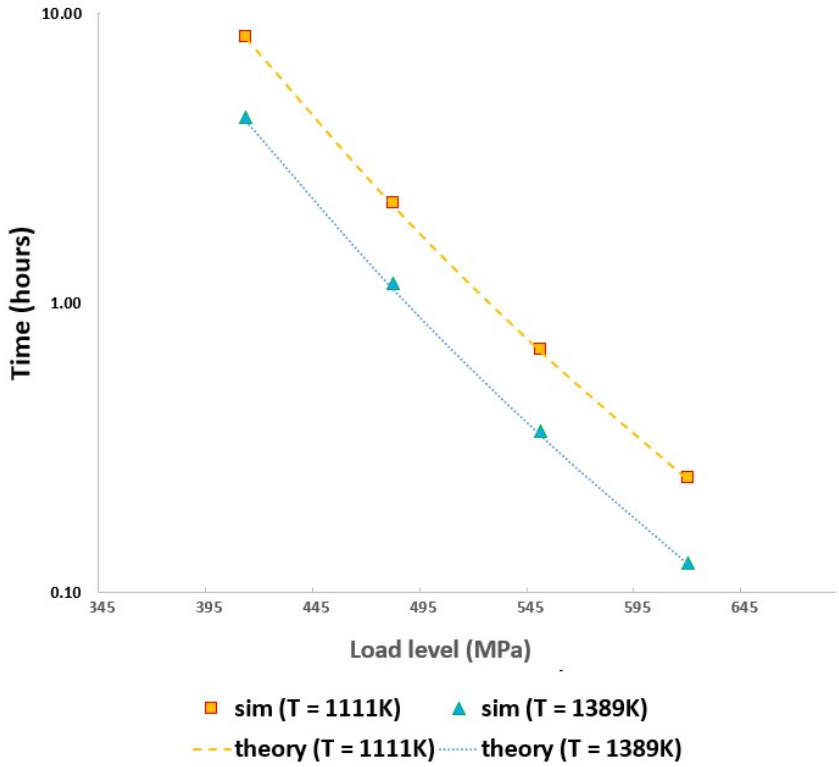

Figure 25 S200H ultimate allowable working time between theoretical and simulated results

3.6.2. Stress Rupture Test on a Plate-With-Hole with Varying χ_a Curves

With the material model calibrated for quasi-static tests and the oxidation assisted damage model matching the theoretical response, a stress rupture test is considered where the macro model is subject to a constant load. From a computational point of view, simulation of a stress rupture test is more challenging than a relaxation test because immediately following failure there is no numerical solution, which causes difficulty in achieving convergence. Therefore, a restart functionality is utilized in the simulation. The loading increment is restarted with a reduced increment size when divergence is detected.

The simulation environment is set to $\sigma_0 = 74.5$ [MPa] and $T = 1088K°$ with the same material properties as the other tests. This matches the physical testing condition of the three stress rupture tests considered.

The specimen being simulated is a plate-with-hole structure with a thickness 2.682 mm, a width of 22.86 mm, and features a hole in the center with a radius of 2.286 mm. Using symmetry, only a quarter of the specimen is meshed and modeled. The mesh for this model can be seen in **Figure 26**:

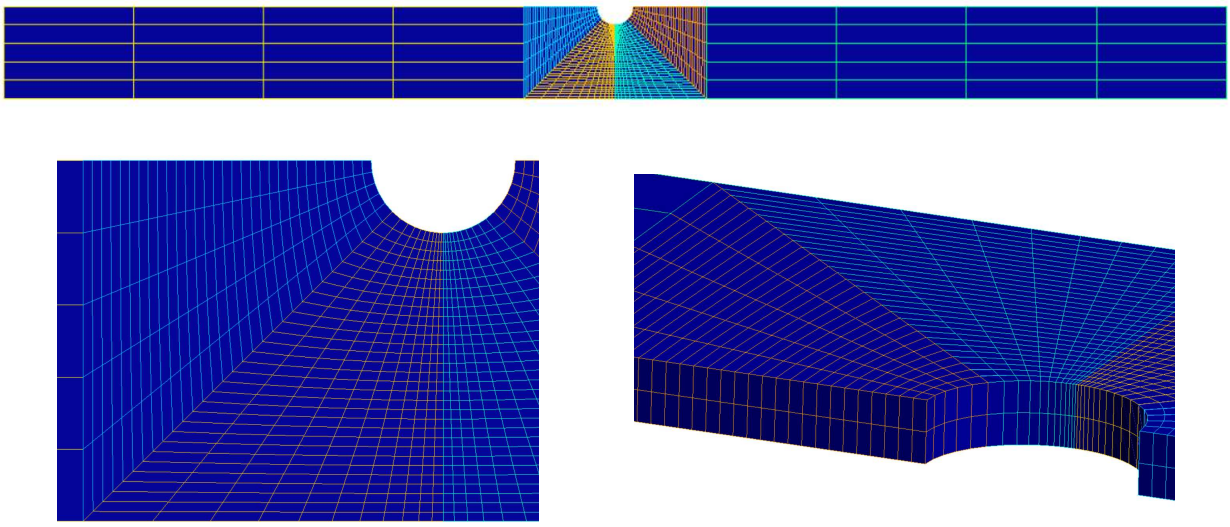

Figure 26 – S200H plate with hole macroscopic mesh for stress rupture test

One of the difficulties in verifying oxidation-assisted damage models for CMCs is the relatively small set of experimental results available given the high cost of manufacturing the materials as well as the sensitivity with which the results are often treated due to confidentiality. In addition to the small set of experimental results, there is also often a large variance in the results due to the nature of stress rupture tests.

Despite these challenges, the effectiveness of the χ_a parameter in bringing the simulation more in line with physical experiments is expected given the increased physicality it brings to the

model. More test data and with it χ_a curve refinement could further increase the accuracy of the model.

Figure 27 shows three experimental results, with stress rupture at 60 hours, 102 hours, and 200 hours. It also shows the displacement at the end of the simulated test coupon versus time for two numerical simulations. The sharp increase of displacement at the end of each simulation represents the failure of the specimen.

The first simulation uses a c_χ of 0.1 and a ω_χ of 0.77. Developing χ_a with these values gives a simulated specimen lifetime of 102 hours which is well within the range of experimental values. Increasing c_χ and ω_χ to 1.0 so that oxidation induced damage begins in all fibers immediately upon the simulation starting results in a lifetime of 53 hours. This lifetime lies slightly outside of the range of experimental values and shows the utility of the χ_a parameter.

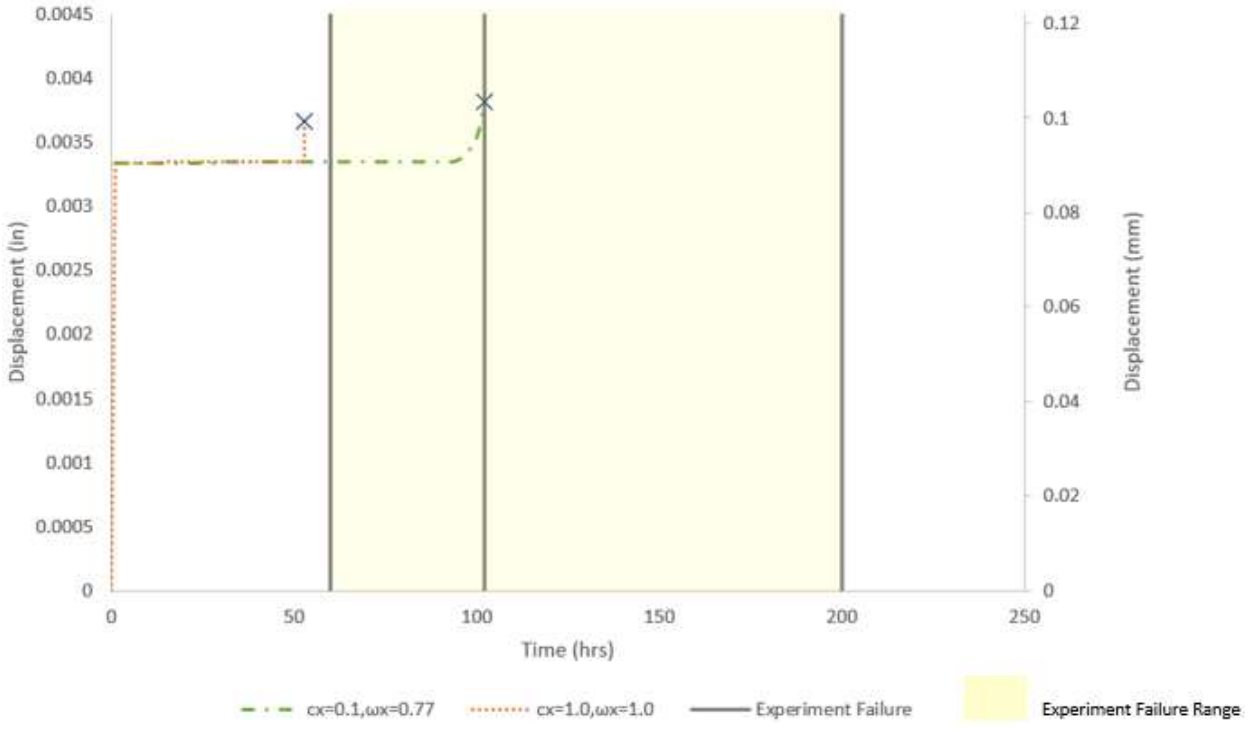

Figure 27 – S200H 1088K $[0,90]_{2s}$ plate with hole experiment-simulation displacement vs time with varying χ_a

Closer examination of the results from the simulation where ω_χ was 0.77 and c_χ was 0.1 shows the development of damage due to oxidation. In the tows, this damage develops slowly at first in the area around the hole where the stress is highest. Over time, as the damage spreads, a crack forms and the tows rapidly fail. This damage development is shown in **Figure 28**. The damage shown represents the damage variable ω_1 of the tows oriented in the direction of the applied tensile force, denoted ω_1^t.

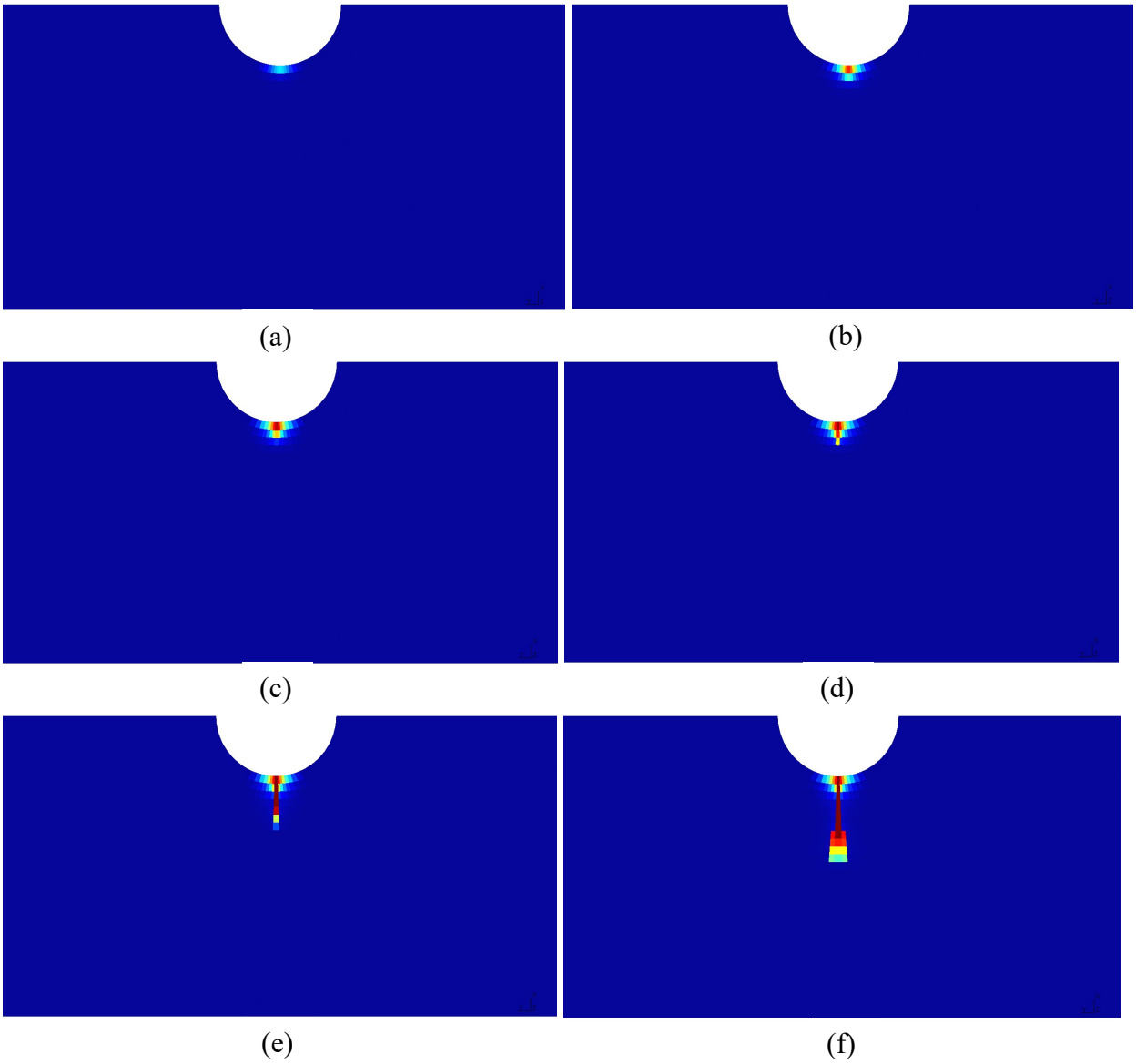

(a) (b) (c) (d) (e) (f)

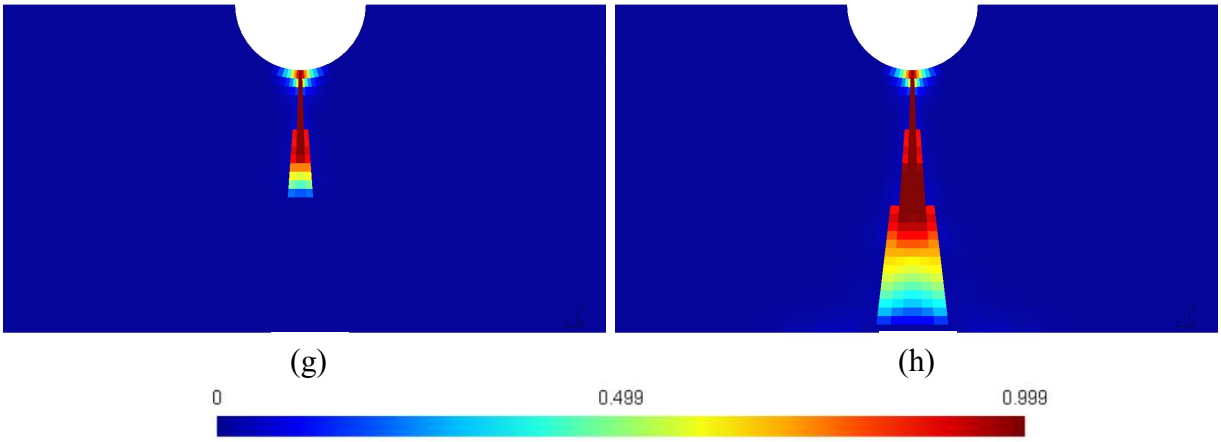

Figure 28 - S200H 1088K $[0,90]_{2s}$ tow damage variable ω_1^1 due to oxidation in open hole tension test at (a) 12 hours (b) 48 hours (c) 84 hours (d) 95 hours (e) 97 hours (f) 99 hours (g) 100 hours (h) 102 hours

The damage in the matrix perpendicular to the tows develops with the tow damage. The matrix damage allows oxygen to access the tows so that oxidation can occur. At the same time, the failure of the tows increases the damage in the matrix. The development of the matrix damage variable denoted ω_2^m for the same simulation at the same time interval as in **Figure 28** can be seen in **Figure 29**.

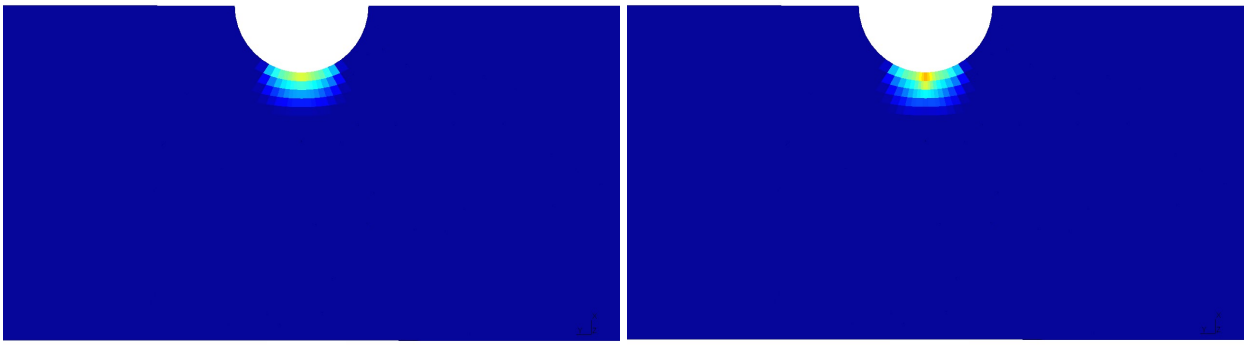

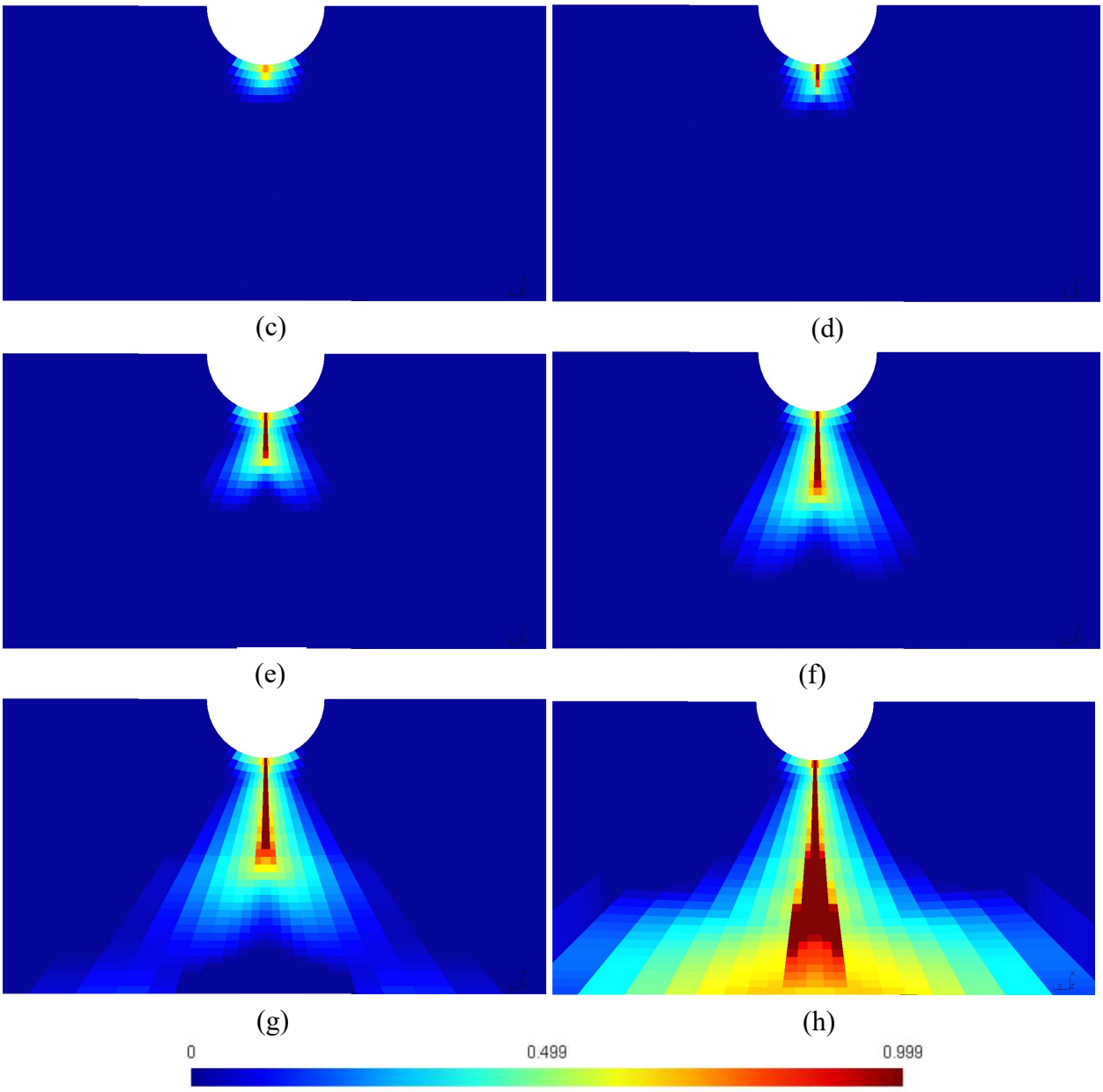

Figure 29 - S200H 1088K $[0,90]_{2s}$ matrix damage variable ω_2^m due to oxidation in open hole tension test at (a) 12 hours (b) 48 hours (c) 84 hours (d) 95 hours (e) 97 hours (f) 99 hours (g) 100 hours (h) 102 hours

Chapter 4: Creep Model for High Temperatures

The creep model for high temperatures is a phase material model which combines the orthotropic continuum damage model outlined in Chapter 2 with an implicit version of the Perzyna, Perić [88], [89] viscoplasticity model for both initial quasi-static and creep analyses.

4.1. Hybrid Damage-Viscoplasticity Constitutive Model

Consider the following:

$$\begin{aligned} \sigma_{ij} &= L^{in}_{ijmn}\varepsilon^{e}_{mn} \\ \varepsilon^{e}_{mn} &= \varepsilon_{mn} - \varepsilon^{p}_{mn} \end{aligned} \tag{47}$$

where the total strain is decomposed into the recoverable elastic ε^{e}_{mn} and non-recoverable viscoplastic strain components ε^{p}_{mn}.

For model reduction (see Appendix A) equation (47) can be recast as follows

$$\sigma_{ij} = L_{ijkl}\left(\varepsilon_{kl} - \mu_{kl}\right) \tag{48}$$

where damage and viscoplasticity induced eigenstrain components μ_{kl} are given by

$$\begin{aligned} \mu_{ij} &= \left(I_{ijkl} - \omega_{ijkl}\right)\varepsilon_{kl} + \omega_{ijkl}\varepsilon^{p}_{kl} \\ \omega_{ijkl} &= \left(L_{ijmn}\right)^{-1} L^{in}_{mnkl} = \left(W_{ijkl}\right)^{2} \end{aligned} \tag{49}$$

where I_{ijkl} is the fourth order identity tensor and W_{ijkl} is the fourth order damage tensor, defined in Voigt notation in (2). Equation (49)b follows from the diagonality of W_{ijkl} and (4)b.

This hybrid material model operates in two regimes, initial quasi-static and creep. The initial quasi-static regime is used for initial monotonic or cyclic loading. The creep regime contains the primary, secondary, as well as failure creep regions utilizing the hybrid damage-viscoplasticity formulation. The transition between initial quasi-static and creep regimes is user-

defined. In the computational implementation herein, the initial quasi-static regime is defined by bounds on the simulation time.

4.2. Damage Evolution

The brittle damage evolution function $G_I(\kappa_I, \alpha)$ is comprised of the piecewise linear function ${}^{e}G_I(\kappa_I)$ as defined in section 2.3 and a ductile failure function ${}^{vp}H(\alpha)$ described in section 4.4 and is defined:

$$G_I(\kappa_I, \alpha) = \max\left({}^{e}G_I(\kappa_I), {}^{vp}H(\alpha)\right) \tag{50}$$

Generalizing the damage function (14) from section 2.3 yields:

$$\omega_I = G_I(\kappa_I, \alpha) \tag{51}$$

where α is the equivalent viscoplastic strain as described in section 4.3. Both the loading history variable κ_I and the equivalent viscoplastic strain α do not decrease and $G_I(\kappa_I, \alpha)$ is monotonically increasing so $\dot{G}_I$ is strictly non-negative.

For brittle damage evolution in creep regime the equivalent strain is defined as

$$\begin{aligned}
\tilde{\varepsilon}_1 &= \frac{1}{2}\left(\varepsilon_{11}^e + \sqrt{\varepsilon_{11}^{e\,2} + 4\left(c_{12}\varepsilon_{12}^{e\,2} + c_{13}\varepsilon_{13}^{e\,2}\right)}\right) \\
\tilde{\varepsilon}_2 &= \frac{1}{2}\left(\varepsilon_{22}^e + \sqrt{\varepsilon_{22}^{e\,2} + 4\left(c_{12}\varepsilon_{12}^{e\,2} + c_{23}\varepsilon_{23}^{e\,2}\right)}\right) \\
\tilde{\varepsilon}_3 &= \frac{1}{2}\left(\varepsilon_{33}^e + \sqrt{\varepsilon_{33}^{e\,2} + 4\left(c_{13}\varepsilon_{13}^{e\,2} + c_{23}\varepsilon_{23}^{e\,2}\right)}\right)
\end{aligned} \tag{52}$$

with shear correction factors reduced to 1, i.e., $c_{ij} = 1$, to permit ductile deformation based on the viscoplasticity model described in the next section. It is instructive to point out that reducing the values of equivalent strains does not change the effective properties L_{ijmn}^{in} in transition from an initial quasi-static to creep regime, and yet further accumulation of brittle damage is still possible with an increase of elastic deformation in the creep regime.

4.3. Viscoplasticity Model

A viscoplasticity model developed from a standard plasticity return mapping [90], [91] is adopted herein. The yield surface and isotropic hardening are defined as:

$$K(\alpha) = K_0 + (K_1 - K_0)\left[1 - e^{-\delta\alpha}\right] + H_0\alpha \tag{53}$$

where K_0 is the yield strength, K_1 is the ultimate strength, δ is an exponent parameter, H_0 is a linear hardening term, and α is the equivalent viscoplastic strain. The viscoplastic flow rule is defined as:

$$\begin{aligned} s_{ij} &= P^{y}_{ijkl}\sigma_{kl} \\ \dot{\varepsilon}_{ij}{}^{p} &= \dot{\gamma} s_{ij} \\ \left\| s_{ij} \right\| &= \sqrt{s_{ij}s_{ij}} \\ \dot{\gamma} &= a\left[\frac{\left\| s_{ij} \right\|}{\sqrt{\frac{2}{3}}K(\alpha)}\right]^{\frac{1}{m}} \end{aligned} \tag{54}$$

where *a* and *m* are material parameters, P^{y}_{ijkl} is the deviatoric projector, and s_{ij} is the deviatoric stress.

4.4. Ductile Failure

Ductile failure is assumed to take place when the viscoplastic strain limit is reached. This type of failure is modeled using the following smoothed Heaviside step function:

$${}^{vp}H(\alpha) = \frac{\tanh\left(\beta\eta\right) + \tanh\left(\beta\left(\alpha - \eta\right)\right)}{\tanh\left(\beta\eta\right) + \tanh\left(\beta\left(\omega_{\max} - \eta\right)\right)} \tag{55}$$

where β defines the strength of the smoothing function and η is the viscoplastic strain limit.

4.5. Semi-Implicit Stress Update Procedure and Consistent Tangent Operator

Given the phase strain ${}_{n+1}\varepsilon_{ij}$ and state variables from the previous step ${}_{n}\kappa_I$, ${}_{n}\varepsilon_{ij}^{p}$, ${}_{n}\alpha$

1. Compute elastic strain

$$ {}_{n+1}\varepsilon_{ij}^{e} = {}_{n+1}\varepsilon_{ij} - {}_{n}\varepsilon_{ij}^{p} \tag{56} $$

2. Determine if analysis is in initial quasi-static or creep regime by checking the simulation time *t* and comparing it to simulation parameters defining loading conditions

3A. If analysis is in initial quasi-static regime:

I. Compute equivalent strain:

$$ \begin{aligned} {}_{n+1}\tilde{\varepsilon}_1 &= \frac{1}{2}\left({}_{n+1}\varepsilon_{11}^{e} + \sqrt{ {}_{n+1}\varepsilon_{11}^{e\,2} + 4\left(c_{12}\,{}_{n+1}\varepsilon_{12}^{e\,2} + c_{13}\,{}_{n+1}\varepsilon_{13}^{e\,2} \right) } \right) \\ {}_{n+1}\tilde{\varepsilon}_2 &= \frac{1}{2}\left({}_{n+1}\varepsilon_{22}^{e} + \sqrt{ {}_{n+1}\varepsilon_{22}^{e\,2} + 4\left(c_{12}\,{}_{n+1}\varepsilon_{12}^{e\,2} + c_{23}\,{}_{n+1}\varepsilon_{23}^{e\,2} \right) } \right) \\ {}_{n+1}\tilde{\varepsilon}_3 &= \frac{1}{2}\left({}_{n+1}\varepsilon_{33}^{e} + \sqrt{ {}_{n+1}\varepsilon_{33}^{e\,2} + 4\left(c_{13}\,{}_{n+1}\varepsilon_{13}^{e\,2} + c_{23}\,{}_{n+1}\varepsilon_{23}^{e\,2} \right) } \right) \end{aligned} \tag{57} $$

II. Update the maximum equivalent strain as in equation (22)

III. Compute the damage variable as in equation (23)

3B. If analysis is in creep regime:

I. Compute the equivalent strain using (57) with shear correction factors given by

$$ c_{ij} = 1 \tag{58} $$

II. Update the maximum equivalent strain as in equation (22)

III. Compute the damage variable:

$$ {}_{n+1}\omega_I = \beta\,{}_{n+1}\max\left({}^{e}G_I\left({}_{n+1}\kappa_I \right), {}^{vp}H_I\left({}_{n}\alpha \right) \right) + \left(1-\beta \right){}_{n}\omega_I \tag{59} $$

4. Calculate the damage-induced constitutive matrix L_{ijkl}^{in} per equation (6)

5. Compute the viscoplastic trial state:

$$
\begin{aligned}
&{}_{n+1}\sigma_{ij}^{trial} = {}_{n+1}L_{ijkl}^{in}\,{}_{n+1}\varepsilon_{ij}^{e} \\
&{}_{n+1}s_{ij}^{trial} = P_{ijkl}\,{}_{n+1}\sigma_{kl}^{trial} \\
&\left\| {}_{n+1}s_{ij}^{trial} \right\| = \sqrt{{}_{n+1}s_{ij}^{trial}\,{}_{n+1}s_{ij}^{trial}} \\
&{}_{n+1}n_{ij} = \frac{{}_{n+1}s_{ij}^{trial}}{\left\| {}_{n+1}s_{kl}^{trial} \right\|}
\end{aligned}
\tag{60}
$$

6. Solve consistency equation using the Newton method for consistency parameter $\Delta\gamma$:

$$
g(\Delta\gamma) = \left\| {}_{n+1}s_{ij}^{trial} \right\| - \left(\frac{\Delta\gamma}{a\Delta t} \right)^{m} \sqrt{\frac{2}{3}} K({}_{n+1}\alpha) - \Delta\gamma P_{ijkl}\,{}_{n+1}L_{klmn}^{in}\,{}_{n+1}n_{mn}\,{}_{n+1}n_{ij} = 0 \tag{61}
$$

For the initial value of $\Delta\gamma$ an forward Euler integration of (54) is employed

$$
\Delta\gamma = a\Delta t \left[\frac{\left\| {}_{n+1}s_{ij}^{trial} \right\|}{\sqrt{\frac{2}{3}} K({}_{n}\alpha)} \right]^{\frac{1}{m}} \tag{62}
$$

7. Update the stress and viscoplastic state variables:

$$
{}_{n+1}\sigma_{ij} = {}_{n+1}\sigma_{ij}^{trial} - \Delta\gamma P_{ijkl}\,{}_{n+1}L_{klmn}^{in}\,{}_{n+1}n_{mn} \tag{63}
$$

$$
{}_{n+1}\varepsilon_{ij}^{p} = {}_{n}\varepsilon_{ij}^{p} + \Delta\gamma\,{}_{n+1}n_{ij} \tag{64}
$$

$$
{}_{n+1}\alpha = {}_{n}\alpha + \sqrt{\frac{2}{3}}\Delta\gamma \tag{65}
$$

Note that once ${}_{n+1}\varepsilon_{ij}^{p}$ is computed, one can go back to step 1 and recompute elastic strains and proceed to step 7 and so forth until convergence is reached. Herein, we pursue a semi-explicit algorithm which is implicit in viscoplasticity but explicit in damage since damage variables mostly remain constant during creep.

8. Compute the consistent constitutive tangent tensor:

$$ {}_{n+1}C_{ijkl} = L_{ijkl} - P_{ijop\ n+1}L^{in}_{opmn\ n+1}n_{mn}\frac{\partial \Delta\gamma}{\partial_{n+1}\varepsilon_{kl}} - \Delta\gamma P_{ijop\ n+1}L^{in}_{opmn}\frac{\partial_{n+1}n_{mn}}{\partial_{n+1}\varepsilon_{kl}} \tag{66} $$

where:

$$ \frac{\partial \Delta\gamma}{\partial_{n+1}\varepsilon_{kl}} = \frac{P_{klmn\ n+1}L_{mnop\ n+1}n_{op} - \frac{2\Delta\gamma P_{ijts\ n+1}L^{in}_{tsqr\ n+1}L^{in}_{qrmn\ n+1}n_{mn}}{\left\|{}_{n+1}s^{trial}_{op}\right\|}\left[\mathbb{I}_{ijkl} - {}_{n+1}n_{ij\ n+1}n_{kl}\right]}{\left(\frac{\Delta\gamma}{a\Delta t}\right)^{m}\sqrt{\frac{2}{3}}K'({}_{n+1}\alpha) + \frac{m}{\Delta\gamma}\left(\frac{\Delta\gamma}{a\Delta t}\right)^{m}\sqrt{\frac{2}{3}}K({}_{n+1}\alpha) + P_{ijkl\ n+1}L^{in}_{klmn\ n+1}n_{mn\ n+1}n_{ij}} \tag{67} $$

$$ \frac{\partial_{n+1}n_{mn}}{\partial_{n+1}\varepsilon_{kl}} = \frac{P_{mnrs\ n+1}L^{in}_{rsij}}{\left\|{}_{n+1}s^{trial}_{op}\right\|}\left[\mathbb{I}_{ijkl} - {}_{n+1}n_{ij\ n+1}n_{kl}\right] \tag{68} $$

4.6. High Temperature Crack Sealing and Strength Reduction

It has been demonstrated in SiC/SiC CMCs that under long term loading at high temperatures, modulus degradation is greater in an inert rather than oxidative environment [31] indicating an oxidation induced crack-sealing mechanism. Additionally, there is a degree of ultimate strength reduction that occurs in SiC/SiC CMCs in these loading scenarios. To reflect these conditions, a special case has been included in the model wherein during a post-creep or -fatigue loading scenario, accumulated damage is reduced to zero and a strength reduction is applied to the pertinent peak strength damage model parameter.

Numerical results where this scheme is utilized are compared to the simulation results without the sealing and strength reduction.

4.7. Numerical Examples

4.7.1. Creep of S200H

The S200H material model used in Section 2.5.1 is used to model the behavior of S200H under high temperature creep. Creep experiments available for the S200H material system

include UNT and open hole tension tests (OHT). The dimensions of the OHT test specimen as shown in **Figure 30** are found in **Table 2**.

Table 2 – OHT Dimensions

	mm
Length	150
Width	24
Radius	4
Thickness	2.3

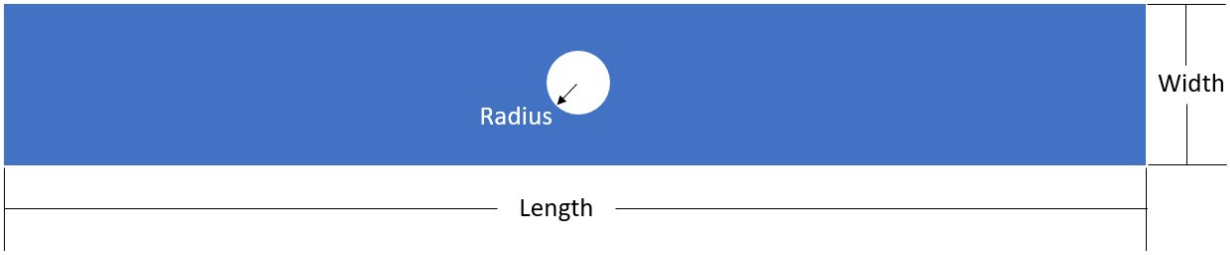

Figure 30 - S200H 1200C plate with hole specimen

Creep tests on UNT and OHT specimens are conducted on $[0,90]_{2s}$ layup at 1200°C. The UNT test comes from the same 2018 experiments as in Section 2.5.1, just as the OHT tests come from the same 2020 EPPIC program experiments. The macroscopic finite element mesh for the UNT consists of a single 8-node hexahedron mesh that is symmetrically constrained as in Section 2.5.1. The macroscopic finite element mesh for the OHT also utilizes symmetry where x,y, and z faces are constrained in such a way that only $1/8^{th}$ of the specimen need be modeled. The model is meshed with 8-node hexahedrons and is shown in **Figure 31**.

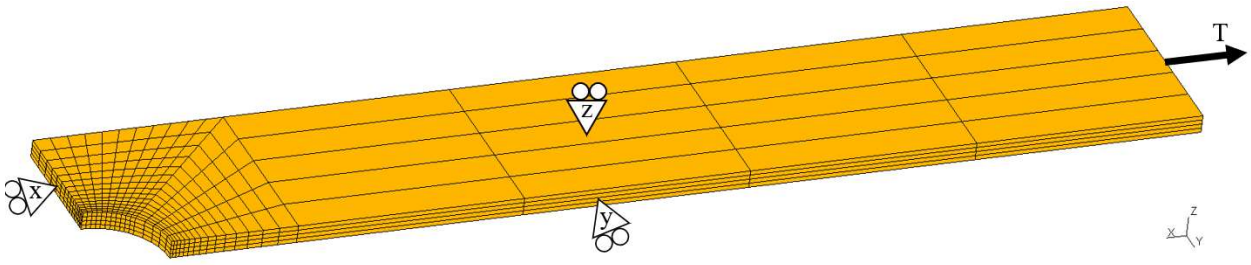

Figure 31 - S200H 1200C OHT macroscopic mesh

In the creep rupture tests, the specimen is loaded quasi-statically to the prescribed creep load and this load is maintained until failure. The OHT experiments also include an interrupted test where the creep test is unloaded before failure and then reloaded at room temperature to determine post-creep retained strength.

The UNT creep rupture test has an applied stress of 150 MPa and a strain vs. time curve for both the experiment and simulation is shown in **Figure 32**.

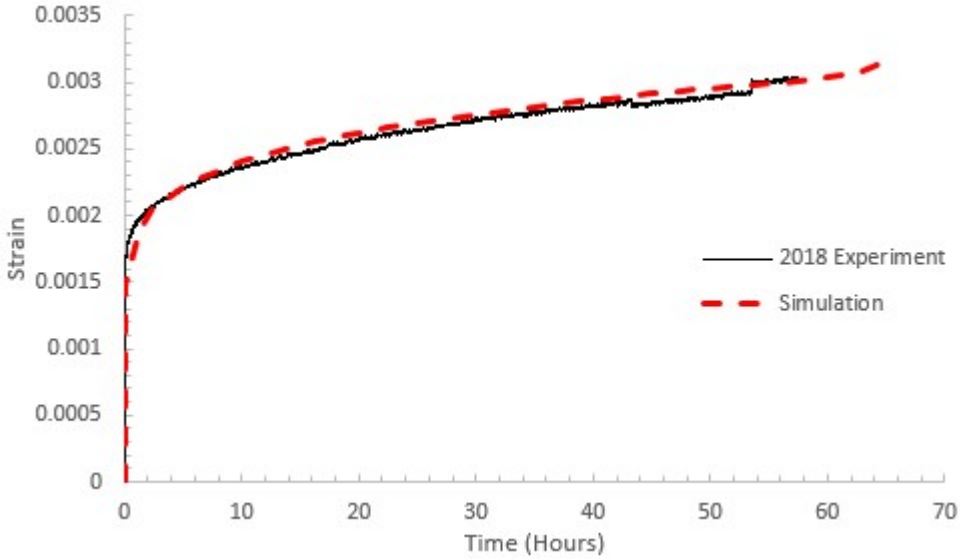

Figure 32 - S200H 1200C $[0,90]_{2s}$ 150MPa creep UNT experiment-simulation strain/time

The OHT creep rupture test has an applied net-section stress of 145 MPa and an extensometer displacement vs. time curve for both the experiment and simulation is shown in **Figure 33**.

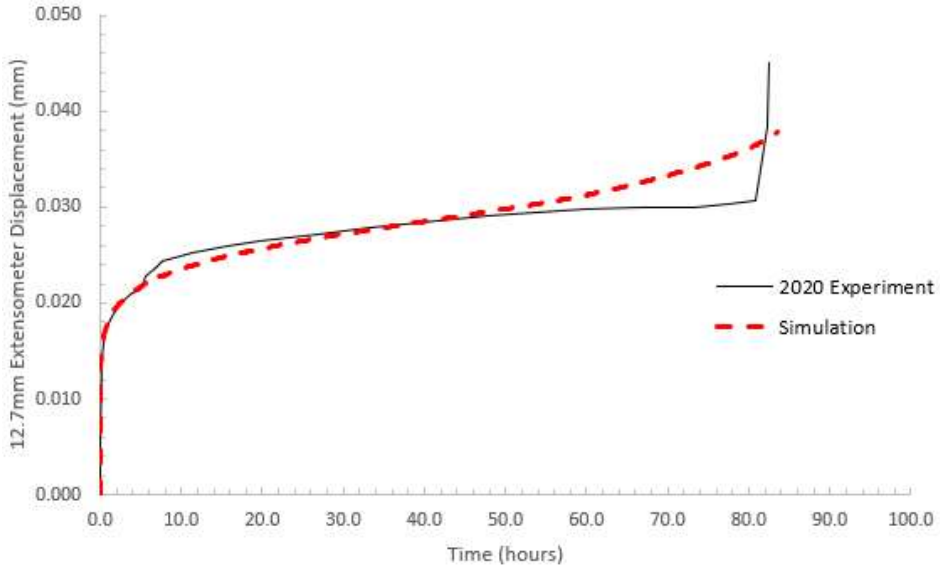

Figure 33 - S200H 1200C $[0,90]_{2s}$ 145MPa creep OHT experiment-simulation strain/time

The OHT interrupted creep test also has an applied net-section stress of 145 MPa. After the experiment was interrupted at 50 hours, the specimen maintained a permanent displacement of 0.0149 mm. The simulation predicts a permanent displacement of 0.0156 which is 4.7% greater than the experiment. The reloaded retained strength test can be found in **Figure 34**. Without any crack sealing or strength reduction, the proposed model overpredicts brittle damage evidenced by softer initial slope as well as the yield stress evidenced by higher stress. By adding crack sealing and strength reduction, the model captures the reloading behavior of the experiment.

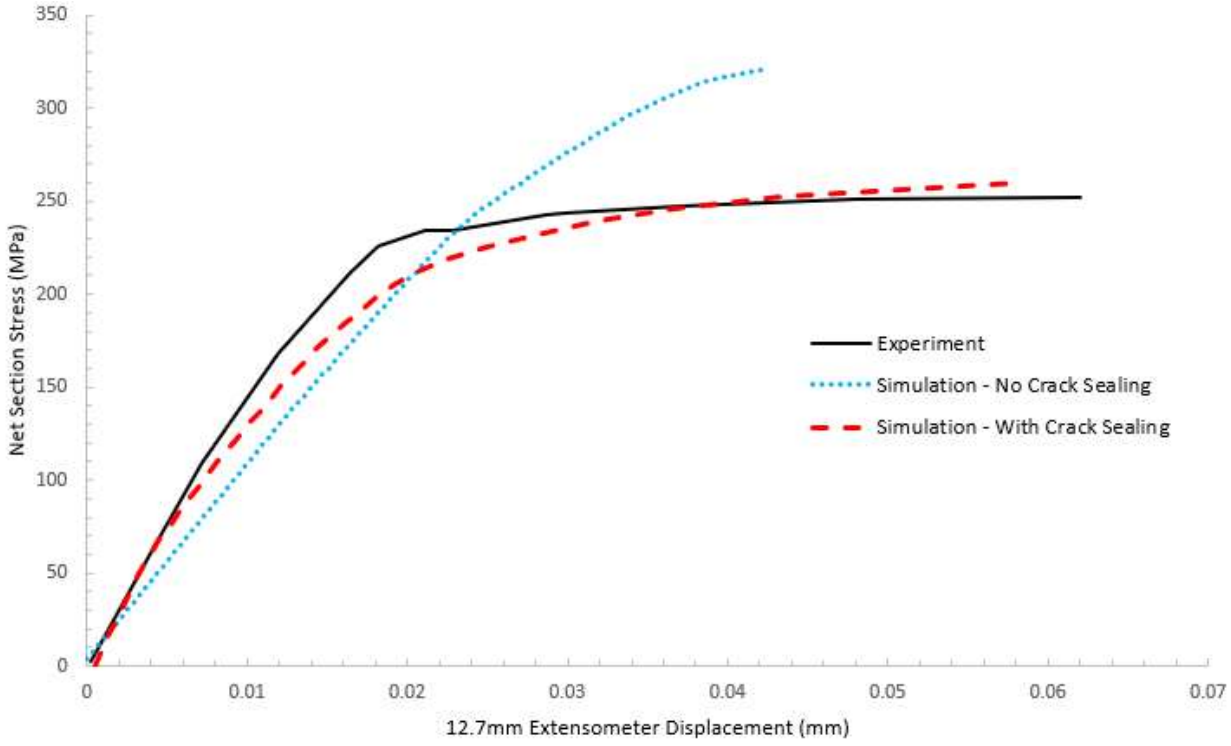

Figure 34 – S200H 1200C $[0,90]_{2s}$ 145 MPa OHT creep 50 hr. interrupted experiment-simulations retained strength stress/strain

During the interrupted test, DIC was used to examine the axial strain near the hole when the net-section stress applied to the specimen reached 145 MPa as well as just before failure. **Figure 35** and **Figure 36** show comparisons of the axial surface strain of the simulation and the DIC. The DIC results were reported as a normalized ratio of local surface strain to the uniform far field strain in the specimen.

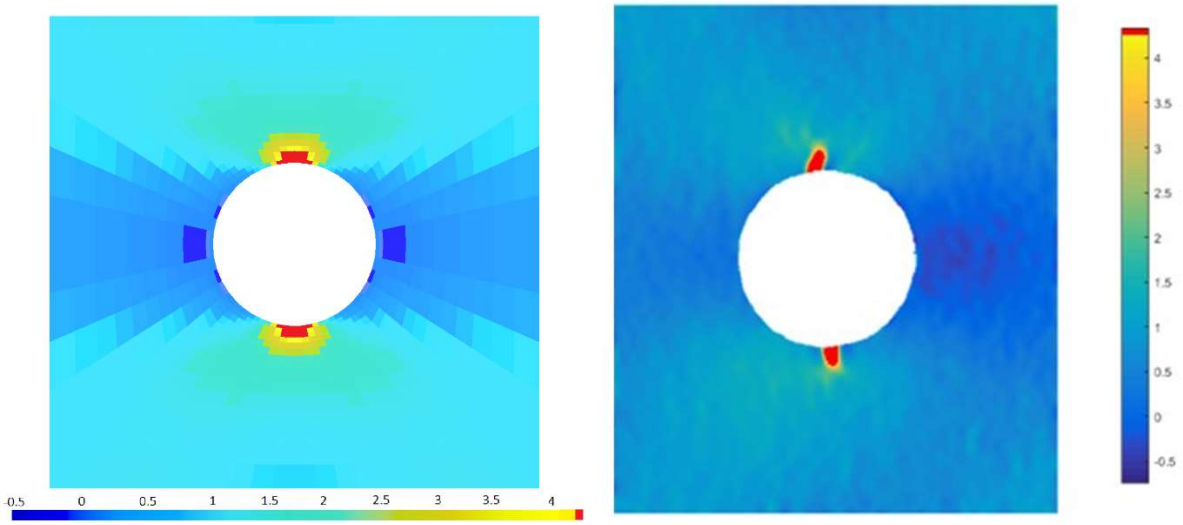

Figure 35 – S200H 1200C $[0,90]_{2s}$ 145 MPa OHT creep 50 hr. interrupted test retained strength axial surface strain simulation (left) and DIC of specimen (right) at 145MPa of reloading

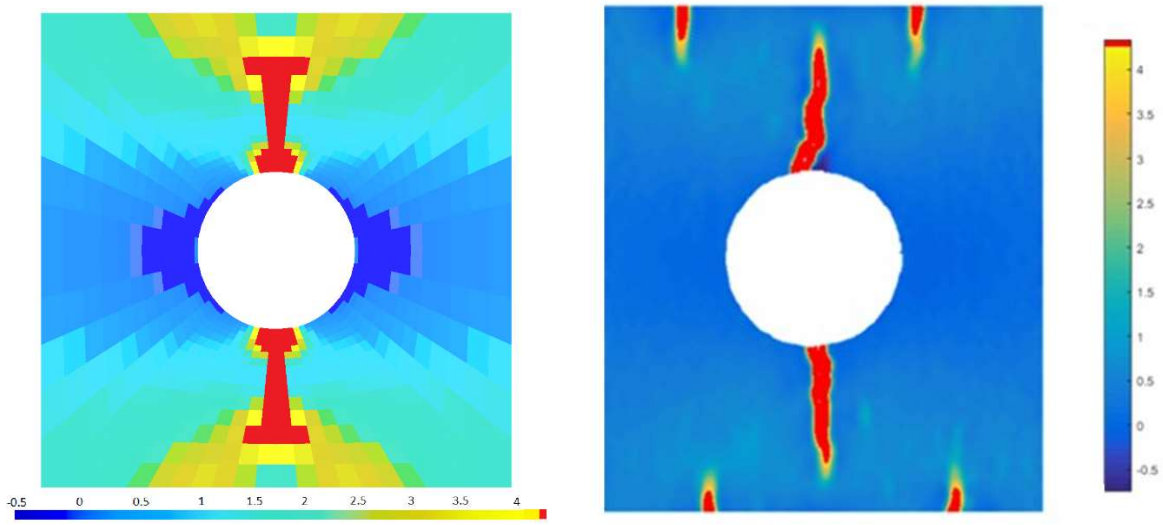

Figure 36 - S200H 1200C $[0,90]_{2s}$ 145 MPa OHT creep 50 hr. interrupted test retained strength axial surface strain simulation (left) and DIC of specimen (right) just before failure

4.7.2. Creep of GEA SMI

The GEA SMI material model detailed in Section 2.5.2.is also employed to model the behavior of GEA SMI under high temperature creep. Creep experiments available for the GEA SMI material system include UNT tests at 1315°C with a $[0,90]_{2s}$ layup at 139 MPa, 178 MPa, and 192 MPa as well as 165 MPa with the $[0,30,60,90]_s$ layup. These experiments come from the

EPPIC program and are modeled macroscopically using the same mesh as in Section 2.5.2. The experiments with the $[0,30,60,90]_s$ layup also include an interrupted test for measuring post-creep retained strength. The $[0,90]_{2s}$ layup creep tests and simulation results are shown in **Figure 37**.

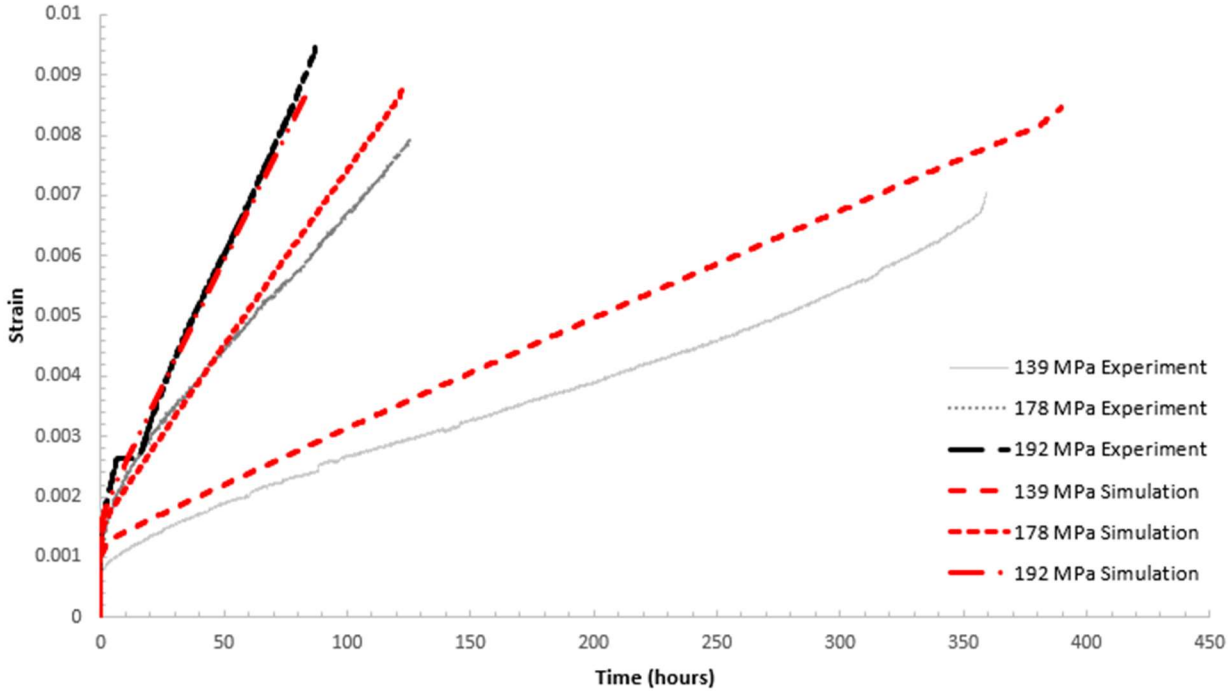

Figure 37 - GEA SMI 1315C [0,90]2s UNT creep experiment-simulation strain/time

A strain vs time curve for the $[0,30,60,90]_s$ 165 MPa UNT creep experiment and simulation can be found in **Figure 38**. The same experiment was repeated but interrupted at 50 hours where the specimen was unloaded, and then reloaded to failure at room temperature. After the experiment was interrupted, the specimen maintained a permanent strain induced by the creep loading of 0.00325 while the simulation predicts a permanent strain of 0.00293 which is 9.9% lower. The reloaded retained strength test can be found in **Figure 39**. Similarly to S200H

material system in interrupted test, without crack sealing or strength reduction, the model overpredicts ductile damage and strength.

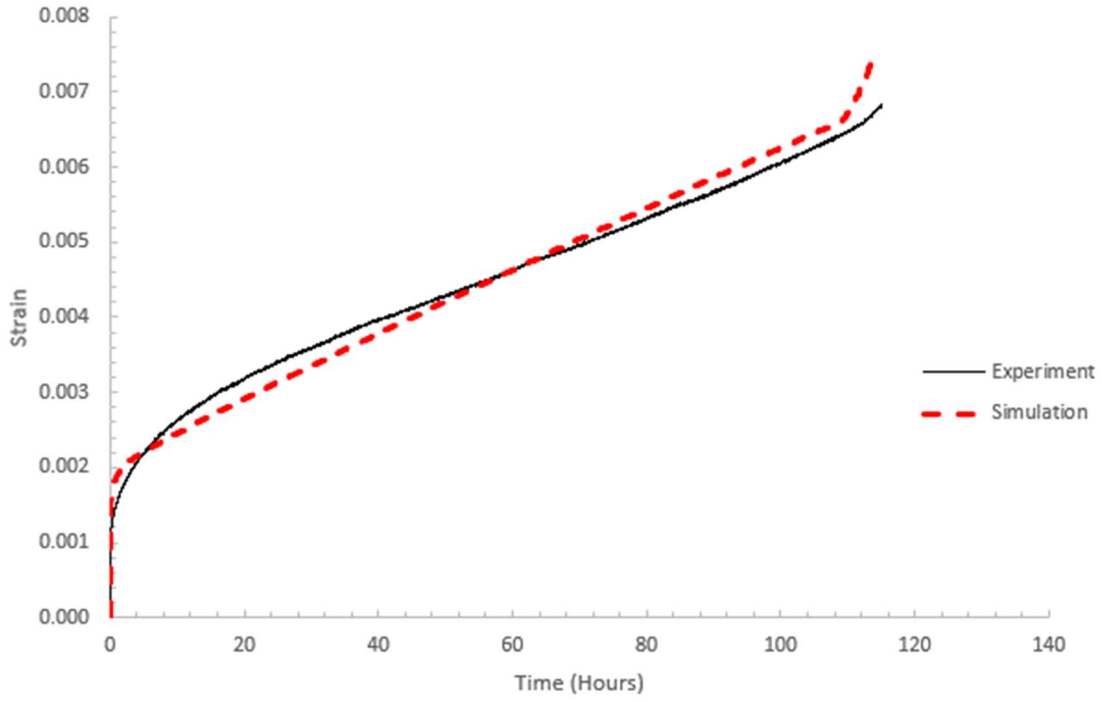

Figure 38 -GEA SMI 1315C [0,30,60,90]S 165 MPa UNT creep experiment-simulation strain/time

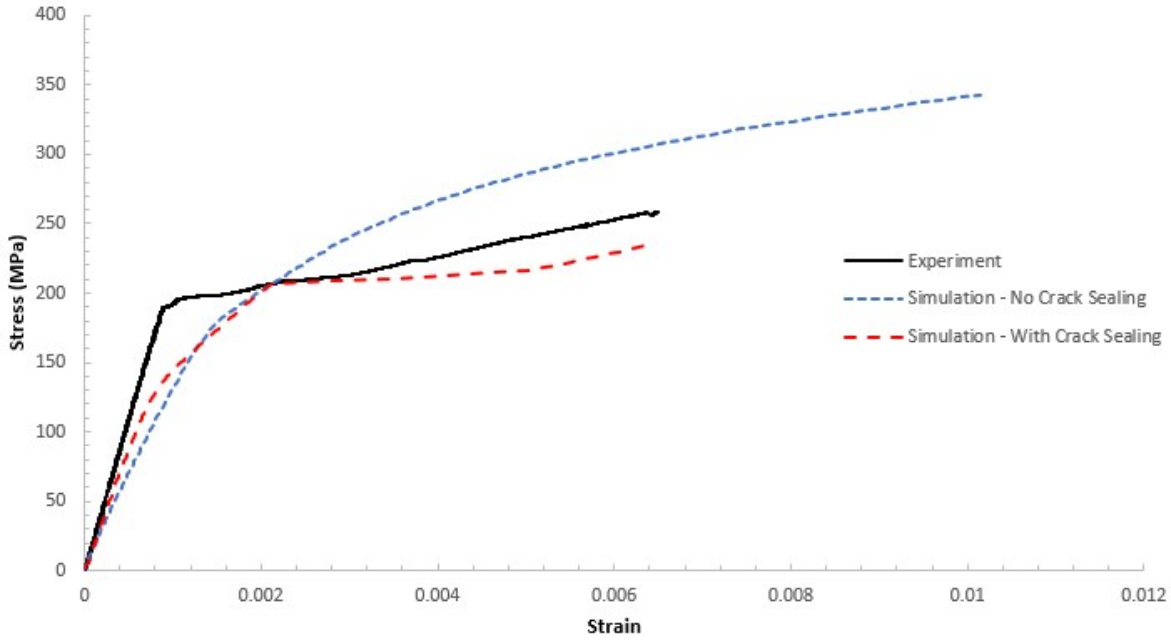

Figure 39 - GEA SMI 1315C [0,30,60,90]S 165 MPa UNT creep 50 hr. interrupted experiment-simulations retained strength stress/strain

Chapter 5: Fatigue Model for High Temperatures

The fatigue model for CMC phases is an extension of the hybrid creep model to cyclic loading. Apart from some specific fatigue damage accumulation features described in section 5.2, the hybrid creep model as outlined in sections 4.1-4.4 defines the material behavior with exception of brittle damage accumulation in high cycle fatigue. Ductile failure is modeled the same way in creep and fatigue, but the viscoplastic failure strain parameter is reduced in fatigue. Since cycle-by-cycle simulation of fatigue is computationally cumbersome, a temporal multiscale technique [92]–[95] is employed by which the damage and viscoplasticity growth rates are calculated at each integration point and then applied over a representative block of cycles.

5.1. Cycle Blocks

Fatigue analysis evolves block by block with ${}^{k}N$ denoting the cycle number corresponding to block *k.* The so-called jump cycle block, which defines the number of cycles over which the rate of ductile or brittle damage growth is kept constant is determined by

$$\Delta N \equiv {}^{k+1}N - {}^{k}N = \min_{Q}\left\{\Delta^{d}N^{Q}, \Delta^{vp}N^{Q}\right\} \tag{69}$$

where $\Delta^{d}N^{Q}$ and $\Delta^{vp}N^{Q}$ are the allowable jump cycles at a quadrature point Q based on the damage and viscoplasticity criteria defined as

$$\begin{aligned}
\Delta^{d}N^{Q} &= \begin{cases} 1 & \max\{\Delta\omega_{I}^{Q}\} \geq \Delta\omega_{\text{tol}} \\ \text{int}\left\{\Delta\omega_{\text{tol}} / \max\{\Delta\omega_{I}^{Q}\}\right\} & \max\{\Delta\omega_{I}^{Q}\} \geq \Delta\omega_{\text{tol}} / \Delta N_{\max} \\ \Delta N_{\max} & \max\{\Delta\omega_{I}^{Q}\} < \Delta\omega_{\text{tol}} / \Delta N_{\max} \end{cases} \\
\Delta^{vp}N^{Q} &= \begin{cases} 1 & \Delta\alpha^{Q} \geq \Delta\alpha_{\text{tol}} \\ \text{int}\left\{\Delta\alpha_{\text{tol}} / \Delta\alpha^{Q}\right\} & \Delta\alpha^{Q} \geq \Delta\alpha_{\text{tol}} / \Delta N_{\max} \\ \Delta N_{\max} & \Delta\alpha^{Q} < \Delta\alpha_{\text{tol}} / \Delta N_{\max} \end{cases}
\end{aligned} \tag{70}$$

where $\Delta\omega_I^Q$ is the change in orthotropic damage variables as defined in Section 2.1 and $\Delta\alpha^Q$ is the change in viscoplastic consistency parameter through one cycle. $\Delta\omega_{\text{tol}}$ is a global parameter controlling the damage change per jump cycle; $\Delta\alpha_{\text{tol}}$ is a global parameter controlling the equivalent viscoplastic strain change per jump cycle, and $\Delta N_{\max}$ is the maximum allowable jump cycle.

Once the size of the jump cycle ΔN is determined, the damage and viscoplastic state in all quadrature points at the start of the next block are updated using the modified forward Euler's method:

$$\begin{aligned} {}^{k+1}\omega_I &= {}^{k}\omega_I + \Delta N\, {}^{k}\Delta\omega_I \\ {}^{k+1}\varepsilon_{ij}^p &= {}^{k}\varepsilon_{ij}^p + \Delta N\, {}^{k}\Delta\varepsilon_{ij}^p \\ {}^{k+1}\alpha &= {}^{k}\alpha + \Delta N\, {}^{k}\Delta\alpha \end{aligned} \tag{71}$$

Figure 40 demonstrates the block cycle technique using the first four blocks of an example one-dimensional creep simulation where only damage is considered. Each cycle consists of four increments. In this example, the first block contains only the first cycle. At the end of the last increment of the cycle, $\Delta\omega$ and ΔN are calculated and because $\Delta N = 1$, the second block begins with the second cycle. After the second cycle's increments are simulated, $\Delta N = 4$ and so the analysis skips to the fifth cycle, the beginning of the third block where damage has been updated as per equation (71). The process is repeated for each block until the analysis is complete.

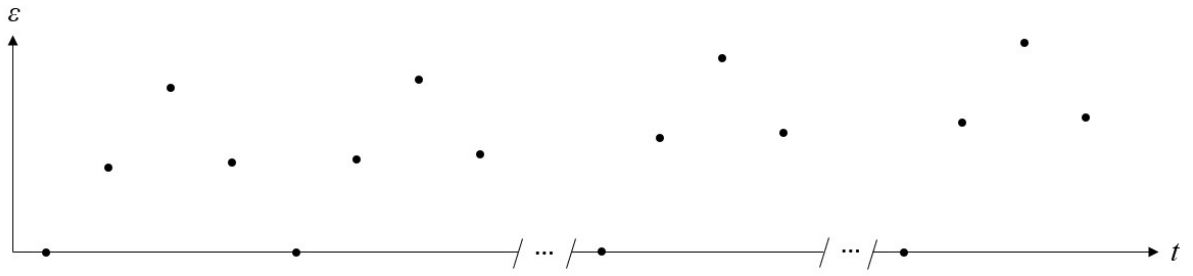

n	1	2	3	4	5	6	7	8
k	1				2			
N	0				1			
ΔN				1				4
ω	0	0.01	0.03	0.03	0.03	0.032	0.034	0.034
Δω				0.03				0.004

9	10	11	12
3			
5			
			150
0.05	0.0501	0.0501	0.0501
			0.0001

13	14	15	16	...
4				...
155				...
			150	...
0.065	0.0651	0.0651	0.0651	...
			0.0001	...

Figure 40 - Cycle block example

5.2. Fatigue Damage Accumulation

Additional damage accumulation than that developed for initial quasi-static and creep loading can be induced by high cycle fatigue loading. This form of brittle damage can develop while the strain state has not yet exceeded the damage threshold. To account for brittle damage accumulation in high cycle fatigue, a power law damage regularization [92] is adopted:

$$\dot{\omega}_I = \left(\frac{G_I(\tilde{\varepsilon}_I, \alpha)}{G_I(\kappa_I, \alpha)} \right)^{\xi_d} \left\langle \dot{G}_I(\tilde{\varepsilon}_I, \alpha) \right\rangle \tag{72}$$

where $\langle x \rangle_+ \equiv \sup\{0, x\}$, ξ_d is a power law exponent. Note that when $\xi_d \to \infty$ (72) reduces to monotonic damage model. In incremental form, the change in damage state variable is:

$${}_{n+1}\Delta\omega_I = \begin{cases} 0 & {}_{n+1}G_I \le {}_nG_I \\ \left({}_{n+1}G_I / {}_n\omega_I \right)^{\xi_d} \left({}_{n+1}G_I - {}_nG_I \right) & {}_nG_I < {}_{n+1}G_I \le {}_n\omega_I \\ {}_{n+1}G_I - {}_n\omega_I & {}_n\omega_I < {}_{n+1}G_I \end{cases} \tag{73}$$

5.3. Stress Update and Consistent Tangent Operator

Given the phase strain ${}_{n+1}\varepsilon_{ij}$ and state variables ${}_{n}\omega_I$, ${}_{n}\varepsilon_{ij}^{p}$, ${}_{n}\alpha$, ${}_{n}G_I$, ${}^{k}\omega_I$, ${}^{k}\varepsilon_{ij}^{p}$, ${}^{k}\alpha$, $\Delta N^{\min}$ where k tracks simulated loading cycles, n tracks loading increments.

1. IF the current increment is the first increment in a loading cycle

I. Replace the damage variable, viscoplastic strain, and equivalent viscoplastic strain with jump cycle augmented values based on jump computed at end of previous cycle:

$$\begin{aligned} {}_{n}\omega_I &= {}^{k}\omega_I + {}^{k}\Delta N^{\min}\,{}^{k}\Delta\omega_I \\ {}_{n}\varepsilon_{ij}^{p} &= {}^{k}\varepsilon_{ij}^{p} + {}^{k}\Delta N^{\min}\,{}^{k}\Delta\varepsilon_{ij}^{p} \\ {}_{n}\alpha &= {}^{k}\alpha + {}^{k}\Delta N^{\min}\,{}^{k}\Delta\alpha \end{aligned} \tag{74}$$

II. Update the loading cycle state variables:

$$\begin{aligned} {}^{k+1}\omega_I &= {}_{n}\omega_I \\ {}^{k+1}\varepsilon_{ij}^{p} &= {}_{n}\varepsilon_{ij}^{p} \\ {}^{k+1}\alpha &= {}_{n}\alpha \end{aligned} \tag{75}$$

III. Reset the value of the minimum jump cycle for this loading cycle:

$${}^{k}\Delta N^{\min} = \Delta N_{\max} \tag{76}$$

2. Compute the elastic strain ${}_{n+1}\varepsilon_{ij}^{e}$ as in equation (56)

3. Determine if analysis is in initial quasi-static or creep regime by checking the simulation time t and comparing it simulation parameters

4A. IF analysis is in initial quasi-static regime:

I. Compute the equivalent strain ${}_{n+1}\tilde{\varepsilon}_I$ as in equation (57)

II. Compute the change in damage variable $\Delta\omega_I$ as in equation (73) where

${}_{n+1}G_I = G_I({}_{n+1}\tilde{\varepsilon}_I, {}_{n}\alpha)$

4B. IF analysis is in creep regime:

I. Compute the equivalent strain ${}_{n+1}\tilde{\varepsilon}_I$ as in equation (57)

II. Compute the change in damage variable ${}_{n+1}\Delta\omega_I$ as in equation (73) where

${}_{n+1}G_I = G_I({}_{n+1}\tilde{\varepsilon}_I, {}_n\alpha)$

III. Update the damage variable:

$$ {}_{n+1}\omega_I = {}_n\omega_I + {}_{n+1}\Delta\omega_I \tag{77} $$

5. Compute the damage-induced constitutive matrix ${}_{n+1}L^{in}_{ijkl}$ per equation (6)

6. Compute the viscoplastic trial state as in equation (60)

7. Solve the consistency equation for the consistency parameter $\Delta\gamma$ as in equations (61) and (62)

8. Update the stress and viscoplastic state variables as in equations (63), (64), (65)

9. Compute the consistent tangent tensor as in equations (66), (67), (68)

10. IF the current increment is the last increment in a loading cycle:

I. Calculate change in damage variable viscoplastic strain, and equivalent viscoplastic strain over cycle:

$$ \begin{aligned} {}^{k+1}\Delta\omega_I &= {}_{n+1}\omega_I - {}^k\omega_I \\ {}^{k+1}\Delta\varepsilon^p_{ij} &= {}_{n+1}\varepsilon^p_{ij} - {}^k\varepsilon^p_{ij} \\ {}^{k+1}\Delta\alpha &= {}_{n+1}\alpha - {}^k\alpha \end{aligned} \tag{78} $$

II. Compute potential jump size for current quadrature point:

$$
{}^{k+1}\Delta^{d}N^{P} = \begin{cases} 1 & \max\{\Delta\omega_I\} \geq \Delta\omega_{\text{tol}} \\ \text{int}\left\{\Delta\omega_{\text{tol}} \middle/ \max\{{}^{k+1}\Delta\omega_I\}\right\} & \max\{\Delta\omega_I\} \geq \Delta\omega_{\text{tol}}/\Delta N_{\max} \\ \Delta N_{\max} & \max\{\Delta\omega_I\} < \Delta\omega_{\text{tol}}/\Delta N_{\max} \end{cases}
$$

$$
{}^{k+1}\Delta^{vp}N^{P} = \begin{cases} 1 & \Delta\alpha \geq \Delta\alpha_{\text{tol}} \\ \text{int}\left\{\Delta\alpha_{\text{tol}} \middle/ {}^{k+1}\Delta\alpha\right\} & \Delta\alpha \geq \Delta\alpha_{\text{tol}}/\Delta N_{\max} \\ \Delta N_{\max} & \Delta\alpha < \Delta\alpha_{\text{tol}}/\Delta N_{\max} \end{cases} \tag{79}
$$

III. Compare potential jump size with minimum jump size from quadrature points previously computed in this increment and update minimum jump size:

$$
{}^{k+1}\Delta N^{\min} = \min\left\{{}^{k+1}\Delta^{d}N^{P}, {}^{k+1}\Delta^{vp}N^{P}, \Delta N^{\min}\right\} \tag{80}
$$

A visualization of this process can be found in **Figure 41**.

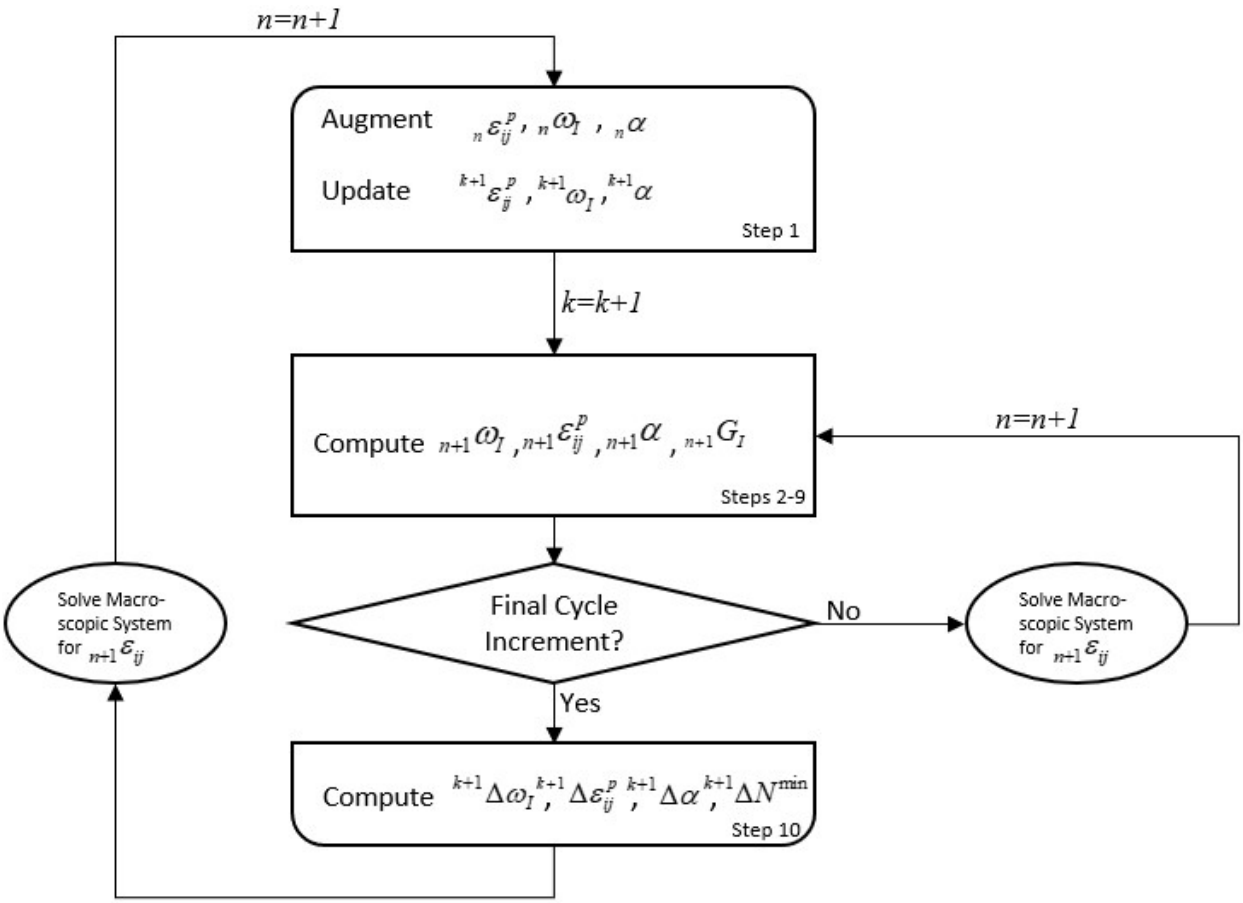

Figure 41 - Fatigue stress update procedure

5.4. Numerical Examples – Fatigue of GEA SMI

The GEA SMI material model used in sections 2.5.2 and 4.7.2 is extended here to model the behavior of GEA SMI under high temperature fatigue. The model parameters for creep are the same except for the reduced fiber viscoplastic failure strain. One set of high temperature fatigue experiments available for the GEA SMI material system is a dataset consisting of cycles/time to failure vs. fatigue stress for a small number of fatigue experiments that were run in a UNT specimen with a $[0,90]_{2s}$ layup at 1315°C at a frequency of 30Hz. Simulations using the symmetrically constrained four layer 8-node hexahedron macroscopic mesh used in previous

GEA SMI simulations were performed and a comparison of the results from those simulations and the experimental data is depicted in **Figure 42**.

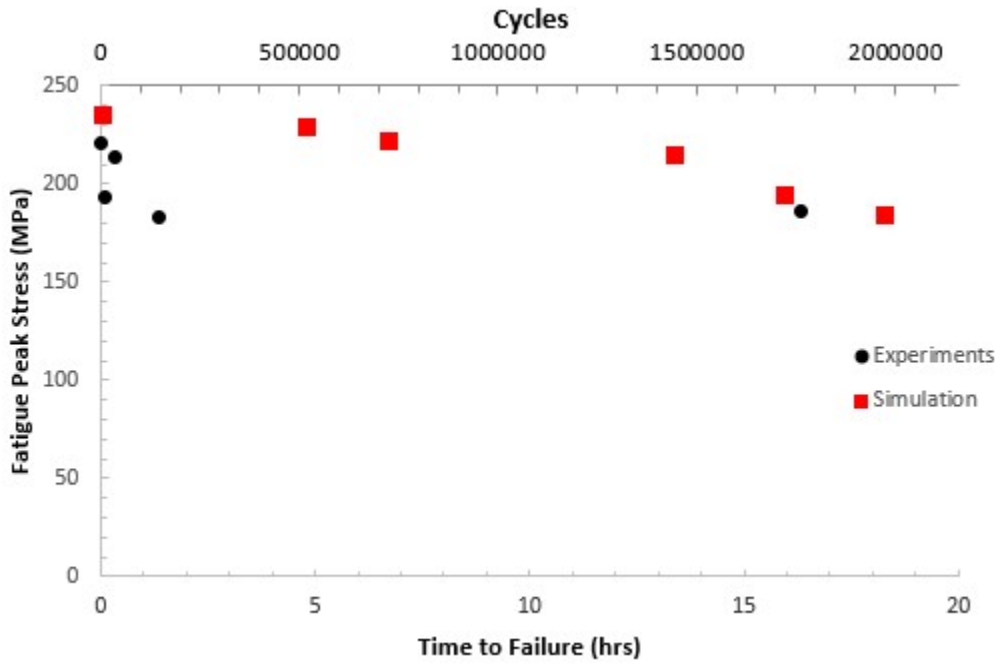

Figure 42 - GEA SMI 1315C $[0,90]_{2s}$ 30Hz fatigue simulation-experiment peak stress vs time/cycles to failure

The other set of high temperature fatigue experiments for GEA SMI is a double notch (DN) fatigue test with the same $[0,30,60,90]_s$ layup seen in the other EPPIC experiments. The experiment is performed with a peak stress of 104 MPa at 1Hz. Like the other EPPIC featured tests, in addition to a fatigue rupture test an interrupted test is performed where after 25 hours of fatigue loading at 1315°C the specimen is loaded until rupture to measure retained strength at room temperature. The dimensions of the DN specimen as shown in **Figure 43** are given in **Table 3**.

Table 3 - DN Dimensions

	mm
Length	150
Width	20
Radius	1.5

Notch Width	3
Notch Depth	3
Thickness	1.778

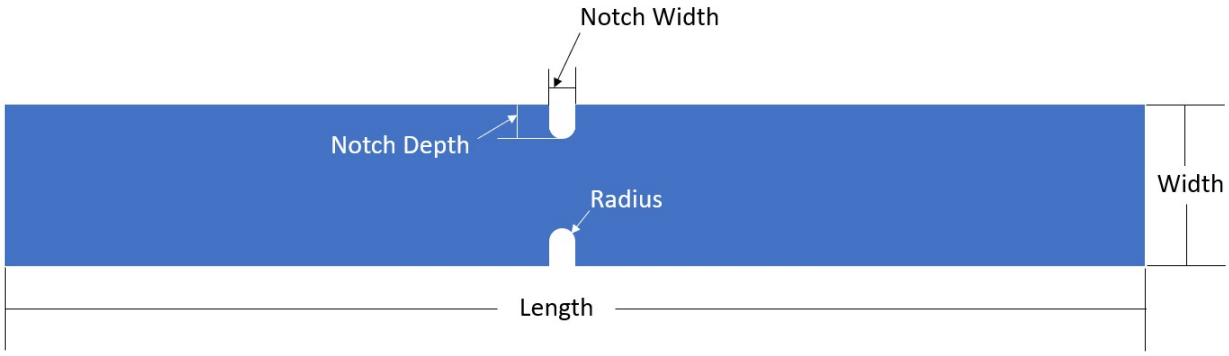

Figure 43 – GEA SMI double notch fatigue specimen

The macroscopic finite element mesh for the DN simulation is meshed with 8-node hexahedrons and utilizes symmetry in three dimensions; it is shown in **Figure 44**.

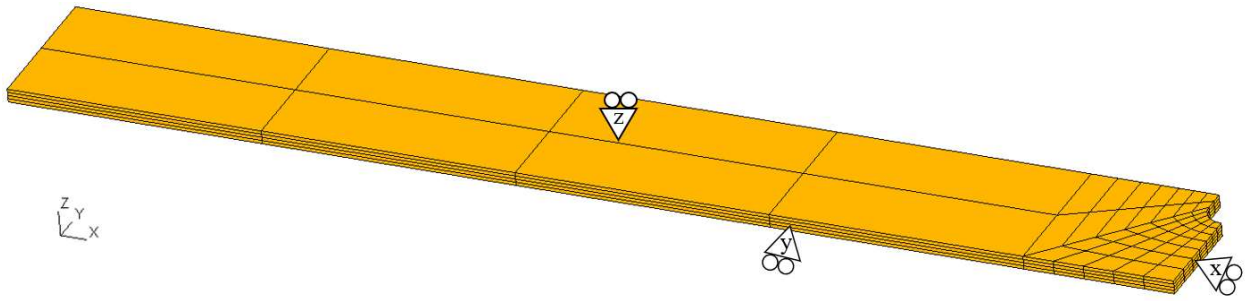

Figure 44 – GEA SMI 1315C double notch macroscopic mesh

An extensometer was placed on the edge of the DN specimen. **Figure 45** shows a comparison of the simulated and experimental extensometer displacement peak during each fatigue cycle vs. the total number of cycles as well as the total time elapsed. It is notable that the experimental peak displacement rises significantly over the last ten hours while the simulated peak displacement does not. Failure in this simulation was determined to be cracking which extends across the surface of the specimen in the axial fibers.

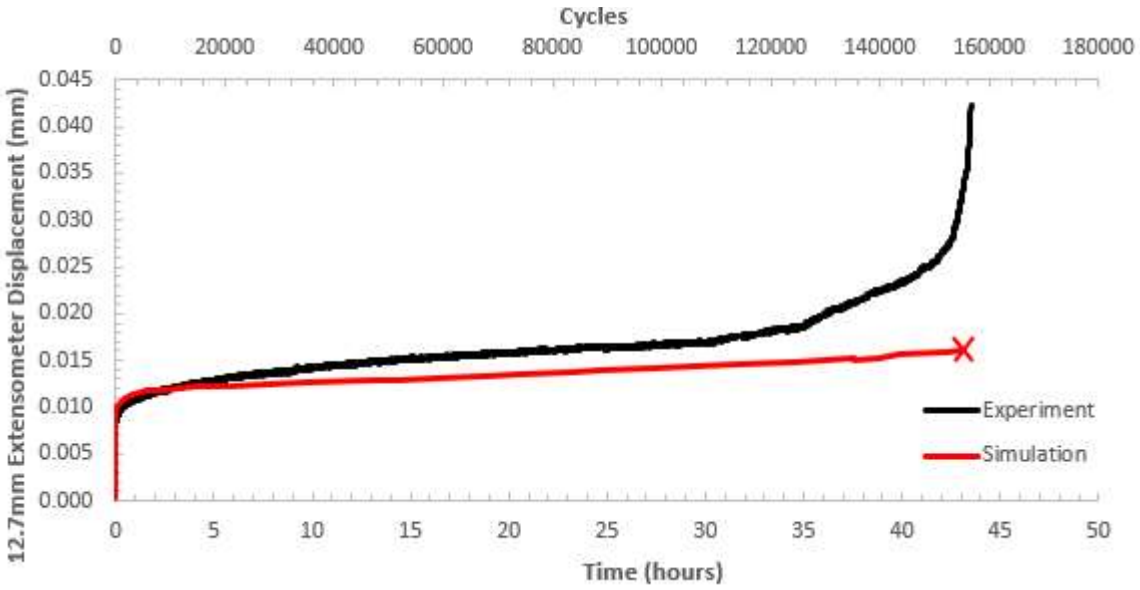

Figure 45 - GEA SMI 1315C $[0,30,60,90]_s$ 104MPa DN fatigue experiment-simulation cycle peak extensometer displacement vs. time/cycles. X indicates failure determined by crack extension across specimen.

Finally, a net-section stress vs. extensometer displacement curve for the interrupted retained strength to failure test can be seen in **Figure 46**. After the fatigue test was interrupted at 25 hours, the specimens showed an average of 0.0075 mm of permanent displacement while the model predicted a permanent displacement of 0.00372 mm. This difference is not due to tertiary fatigue but rather represents an opportunity for the model to be improved. An improvement to the simulated retained strength test via crack sealing and strength reduction is also demonstrated.

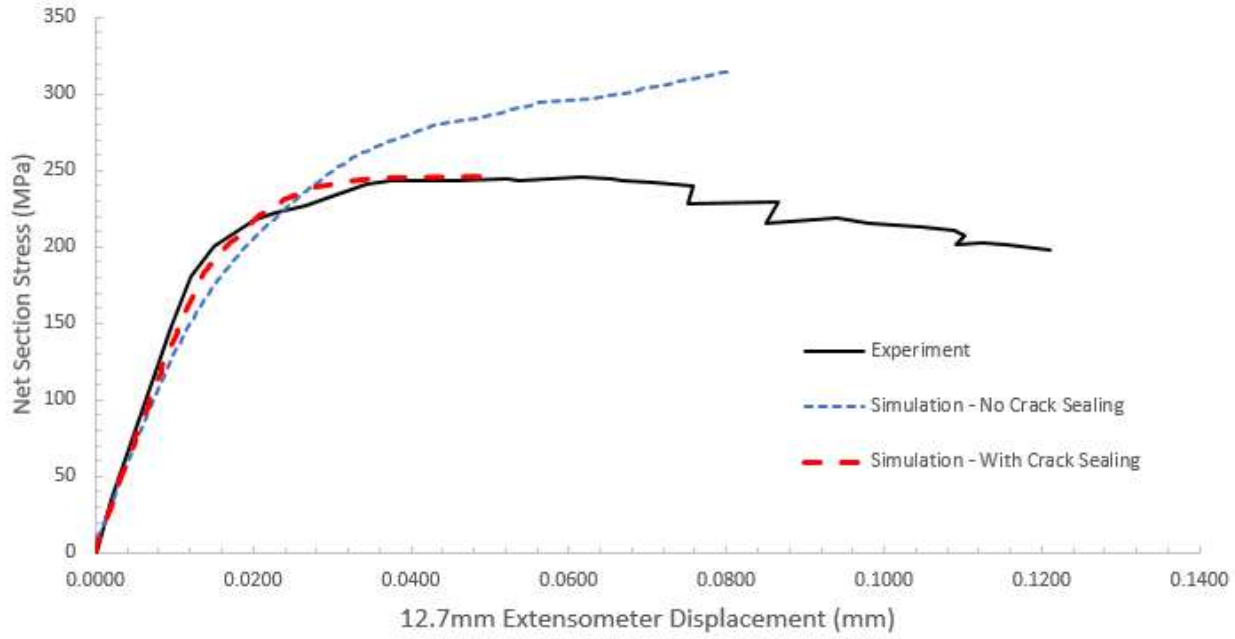

Figure 46 - GEA SMI 1315C $[0,30,60,90]_s$ 104MPa DN interrupted fatigue experiment-simulations retained strength net-section stress vs. extensometer displacement

Chapter 6: Conclusion

A unified computational model has been developed for initial quasi-static, creep, and fatigue loading of SiC/SiC CMCs at high temperatures with oxidation-assisted rupture at intermediate temperatures. The proposed model features reduced order homogenization as a robust and efficient basis for capturing spatial multiscale composite behavior, a continuum damage mechanics model for orthotropic time-independent brittle behavior, a hybrid damage-viscoplasticity model combined with an oxidation-driven crack sealing effect for time-dependent ductile-brittle behavior, a slow crack growth model for tows and fibers which depends on initial matrix pores and subsequent matrix cracking, and a temporal multiscale model for fatigue behavior.

The primary advantage of this model is the unified nature of a single set of material parameters which drive a consistent model that can seamlessly transition between initial quasi-static, creep, and fatigue regimes within the same analysis instance all while capturing the complex material response of CMCs.

The proposed oxidation-assisted rupture model is phenomenological in nature in the sense that diffusion of oxygen and thus availability of oxygen to fibers at multiple scales is not resolved, but rather postulated in terms of initial pores and subsequent load induced microcracks. Yet the proposed model has been shown to possess considerable flexibility to tune the oxygen availability model parameters to fit the highly scattered experimental data.

Building upon the modeling framework demonstrated in this dissertation, there are opportunities for future studies to expand its utility and accuracy. Many of the physical phenomena that lead to the degradation and failure of CMCs occur at the interface between the matrix and fibers. Therefore, incorporating an interphase between the matrix and fiber as part of

the unit cell would offer a modeling space to capture these effects. Further, ROH has the capability of modeling separations between phases which could also be used to model these interfacial phenomena. Extending viscoplasticity into the initial quasi-static regime was briefly explored in developing these models to better capture post high temperature creep and fatigue behavior, and while the crack sealing technique was determined to be a more effective improvement, a viscoplasticity extension could be examined further. A stronger coupling between viscoplasticity and damage might enhance the ability of the model to capture tertiary fatigue as well as the retained strength regime and could be looked at.

In glancing towards the future, if CMCs were to become more accessible to manufacturers, improved modeling techniques need to be developed. Access to high-quality data on the behavior of CMCs is a real barrier to both model development and adoption. Further studies would greatly benefit from the kind of high-quality data that was developed in the EPPIC program and performing similar comprehensive CMC lifing studies is among the highest contributions that could be made to the development of improved CMC modeling capabilities.

References

[1] D. Brewer, “HSR/EPM combustor materials development program,” *Mater. Sci. Eng. A*, vol. 261, no. 1, pp. 284–291, Mar. 1999, doi: 10.1016/S0921-5093(98)01079-X.

[2] I. Spitsberg and J. Steibel, “Thermal and Environmental Barrier Coatings for SiC/SiC CMCs in Aircraft Engine Applications*,” *Int. J. Appl. Ceram. Technol.*, vol. 1, no. 4, pp. 291–301, 2004, doi: 10.1111/j.1744-7402.2004.tb00181.x.

[3] D. Zhu, “Advanced Environmental Barrier Coatings for SiC/SiC Ceramic Matrix Composite Turbine Components,” in *Engineered Ceramics*, John Wiley & Sons, Ltd, 2016, pp. 187–202. doi: 10.1002/9781119100430.ch10.

[4] J. A. DiCarlo, “Advances in SiC/SiC Composites for Aero-Propulsion,” in *Ceramic Matrix Composites*, John Wiley & Sons, Ltd, 2014, pp. 217–235. doi: 10.1002/9781118832998.ch7.

[5] C. Sauder, “Ceramic Matrix Composites: Nuclear Applications,” in *Ceramic Matrix Composites*, John Wiley & Sons, Ltd, 2014, pp. 609–646. doi: 10.1002/9781118832998.ch22.

[6] T. Muroga, M. Gasparotto, and S. J. Zinkle, “Overview of materials research for fusion reactors,” *Fusion Eng. Des.*, vol. 61–62, pp. 13–25, Nov. 2002, doi: 10.1016/S0920-3796(02)00219-3.

[7] A. Kohyama, Y. Katoh, L. L. Snead, and R. H. Jones, “Development of SiC/SiC composite for fusion application,” Art. no. IAEA-CSP--8/C, 2001, Accessed: Aug. 17, 2021. [Online]. Available: http://inis.iaea.org/Search/search.aspx?orig_q=RN:33029026

[8] R. R. Judkins *et al.*, “Development of Ceramic Composite Hot-Gas Filters,” *J. Eng. Gas Turbines Power*, vol. 118, no. 3, pp. 495–499, Jul. 1996, doi: 10.1115/1.2816675.

[9] C. L. Chow and J. Wang, “An anisotropic theory of elasticity for continuum damage mechanics,” *Int. J. Fract.*, vol. 33, no. 1, pp. 3–16, Jan. 1987, doi: 10.1007/BF00034895.

[10] J. Fish, K. Shek, M. Pandheeradi, and M. S. Shephard, "Computational plasticity for composite structures based on mathematical homogenization: Theory and practice," *Comput. Methods Appl. Mech. Eng.*, vol. 148, no. 1, pp. 53–73, Aug. 1997, doi: 10.1016/S0045-7825(97)00030-3.

[11] J. Fish, *Practical Multiscaling*. John Wiley & Sons, 2013.

[12] C. Oskay and J. Fish, "Eigendeformation-based reduced order homogenization for failure analysis of heterogeneous materials," *Comput. Methods Appl. Mech. Eng.*, vol. 196, no. 7, pp. 1216–1243, Jan. 2007, doi: 10.1016/j.cma.2006.08.015.

[13] Z. Yuan and J. Fish, "Hierarchical model reduction at multiple scales," *Int. J. Numer. Methods Eng.*, vol. 79, no. 3, pp. 314–339, 2009, doi: 10.1002/nme.2554.

[14] Z. Yuan and J. Fish, "Multiple scale eigendeformation-based reduced order homogenization," *Comput. Methods Appl. Mech. Eng.*, vol. 198, no. 21, pp. 2016–2038, May 2009, doi: 10.1016/j.cma.2008.12.038.

[15] T. Artz, Z. Yuan, R. Kumar, and J. Fish, "Computational model for oxidation-assisted rupture of ceramic matrix composites," *Int. J. Solids Struct.*, vol. 202, pp. 195–207, Oct. 2020, doi: 10.1016/j.ijsolstr.2020.05.009.

[16] R. S. Kumar, M. Mordasky, G. Ojard, Z. Yuan, and J. Fish, "Notch-strength prediction of ceramic matrix composites using multi-scale continuum damage model," *Materialia*, vol. 6, p. 100267, Jun. 2019, doi: 10.1016/j.mtla.2019.100267.

[17] A. Shojaei, G. Li, J. Fish, and P. J. Tan, "Multi-scale constitutive modeling of Ceramic Matrix Composites by Continuum Damage Mechanics," *Int. J. Solids Struct.*, vol. 51, no. 23, pp. 4068–4081, Nov. 2014, doi: 10.1016/j.ijsolstr.2014.07.026.

[18] L. Marcin, J.-F. Maire, N. Carrère, and E. Martin, "Development of a Macroscopic Damage Model for Woven Ceramic Matrix Composites," *Int. J. Damage Mech.*, vol. 20, no. 6, pp. 939–957, Aug. 2011, doi: 10.1177/1056789510385259.

[19] D. Zhang, P. Meyer, and A. M. Waas, "An experimentally validated computational model for progressive damage analysis of notched oxide/oxide woven ceramic matrix composites," *Compos. Struct.*, vol. 161, pp. 264–274, Feb. 2017, doi: 10.1016/j.compstruct.2016.11.001.

[20] R. S. Kumar, “Micromechanics Approach for the Overall Elastic Properties of Ceramic Matrix Composites Incorporating Defect Structures,” presented at the ASME Turbo Expo 2020: Turbomachinery Technical Conference and Exposition, Jan. 2021. doi: 10.1115/GT2020-16056.

[21] D. Tal and J. Fish, “Generating a statistically equivalent representative volume element with discrete defects,” *Compos. Struct.*, vol. 153, pp. 791–803, Oct. 2016, doi: 10.1016/j.compstruct.2016.06.077.

[22] T. Skinner and A. Chattopadhyay, “Multiscale temperature-dependent ceramic matrix composite damage model with thermal residual stresses and manufacturing-induced damage,” *Compos. Struct.*, vol. 268, p. 114006, Jul. 2021, doi: 10.1016/j.compstruct.2021.114006.

[23] R. Haj-Ali and J. Aboudi, “A new and general formulation of the parametric HFGMC micromechanical method for two and three-dimensional multi-phase composites,” *Int. J. Solids Struct.*, vol. 50, no. 6, pp. 907–919, Mar. 2013, doi: 10.1016/j.ijsolstr.2012.11.009.

[24] B. A. A. Bednarcyk, “MAC/GMC 4.0 User’s Manual: Keywords Manual. Volume 2,” Dec. 2002. Accessed: Apr. 24, 2020. [Online]. Available: https://ntrs.nasa.gov/search.jsp?R=20030014606

[25] B. A. A. Bednarcyk, “MAC/GMC 4.0 User’s Manual: Example Problem Manual. Volume 3,” Dec. 2002. Accessed: Apr. 24, 2020. [Online]. Available: https://ntrs.nasa.gov/search.jsp?R=20030015411

[26] B. A. Bednarcyk, S. K. Mital, E. J. Pineda, and S. M. Arnold, “Multiscale Modeling of Ceramic Matrix Composites,” presented at the AIAA SciTech 2015, Kissimmee, Fl, Jan. 2015. Accessed: Aug. 17, 2021. [Online]. Available: https://ntrs.nasa.gov/citations/20150002079

[27] N. N. M. Nemeth, “Stochastic-Strength-Based Damage Simulation of Ceramic Matrix Composite Laminates,” Oct. 2016. Accessed: Jul. 17, 2019. [Online]. Available: https://ntrs.nasa.gov/search.jsp?R=20160013709

[28] S. Darzens, J.-L. Chermant, and J. Vicens, “First results on SiCf-SiBC creep,” *Scr. Mater.*, vol. 43, no. 6, pp. 497–502, Aug. 2000, doi: 10.1016/S1359-6462(00)00451-6.

[29] K. L. Rugg, R. E. Tressler, and J. Lamon, "Interfacial behavior of microcomposites during creep at elevated temperatures," *J. Eur. Ceram. Soc.*, vol. 19, no. 13, pp. 2297–2303, Oct. 1999, doi: 10.1016/S0955-2219(99)00117-X.

[30] G. N. Morscher *et al.*, "Tensile creep and fatigue of Sylramic-iBN melt-infiltrated SiC matrix composites: Retained properties, damage development, and failure mechanisms," *Compos. Sci. Technol.*, vol. 68, no. 15, pp. 3305–3313, Dec. 2008, doi: 10.1016/j.compscitech.2008.08.028.

[31] S. Zhu, M. Mizuno, Y. Nagano, J. Cao, Y. Kagawa, and H. Kaya, "Creep and Fatigue Behavior in an Enhanced SiC/SiC Composite at High Temperature," *J. Am. Ceram. Soc.*, vol. 81, no. 9, pp. 2269–2277, 1998, doi: 10.1111/j.1151-2916.1998.tb02621.x.

[32] J. A. DiCarlo, H. M. Yun, and J. B. Hurst, "Fracture mechanisms for SiC fibers and SiC/SiC composites under stress-rupture conditions at high temperatures," *Appl. Math. Comput.*, vol. 152, no. 2, pp. 473–481, May 2004, doi: 10.1016/S0096-3003(03)00570-8.

[33] T. E. Steyer, F. W. Zok, and D. P. Walls, "Stress Rupture of an Enhanced Nicalon/Silicon Carbide Composite at Intermediate Temperatures," *J. Am. Ceram. Soc.*, vol. 81, no. 8, pp. 2140–2146, 1998, doi: 10.1111/j.1151-2916.1998.tb02598.x.

[34] G. N. Morscher, J. Hurst, and D. Brewer, "Intermediate-Temperature Stress Rupture of a Woven Hi-Nicalon, BN-Interphase, SiC-Matrix Composite in Air," *J. Am. Ceram. Soc.*, vol. 83, no. 6, pp. 1441–1449, 2000, doi: 10.1111/j.1151-2916.2000.tb01408.x.

[35] A. G. Evans, F. W. Zok, R. M. McMeeking, and Z. Z. Du, "Models of High-Temperature, Environmentally Assisted Embrittlement in Ceramic-Matrix Composites," *J. Am. Ceram. Soc.*, vol. 79, no. 9, pp. 2345–2352, 1996, doi: 10.1111/j.1151-2916.1996.tb08982.x.

[36] F. E. Heredia, J. C. McNulty, F. W. Zok, and A. G. Evans, "Oxidation Embrittlement Probe for Ceramic-Matrix Composites," *J. Am. Ceram. Soc.*, vol. 78, no. 8, pp. 2097–2100, 1995, doi: 10.1111/j.1151-2916.1995.tb08621.x.

[37] S. Mall and J. L. Ryba, "Effects of moisture on tensile stress rupture behavior of a SiC/SiC composite at elevated temperatures," *Compos. Sci. Technol.*, vol. 68, no. 1, pp. 274–282, Jan. 2008, doi: 10.1016/j.compscitech.2007.03.005.

[38] W. Xu, F. W. Zok, and R. M. McMeeking, “Model of Oxidation-Induced Fiber Fracture in SiC/SiC Composites,” *J. Am. Ceram. Soc.*, vol. 97, no. 11, pp. 3676–3683, 2014, doi: 10.1111/jace.13180.

[39] R. M. Sullivan, “A Numerical Solution Routine for Investigating Oxidation-Induced Strength Degradation Mechanisms in SiC/SiC Composites,” Oct. 04, 2015. Accessed: Jul. 17, 2019. [Online]. Available: https://ntrs.nasa.gov/search.jsp?R=20150023066

[40] R. M. Sullivan, “Time-Dependent Stress Rupture Strength Degradation of Hi-Nicalon Fiber-Reinforced Silicon Carbide Composites at Intermediate Temperatures,” Jan. 2016. Accessed: Jul. 17, 2019. [Online]. Available: https://ntrs.nasa.gov/search.jsp?R=20160001159

[41] H.-T. Lin and P. F. Becher, “Effect of fiber coating on lifetime of Nicalon fiber-silicon carbide composites in air,” *Mater. Sci. Eng. A*, vol. 231, no. 1, pp. 143–150, Jul. 1997, doi: 10.1016/S0921-5093(97)00079-8.

[42] L. U. J. T. Ogbuji, “Recent Developments in the Environmental Durability of Sic/sic Composites,” Jul. 2002. Accessed: Nov. 05, 2019. [Online]. Available: https://ntrs.nasa.gov/search.jsp?R=20020070893

[43] W. H. Glime and J. D. Cawley, “Stress Concentration Due to Fiber-Matrix Fusion in Ceramic-Matrix Composites,” *J. Am. Ceram. Soc.*, vol. 81, no. 10, pp. 2597–2604, 1998, doi: 10.1111/j.1151-2916.1998.tb02666.x.

[44] N. Iyengar and W. A. Curtin, “Time-dependent failure in fiber-reinforced composites by fiber degradation,” *Acta Mater.*, vol. 45, no. 4, pp. 1489–1502, Apr. 1997, doi: 10.1016/S1359-6454(96)00260-1.

[45] W. Gauthier, F. Pailler, J. Lamon, and R. Pailler, “Oxidation of Silicon Carbide Fibers During Static Fatigue in Air at Intermediate Temperatures,” *J. Am. Ceram. Soc.*, vol. 92, no. 9, pp. 2067–2073, 2009, doi: 10.1111/j.1551-2916.2009.03180.x.

[46] P. Forio, F. Lavaire, and J. Lamon, “Delayed Failure at Intermediate Temperatures (600°–700°C) in Air in Silicon Carbide Multifilament Tows,” *J. Am. Ceram. Soc.*, vol. 87, no. 5, pp. 888–893, 2004, doi: 10.1111/j.1551-2916.2004.00888.x.

[47] T. A. Parthasarathy, B. Cox, O. Sudre, C. Przybyla, and M. K. Cinibulk, "Modeling environmentally induced property degradation of SiC/BN/SiC ceramic matrix composites," *J. Am. Ceram. Soc.*, vol. 101, no. 3, pp. 973–997, Mar. 2018, doi: 10.1111/jace.15325.

[48] C. Cluzel, E. Baranger, P. Ladevèze, and A. Mouret, "Mechanical behaviour and lifetime modelling of self-healing ceramic-matrix composites subjected to thermomechanical loading in air," *Compos. Part Appl. Sci. Manuf.*, vol. 40, no. 8, pp. 976–984, Aug. 2009, doi: 10.1016/j.compositesa.2008.10.020.

[49] M. Genet, L. Marcin, E. Baranger, C. Cluzel, P. Ladevèze, and A. Mouret, "Computational prediction of the lifetime of self-healing CMC structures," *Compos. Part Appl. Sci. Manuf.*, vol. 43, no. 2, pp. 294–303, Feb. 2012, doi: 10.1016/j.compositesa.2011.11.004.

[50] K. L. Rugg, R. E. Tressler, C. E. Bakis, and J. Lamon, "Creep of SiC–SiC microcomposites," *J. Eur. Ceram. Soc.*, vol. 19, no. 13, pp. 2285–2296, Oct. 1999, doi: 10.1016/S0955-2219(99)00118-1.

[51] A. G. Evans and C. Weber, "Creep damage in SiC/SiC composites," *Mater. Sci. Eng. A*, vol. 208, no. 1, pp. 1–6, Apr. 1996, doi: 10.1016/0921-5093(95)09867-4.

[52] M. R. Begley, A. G. Evans, and R. M. McMeeking, "Creep rupture in ceramic matrix composites with creeping fibers," *J. Mech. Phys. Solids*, vol. 43, no. 5, pp. 727–740, May 1995, doi: 10.1016/0022-5096(95)00006-5.

[53] J. Henager and R. H. Jones, "High-temperature plasticity effects in bridged cracks and subcritical crack growth in ceramic composites," *Mater. Sci. Eng. Struct. Mater. Prop. Microstruct. Process. Switz.*, vol. 166:1–2, Jul. 1993, Accessed: Aug. 17, 2021. [Online]. Available: https://www.osti.gov/etdeweb/biblio/5382932

[54] Z. Luo, H. Cao, H. Ren, and X. Zhou, "Tension-tension fatigue behavior of a PIP SiC/SiC composite at elevated temperature in air," *Ceram. Int.*, vol. 42, no. 2, Part B, pp. 3250–3260, Feb. 2016, doi: 10.1016/j.ceramint.2015.10.116.

[55] M. Ruggles-Wrenn, N. Boucher, and C. Przybyla, "Fatigue of three advanced SiC/SiC ceramic matrix composites at 1200°C in air and in steam," *Int. J. Appl. Ceram. Technol.*, vol. 15, no. 1, pp. 3–15, 2018, doi: 10.1111/ijac.12773.

[56] M. B. Ruggles-Wrenn, D. T. Christensen, A. L. Chamberlain, J. E. Lane, and T. S. Cook, "Effect of frequency and environment on fatigue behavior of a CVI SiC/SiC ceramic matrix composite at 1200°C," *Compos. Sci. Technol.*, vol. 71, no. 2, pp. 190–196, Jan. 2011, doi: 10.1016/j.compscitech.2010.11.008.

[57] M. Mizuno, S. Zhu, Y. Nagano, Y. Sakaida, Y. Kagawa, and M. Watanabe, "Cyclic-Fatigue Behavior of SiC/SiC Composites at Room and High Temperatures," *J. Am. Ceram. Soc.*, vol. 79, no. 12, pp. 3065–3077, 1996, doi: 10.1111/j.1151-2916.1996.tb08078.x.

[58] F. Rebillat, A. Guette, L. Espitalier, C. Debieuvre, and R. Naslain, "Oxidation resistance of SiC/SiC micro and minicomposites with a highly crystallised BN interphase," *J. Eur. Ceram. Soc.*, vol. 18, no. 13, pp. 1809–1819, Nov. 1998, doi: 10.1016/S0955-2219(98)00120-4.

[59] J. Lamon, "Chemical Vapor Infiltrated SiC/SiC Composites (CVI SiC/SiC)," in *Handbook of Ceramic Composites*, N. Bansal, Ed. Kluwer Academic Publishers, 2005, pp. 55–76.

[60] C. I. Contescu, "Initial assessment of environmental effects on SiC/SiC composites in helium-cooled nuclear systems," ORNL/TM-2013/319, 1096306, Sep. 2013. doi: 10.2172/1096306.

[61] E. Jin *et al.*, "Effect of Interface Coating on High Temperature Mechanical Properties of SiC–SiC Composite Using Domestic Hi–Nicalon Type SiC Fibers," *Coatings*, vol. 10, no. 5, Art. no. 5, May 2020, doi: 10.3390/coatings10050477.

[62] A. S. Almansour and G. N. Morscher, "Tensile creep behavior of SiCf/SiC ceramic matrix minicomposites," *J. Eur. Ceram. Soc.*, vol. 40, no. 15, pp. 5132–5146, Dec. 2020, doi: 10.1016/j.jeurceramsoc.2020.07.012.

[63] X. Jing, Z. Cheng, H. Niu, X. Yang, and D. Shi, "Deformation and rupture behaviors of SiC/SiC under creep, fatigue and dwell-fatigue load at 1300 °C," *Ceram. Int.*, vol. 45, no. 17, Part A, pp. 21440–21447, Dec. 2019, doi: 10.1016/j.ceramint.2019.07.134.

[64] K. H. Khafagy, C. Sorini, T. Skinner, and A. Chattopadhyay, "Modeling creep behavior in ceramic matrix composites," *Ceram. Int.*, vol. 47, no. 9, pp. 12651–12660, May 2021, doi: 10.1016/j.ceramint.2021.01.125.

[65] M. Grujicic, R. Galgalikar, J. S. Snipes, and S. Ramaswami, "Material Constitutive Models for Creep and Rupture of SiC/SiC Ceramic-Matrix Composites (CMCs) Under Multiaxial Loading," *J. Mater. Eng. Perform.*, vol. 25, no. 5, pp. 1697–1708, May 2016, doi: 10.1007/s11665-016-2036-1.

[66] S. M. Arnold, F. A. Holland, B. A. Bednarcyk, and E. J. Pineda, "Combining material and model pedigree is foundational to making ICME a reality," *Integrating Mater. Manuf. Innov.*, vol. 4, no. 1, pp. 37–62, Dec. 2015, doi: 10.1186/s40192-015-0031-2.

[67] J. Aboudi, S. M. Arnold, and B. A. Bednarcyk, "Chapter 7 - Multiscale Modeling of Composites," in *Micromechanics of Composite Materials*, J. Aboudi, S. M. Arnold, and B. A. Bednarcyk, Eds. Oxford: Butterworth-Heinemann, 2013, pp. 447–540. doi: 10.1016/B978-0-12-397035-0.00007-0.

[68] J. Lamon and A. Laforêt, "Static Fatigue of SiC/SiC Minicomposites at High Temperatures Up to 1200 °C in Air: Multiscale Approach," *J. Compos. Sci.*, vol. 5, no. 3, Art. no. 3, Mar. 2021, doi: 10.3390/jcs5030067.

[69] L. Longbiao, "A hysteresis energy dissipation based model for multiple loading damage in continuous fiber-reinforced ceramic-matrix composites," *Compos. Part B Eng.*, vol. 162, pp. 259–273, Apr. 2019, doi: 10.1016/j.compositesb.2018.11.012.

[70] S. Arnold and P. M. and B. B. Subodh Mital, "Multiscale Modeling of Random Microstructures in SiC/SiC Ceramic Matrix Composites within MAC/GMC Framework," *Proc. Am. Soc. Compos. Thirty-First Tech. Conf.*, vol. 0, no. 0, Art. no. 0, 2016, Accessed: Aug. 17, 2021. [Online]. Available: http://dpi-proceedings.com/index.php/asc31/article/view/3144

[71] L. Zhang, R. Qiu, J. Cheng, and B. Liu, "Experimental investigation and multiscale simulation on the bending fatigue of 2D SiCf/SiC composites," *Int. J. Fatigue*, vol. 144, p. 106051, Mar. 2021, doi: 10.1016/j.ijfatigue.2020.106051.

[72] J. Zheng, P. Zhang, D. Zhang, and D. Jiang, "A Multi-Scale Submodel Method for Fatigue Analysis of Braided Composite Structures," *Materials*, vol. 14, no. 15, Art. no. 15, Jan. 2021, doi: 10.3390/ma14154190.

[73] J. Fish and Y. Yu, “A PSEUDO-NONLOCAL FINITE ELEMENT FOR EFFICIENT SOLUTION OF COMPUTATIONALLY DEMANDING MATERIAL MODELS,” *Int. J. Multiscale Comput. Eng.*, vol. 19, 2021, doi: 10.1615/IntJMultCompEng.2021040102.

[74] G. Jefferson, C. Przybyla, and L. Zawada, “Assessment of Damage Progression Models For SiC/SiC Ceramic Matrix Composites,” *Int. J. Multiscale Comput. Eng.*, Dec. 2021.

[75] G. Corman and K. Luthra, “Melt Infiltrated Ceramic Composites (Hipercomp) for Gas Turbine Engine Applications,” Tiax Llc, Sep. 2005. doi: 10.2172/936318.

[76] T. T. Kim, S. Mall, and L. P. Zawada, “Fatigue Behavior of Hi-Nicalon Type-S^{TM}/BN/SiC Ceramic Matrix Composites in a Combustion Environment,” *Int. J. Appl. Ceram. Technol.*, vol. 8, no. 2, pp. 261–272, 2011, doi: 10.1111/j.1744-7402.2010.02558.x.

[77] M. van Roode, A. K. Bhattacharya, M. K. Ferber, and F. Abdi, “Creep Resistance and Water Vapor Degradation of SiC/SiC Ceramic Matrix Composite Gas Turbine Hot Section Components,” Dec. 2010, pp. 455–469. doi: 10.1115/GT2010-23012.

[78] J. Lemaitre and J. L. Chaboche, “ASPECT PHENOMENOLOGIQUE DE LA RUPTURE PAR ENDOMMAGEMENT,” *J MEC APPL*, vol. 2, no. 3, 1978, Accessed: Nov. 04, 2019. [Online]. Available: https://trid.trb.org/view.aspx?id=1048150

[79] F. Sidoroff, “Description of Anisotropic Damage Application to Elasticity,” in *Physical Non-Linearities in Structural Analysis*, Berlin, Heidelberg, 1981, pp. 237–244. doi: 10.1007/978-3-642-81582-9_35.

[80] J. Mazars, “APPLICATION DE LA MECANIQUE DE L’ENDOMMAGEMENT AU COMPORTEMENT NON LINEAIRE ET A LA RUPTURE DU BETON DE STRUCTURE,” *THESE Dr. ES Sci. Present. Univ. PIERRE MARIE CURIE - PARIS 6*, May 1984, Accessed: Nov. 04, 2019. [Online]. Available: https://trid.trb.org/view/1032710

[81] Y. Liu *et al.*, “A regularized phenomenological multiscale damage model,” *Int. J. Numer. Methods Eng.*, vol. 99, no. 12, pp. 867–887, 2014, doi: 10.1002/nme.4705.

[82] G. Duvaut and J. L. Lions, *Inequalities in Mechanics and Physics*. Springer-Verlag, 1976.

[83] Altair Engineering, “Multiscale Designer 3.4 User Manual.” Troy, MI, USA, 2018.

[84] Z. Yuan, “The Multiscale Damage Mechanics in Objected-oriented Fortran Framework,” Columbia University, 2016. doi: 10.7916/D8KS6RCJ.
[85] U. Santhosh, Y. Gowayed, G. Ojard, I. Smyth, S. Kalarikkal, and G. Jefferson, “Quantification of Porosity in Ceramic Matrix Composites Using Thermography,” *J. Nondestruct. Eval.*, vol. 37, no. 2, p. 37, May 2018, doi: 10.1007/s10921-018-0487-z.
[86] P. Del Puglia, M. A. Sheikh, and D. R. Hayhurst, “Classification and quantification of initial porosity in a CMC laminate,” *Compos. Part Appl. Sci. Manuf.*, vol. 35, no. 2, pp. 223–230, Feb. 2004, doi: 10.1016/j.compositesa.2003.09.026.
[87] W. Gauthier and J. Lamon, “Delayed Failure of Hi-Nicalon and Hi-Nicalon S Multifilament Tows and Single Filaments at Intermediate Temperatures (500°–800°C),” *J. Am. Ceram. Soc.*, vol. 92, no. 3, pp. 702–709, 2009, doi: 10.1111/j.1551-2916.2009.02924.x.
[88] P. Perzyna, “Fundamental Problems in Viscoplasticity,” in *Advances in Applied Mechanics*, vol. 9, G. G. Chernyi, H. L. Dryden, P. Germain, L. Howarth, W. Olszak, W. Prager, R. F. Probstein, and H. Ziegler, Eds. Elsevier, 1966, pp. 243–377. doi: 10.1016/S0065-2156(08)70009-7.
[89] D. Perić, “On a class of constitutive equations in viscoplasticity: Formulation and computational issues,” *Int. J. Numer. Methods Eng.*, vol. 36, no. 8, pp. 1365–1393, 1993, doi: https://doi.org/10.1002/nme.1620360807.
[90] J. C. Simo and R. L. Taylor, “Consistent tangent operators for rate-independent elastoplasticity,” *Comput. Methods Appl. Mech. Eng.*, vol. 48, no. 1, pp. 101–118, Feb. 1985, doi: 10.1016/0045-7825(85)90070-2.
[91] E. D. S. Neto, D. Perić, and D. Owen, “Viscoplasticity,” in *Computational Methods for Plasticity*, John Wiley & Sons, Ltd, 2008, pp. 435–470. doi: 10.1002/9780470694626.ch11.
[92] J. Fish and Q. Yu, “Computational mechanics of fatigue and life predictions for composite materials and structures,” *Comput. Methods Appl. Mech. Eng.*, vol. 191, no. 43, pp. 4827–4849, Sep. 2002, doi: 10.1016/S0045-7825(02)00401-2.
[93] C. Oskay and J. Fish, “Fatigue life prediction using 2-scale temporal asymptotic homogenization,” *Int. J. Numer. Methods Eng.*, vol. 61, no. 3, pp. 329–359, 2004, doi: 10.1002/nme.1069.
[94] J. Fish, M. Bailakanavar, L. Powers, and T. Cook, “Multiscale fatigue life prediction model for heterogeneous materials,” *Int. J. Numer. Methods Eng.*, vol. 91, no. 10, pp. 1087–1104, 2012, doi: 10.1002/nme.4307.
[95] C. Oskay and J. Fish, “Multiscale Modeling of Fatigue for Ductile Materials,” *Int. J. Multiscale Comput. Eng.*, vol. 2, no. 3, 2004, doi: 10.1615/IntJMultCompEng.v2.i3.10.

Contents of this dissertation have been reprinted from:

International Journal for Multiscale Computational Engineering, Special Issue: Assessment of Damage Progression Models for SiC/SiC Ceramic Matrix Composites, T. Artz and J. Fish, *A Unified Approach to Computational Modeling of Ceramic Matrix Composites Under High*

Temperature Creep, Fatigue, and Initial Quasi-Static Loading, Copyright 2021, with permission from Begell house, Inc.

International Journal of Solids and Structures, Volume 202, T. Artz et al., *Computational model for oxidation-assisted rupture of ceramic matrix composites*, Pages 195-207, Copyright 2020, with permission from Elsevier.

Appendix A – Reduced Order Homogenization

In this appendix we briefly outlined the reduced order homogenization approach detailed in [11] and many others referenced herein. Consider the following small deformation boundary value problem

$$
\begin{aligned}
&\frac{\partial}{\partial x_j}\sigma_{ij}^{\xi}(\mathbf{x})+f_i(\mathbf{x})=0,\ \ \mathbf{x}\in\Omega,\\
&\sigma_{ij}^{\xi}(\mathbf{x})=L_{ijkl}^{in-\xi}(\mathbf{x})\varepsilon_{kl}^{\xi}(\mathbf{x}),\ \ \mathbf{x}\in\Omega,\\
&\varepsilon_{kl}^{\xi}(\mathbf{x})\equiv u_{(k,x_l)}^{\xi}(\mathbf{x})=\frac{1}{2}\left(\frac{\partial u_k^{\xi}(\mathbf{x})}{\partial x_l}+\frac{\partial u_l^{\xi}(\mathbf{x})}{\partial x_k}\right),\ \ \mathbf{x}\in\Omega,\\
&\mu_{kl}^{\xi}(\mathbf{x})=f(\varepsilon_{ij}^{\xi}(\mathbf{x}),\sigma_{ij}^{\xi}(\mathbf{x})),\ \ \mathbf{x}\in\Omega,\\
&u_i^{\xi}(\mathbf{x})=\tilde{u}_i(\mathbf{x}),\qquad \mathbf{x}\in\Gamma_u,\\
&n_j\sigma_{ij}^{\xi}(\mathbf{x})=\tilde{t}_i(\mathbf{x}),\qquad \mathbf{x}\in\Gamma_\sigma.
\end{aligned}
\tag{81}
$$

where Γ_u and Γ_σ are the essential and natural boundaries of the coarse-scale (macroscopic) domain Ω, respectively, satisfying $\Gamma_u\bigcap\Gamma_\sigma=\varnothing,\Gamma_u\bigcup\Gamma_\sigma=\Gamma$ (see Fig. 1). $\tilde{\mathbf{u}}(\mathbf{x})$ and $\tilde{\mathbf{t}}(\mathbf{x})$ denote prescribed displacement and traction on Γ_u and Γ_σ, respectively. $\xi>0$ is a small parameter representing characteristic size of RVE domain. $\mathbf{u}^{\xi}(\mathbf{x})$ is the displacement; $\boldsymbol{\varepsilon}^{\xi}(\mathbf{x})$ the total small strain consisting of elastic and inelastic contributions; $\boldsymbol{\mu}^{\xi}(\mathbf{x})$ the eigenstrain defined in (49); $\mathbf{f}(\mathbf{x})$ is the body force; $\mathbf{L}^{\xi}(\mathbf{x})$ denote rapidly varying elastic constitutive tensor; with $\square^{\xi}$ denoting the inclusion of multiple scales. For reduced order homogenization it is necessary to express the constitutive equation in terms of eigenstrains

$$
\sigma_{ij}^{\xi}(\mathbf{x})=L_{ijkl}^{\xi}(\mathbf{x})\left(\varepsilon_{kl}^{\xi}(\mathbf{x})-\mu_{kl}^{\xi}(\mathbf{x})\right),\ \ \mathbf{x}\in\Omega \tag{82}
$$

Assuming scale separation a local RVE coordinate $\mathbf{y} = \mathbf{x}/\xi$ is introduced, and consequently, the response functions are assumed to depend on both the slow $\mathbf{x}$ and fast $\mathbf{y}$ coordinates. An asymptotic expansion of displacements $u_i^{\xi}(\mathbf{x})$ is employed

$$u_i^{\xi}(\mathbf{x}) = u_i^c(\mathbf{x}) + \xi u_i^{(1)}(\mathbf{x},\mathbf{y}) + \xi^2 u_i^{(2)}(\mathbf{x},\mathbf{y}) + \cdots, \tag{83}$$

where $\mathbf{u}^c = \mathbf{u}^c(\mathbf{x})$ is the zeroth-order or coarse-scale displacement. Using the two-scale differential operator [10]–[14] , and assuming $L_{ijkl}^{\xi}(\mathbf{x}) = L_{ijkl}(\mathbf{y})$, the asymptotic expansion of strain and stresses are obtained. The resulting fine- and coarse-scale equations are:

$$\begin{aligned} \textit{Unit cell}: \; & -\frac{\partial}{\partial y_j}\Big(L_{ijkl}(\mathbf{y})\Big(\varepsilon_{kl}^c(\mathbf{x}) + u_{(k,y_l)}^{(1)}(\mathbf{x},\mathbf{y})\Big)\Big) \\ & + \frac{\partial}{\partial y_j}\Big(L_{ijkl}(\mathbf{y})\mu_{kl}^f(\mathbf{x},\mathbf{y})\Big) = 0, \end{aligned} \tag{84}$$

$$\begin{aligned} \textit{Coarse scale}: \; & -\frac{\partial}{\partial y_j}\Big(L_{ijkl}(\mathbf{y})\Big(u_{(k,x_l)}^{(1)}(\mathbf{x},\mathbf{y}) + u_{(k,y_l)}^{(2)}(\mathbf{x},\mathbf{y})\Big)\Big) \\ & -\frac{\partial}{\partial x_j}(L_{ijkl}(\mathbf{y})\Big(\varepsilon_{kl}^c(\mathbf{x}) + u_{(k,y_l)}^{(1)}(\mathbf{x},\mathbf{y})\Big) + \frac{\partial}{\partial x_j}\Big(L_{ijkl}(\mathbf{y})\mu_{kl}^f(\mathbf{x},\mathbf{y})\Big) = f_i(\mathbf{x}), \\ & \sigma_{ij}^f(\mathbf{x},\mathbf{y}) = L_{ijkl}(\mathbf{y})\Big(\varepsilon_{ij}^f(\mathbf{x},\mathbf{y}) - \mu_{ij}^f(\mathbf{x},\mathbf{y})\Big), \end{aligned} \tag{85}$$

For model reduction, the second term in asymptotic expansion (84) is expressed as

$$u_i^{(1)}(\mathbf{x},\mathbf{y}) = H_i^{kl}(\mathbf{y})\varepsilon_{kl}^c(\mathbf{x}) + \int_{\Theta} h_i^{kl}(\mathbf{y},\tilde{\mathbf{y}})\mu_{kl}^f(\mathbf{x},\tilde{\mathbf{y}})d\tilde{\Theta}, \tag{86}$$

where $H_i^{kl}(\mathbf{y})$ and $h_i^{kl}(\mathbf{y},\tilde{\mathbf{y}})$ are *y*-periodic zero-mean first-order influence and transformation functions, respectively, both symmetric with respect to indices *k* and *l*. The physical meaning of (86) is that a unit eigenstrain $\mu_{kl}^f(\mathbf{x},\tilde{\mathbf{y}})$ induces elastic deformation of the magnitude of $h_i^{kl}(\mathbf{y},\tilde{\mathbf{y}})$ due to volume and/or shape change at an infinitesimal neighborhood of a point $\tilde{\mathbf{y}} \in \Theta$. Further, inserting (86) into (84) yields

$$\left(\frac{\partial}{\partial y_j}\left(L_{ijkl}(\mathbf{y})\left(I_{klmn}+H^{mn}_{(k,y_l)}(\mathbf{y})\right)\right)\right)\varepsilon^c_{mn}(\mathbf{x})$$
$$+\frac{\partial}{\partial y_j}\left(L_{ijkl}(\mathbf{y})\left(\int_\Theta h^{mn}_{(k,y_l)}(\mathbf{y},\tilde{\mathbf{y}})\mu^f_{mn}(\mathbf{x},\tilde{\mathbf{y}})d\tilde{\Theta}-\mu^f_{kl}(\mathbf{x},\mathbf{y})\right)\right)=0, \tag{87}$$

where $I_{klmn}=\frac{1}{2}\left(\delta_{km}\delta_{ln}+\delta_{kn}\delta_{lm}\right)$.

Since (87) has to be satisfied for arbitrary $\varepsilon^c_{mn}(\mathbf{x})$, this yields a well-known equation for a periodic zero-mean function $H^{mn}_k(\mathbf{y})$ on the RVE domain Θ

$$\frac{\partial}{\partial y_j}\left(L_{ijkl}(\mathbf{y})E^{mn}_{kl}(\mathbf{y})\right)=0$$
$$E^{mn}_{kl}(\mathbf{y})=I_{klmn}+H^{mn}_{(k,y_l)}(\mathbf{y}) \tag{88}$$

which can be shown to have a unique solution [11].

From (87) and (88), we have the following equality for the eigenstrains

$$\frac{\partial}{\partial y_j}\left(L_{ijkl}(\mathbf{y})\left(\int_\Theta h^{mn}_{(k,y_l)}(\mathbf{y},\tilde{\mathbf{y}})\mu^f_{mn}(\mathbf{x},\tilde{\mathbf{y}})d\tilde{\Theta}-\mu^f_{kl}(\mathbf{x},\mathbf{y})\right)\right)=0 \tag{89}$$

We further define the coarse-scale stress and strain as an average of corresponding fine-scale fields over RVE domain

$$\varepsilon^c_{ij}(\mathbf{x})=\frac{1}{|\Theta|}\int_\Theta \varepsilon^f_{ij}(\mathbf{x},\mathbf{y})d\Theta$$
$$\sigma^c_{ij}(\mathbf{x})=\frac{1}{|\Theta|}\int_\Theta \sigma^f_{ij}(\mathbf{x},\mathbf{y})d\Theta \tag{90}$$

where $|\Theta|$ denotes the volume of Θ. Further, integrating (85) over Θ and combining with (86)-(90), yields the homogenized equation of the source problem (81)

$$\begin{cases} \sigma_{ij}^{c}(\mathbf{x}) = \overline{L}_{ijkl}\varepsilon_{kl}^{c}(\mathbf{x}) + \dfrac{1}{|\Theta|}\int_{\Theta} L_{ijkl}(\mathbf{y})\left(\int_{\Theta} h_{(k,y_l)}^{mn}(\mathbf{y},\tilde{\mathbf{y}})\mu_{mn}^{f}(\mathbf{x},\tilde{\mathbf{y}})d\tilde{\Theta} - \mu_{kl}^{f}(\mathbf{x},\mathbf{y})\right)d\Theta \\ \sigma_{ij,x_j}^{c}(\mathbf{x}) + f_i(\mathbf{x}) = 0, \qquad \mathbf{x} \in \Omega, \\ n_j(\mathbf{x})\sigma_{ij}^{c}(\mathbf{x}) = \tilde{t}_i(\mathbf{x}), \qquad \mathbf{x} \in \Gamma_\sigma, \\ u_i^0(\mathbf{x}) = \tilde{u}_i(\mathbf{x}), \qquad \mathbf{x} \in \Gamma_u, \end{cases} \tag{91}$$

where $\overline{\boldsymbol{L}}$ is the homogenized or overall elastic constitutive tensor, whose components are given by

$$\overline{L}_{ijmn} = \frac{1}{|\Theta|}\int_{\Theta} L_{ijkl}(\mathbf{y})E_{kl}^{mn}(\mathbf{y})d\mathbf{y}, \tag{92}$$

which can be shown to be symmetric, bounded and positive definite.

To reduce the computational complexity of solving the RVE problem the eigenstrains are approximated as

$$\mu_{ij}^{f}(\mathbf{x},\mathbf{y}) = \sum_{\alpha=1}^{M} N^{(\alpha)}(\mathbf{y})\mu_{ij}^{(\alpha)}(\mathbf{x}), \ \sum_{\alpha=1}^{M} N^{(\alpha)}(\mathbf{y}) = 1 \tag{93}$$

The partition of unity condition for the eigenstrain shape functions is satisfied by the piecewise constant approximation

$$N^{(\alpha)}(\mathbf{y}) = \begin{cases} 1, & y \in \Theta^{(\alpha)}, \\ 0, & y \notin \Theta^{(\alpha)}, \end{cases} \tag{94}$$

in which the total volume of the RVE is partitioned into M non-overlapping subdomains denoted by $\Theta^{(\alpha)}$.

Inserting (93) into (89) yields the following equality for a periodic zero-mean function $h_i^{mn(\alpha)}$:

$$L_{ijkl}(\mathbf{y})\left(h_{(k,y_l)}^{mn(\alpha)}(\mathbf{y}) - I_{klmn}^{(\alpha)}(\mathbf{y})\right)_{,y_j} = 0 \ \ \forall\, \alpha \tag{95}$$

where

$$h_i^{mn(\alpha)}(\mathbf{y}) = \int_{\Theta^{(\alpha)}} h_i^{mn}(\mathbf{y},\tilde{\mathbf{y}}) d\tilde{\Theta},$$
$$I_{klmn}^{(\alpha)}(\mathbf{y}) = \begin{cases} I_{klmn}, & \mathbf{y} \in \Theta^{(\alpha)}, \\ 0, & \text{elsewhere}, \end{cases} \tag{96}$$

Combining the above equations, the residual-free fine-scale strain field is given by

$$\varepsilon_{ij}^{f}(\mathbf{x},\mathbf{y}) = E_{ij}^{kl}(\mathbf{y})\varepsilon_{kl}^{c}(\mathbf{x}) + \int_{\Theta} h_{i,y_j}^{kl}(\mathbf{y},\tilde{\mathbf{y}})\mu_{kl}^{f}(\mathbf{x},\tilde{\mathbf{y}}) d\tilde{\Theta} \tag{97}$$

Inserting the approximation of eigenstrains (96) yields

$$\varepsilon_{ij}^{\xi_2}(\mathbf{x},\mathbf{y}) = E_{ij}^{kl}(\mathbf{y})\varepsilon_{kl}^{c}(\mathbf{x}) + \sum_{\alpha=1}^{M} h_{\left(i,y_j\right)}^{kl(\alpha)}(\mathbf{y})\mu_{kl}^{(\alpha)}(\mathbf{x}) \tag{98}$$

Further integrating (98) over partition domain $\Theta^{(\beta)}$ yields

$$\varepsilon_{ij}^{(\beta)}(\mathbf{x}) = E_{ij}^{kl(\beta)}\varepsilon_{kl}^{c}(\mathbf{x}) + \sum_{\alpha=1}^{M} h_{\left(i,y_j\right)}^{kl(\beta\alpha)}\mu_{kl}^{(\alpha)}(\mathbf{x}) \tag{99}$$

and

$$h_{ij}^{kl(\beta\alpha)} = \frac{1}{\left|\Theta^{(\beta)}\right|}\int_{\Theta^{(\beta)}} h_{\left(i,y_j\right)}^{kl(\alpha)}(\mathbf{y}) d\Theta, \;\; E_{ij}^{kl(\beta)} = I_{ijkl} + \frac{1}{\left|\Theta^{(\beta)}\right|}\int_{\Theta^{(\beta)}} H_{\left(i,y_j\right)}^{kl}(\mathbf{y}) d\Theta, \tag{100}$$

Combining (91), (92) and (93), the reduced order form of the coarse-scale stress is given by

$$\sigma_{ij}^{c}(\mathbf{x}) = \overline{L}_{ijkl}\varepsilon_{kl}^{c}(\mathbf{x}) + \sum_{\alpha=1}^{M} \overline{A}_{ijkl}^{(\alpha)}\mu_{kl}^{(\alpha)}(\mathbf{x}), \tag{101}$$

where

$$\overline{A}_{ijkl}^{(\alpha)} = \frac{1}{\Theta}\int_{\Theta} L_{ijkl}(\mathbf{y})\left(h_{\left(m,y_n\right)}^{kl(\alpha)}(\mathbf{y}) - I_{mnkl}^{(\alpha)}(\mathbf{y})\right) d\Theta. \tag{102}$$

It is convenient to rewrite (101) by defining the coarse-scale eigenstrain $\mu_{kl}^{c}(\mathbf{x})$ as

$$\mu_{kl}^{c}(\mathbf{x}) = -\sum_{\alpha=1}^{M} M_{klij}^{c}\overline{A}_{ijmn}^{(\alpha)}\mu_{mn}^{(\alpha)}(\mathbf{x}) \tag{103}$$

which together with (99)-(102) yields the coarse-scale boundary value problem

$$\begin{cases} -\dfrac{\partial}{\partial x_j}\sigma_{ij}^{c}(\mathbf{x}) = f_i(\mathbf{x}), \quad \mathbf{x}\in\Omega \\ n_j\sigma_{ij}^{c}(\mathbf{x}) = \tilde{t}_i(\mathbf{x}), \quad \mathbf{x}\in\Gamma_\sigma, \\ u_i^0(\mathbf{x}) = \tilde{u}_i(\mathbf{x}), \quad \mathbf{x}\in\Gamma_u. \end{cases} \tag{104}$$

Equations (99)-(100) together with the constitutive equations of individual phases comprise the reduced order system of equations for the independent unknowns $\varepsilon_{ij}^{(\alpha)}(\mathbf{x})$. Once the partitioned eigenstrains are determined, equations (101)-(104) are employed to update the coarse-scale fields.

Appendix B – Model Parameters

Model Parameters – S200H

Table 4 - S200H Tow Material Model Parameters

Tows	**23°C**	815°C	**1200°C**
Axial Young's Modulus (Gpa)	250.0	250.0	250.0
Transverse Young's Modulus (GPa)	98.0	98.0	98.0
Axial/Transverse Poisson's Ratio	0.053	0.053	0.053
Transverse/Transverse Poisson's Ratio	0.16	0.16	0.16
Axial/Transverse Shear Modulus (GPa)	55.0	55.0	55.0
Axial Damage Initiation Stress (MPa)	161.6	161.6	161.6
Axial Peak Strength (MPa)	1599.6	923.9	1234.2
Axial Peak Strength (MPa) – Reduced	234.4		
Axial Strain at Peak Strength	0.0064	0.0037	0.005
Axial Failure Strain	0.0065	0.0038	0.0051
Transverse Damage Initiation Stress (MPa)	167.5	174.4	167.5
Transverse Peak Strength (MPa)	413.7	334.4	413.7
Transverse Strain at Peak Strength	0.006	0.0035	0.005
Transverse Failure Strain	0.0061	0.0036	0.0051
Maximum Damage Variable Value	0.99	0.99	0.99
Axial/Transverse Shear Correction	2.0	2.0	2.0
Transverse/Transverse Shear Correction	2.0	2.0	2.0
Viscous Regularization Factor (s)	0.0015	0.0015	0.0015
Viscoplastic Yield Strength (MPa)			6.9
Viscoplastic Ultimate Strength (MPa)			2413.2
Viscoplastic Exponential Hardening			40.1
Viscoplastic Linear Hardening			6000
Viscoplastic Power Term			0.5
Viscoplastic Coefficient			0.00000000027
Viscoplastic Failure Smoothing Strength			35000
Viscoplastic Creep Failure Strain			0.00117
Oxidation Initial Mean Strength (MPa)		4630	
Oxidation Slow Crack Grown Exponent		8.7	
Oxidation A_0 ($s^{-1} \cdot \mathrm{MPa}^{-\beta} \cdot m^{-\left(\frac{\beta}{2}-1\right)}$)		0.0001956	
Oxidation Activation Energy ($\mathrm{J \cdot mol^{-1}}$)		0.00001	
Oxidation Tow Fracture Toughness ($\mathrm{MPa \cdot m^{1/2}}$)		1.4	

Table 5 - S200H Matrix Material Model Parameters

Matrix	**23°C**	815°C	**1200°C**
Young's Modulus (GPa)	108.0	108	108.0
Poisson's Ratio	0.15	0.15	0.15
Damage Initiation Stress (MPa)	124.1	187.0	62.1
Peak Strength (MPa)	166.2	161.23	75.8
Peak Strength (MPa) – Reduced	124.8		
Strain at Peak Strength	0.0112	0.009	0.0055
Failure Strain	0.0113	0.025	0.0056
Maximum Damage Variable Value	0.99	0.99	0.99
Shear Correction	2.7	2.0	2.7
Viscous Regularization Factor (s)	0.0015	0.0015	0.0015
Viscoplastic Yield Strength (MPa)			6.9
Viscoplastic Ultimate Strength (MPa)			75.8
Viscoplastic Exponential Hardening			5.1
Viscoplastic Linear Hardening			10150.0
Viscoplastic Power Term			0.7
Viscoplastic Coefficient			0.0000006
Viscoplastic Failure Smoothing Strength			35000
Viscoplastic Creep Failure Strain			0.5

Model Parameters – GEA SMI

Table 6 - GEA SMI Fiber Material Model Parameters

Fiber	23°C	1315°C
Axial Young's Modulus (Gpa)	992.8	1068.7
Transverse Young's Modulus (GPa)	179.3	137.9
Axial/Transverse Poisson's Ratio	0.05	0.05
Transverse/Transverse Poisson's Ratio	0.2	0.2
Axial/Transverse Shear Modulus (GPa)	151.7	151.7
Axial Damage Initiation Stress (MPa)	1241.0	689.5
Axial Peak Strength (MPa)	5654.5	2413.2
Axial Peak Strength (MPa) - Reduced	1241.7	
Axial Strain at Peak Strength	0.023	0.0065
Axial Failure Strain	0.025	0.0065
Transverse Damage Initiation Stress (MPa)	137.9	172.4
Transverse Peak Strength (MPa)	199.9	172.4
Transverse Peak Strength (MPa) – Reduced	117.2	
Transverse Strain at Peak Strength	0.007	0.005
Transverse Failure Strain	0.007	0.005
Maximum Damage Variable Value	0.999	0.999
Axial/Transverse Shear Correction	1.0	1.0
Transverse/Transverse Shear Correction	1.0	1.0
Viscous Regularization Factor (s)	0.0015	0.0015
Viscoplastic Yield Strength (MPa)		482.6
Viscoplastic Ultimate Strength (MPa)		1310.0
Viscoplastic Exponential Hardening		2.1
Viscoplastic Linear Hardening		60
Viscoplastic Power Term		0.4
Viscoplastic Coefficient		0.0000012
Viscoplastic Failure Smoothing Strength		52000
Viscoplastic Creep Failure Strain		0.032
Viscoplastic Fatigue Failure Strain		0.00837
Fatigue Damage Power Law Exponent		1.0

Table 7 - GEA SMI Matrix Material Model Parameters

Matrix	23°C	1315°C
Young's Modulus (GPa)	165.5	124.1
Poisson's Ratio	0.15	0.15

Damage Initiation Stress (MPa)	134.4	137.9
Peak Strength (MPa)	193.7	124.1
Strain at Peak Strength	0.029	0.012
Failure Strain	0.029	0.012
Maximum Damage Variable Value	0.999	0.999
Shear Correction	2.1	2.4
Viscous Regularization Factor (s)	0.0015	0.0015
Viscoplastic Yield Strength (MPa)		241.3
Viscoplastic Ultimate Strength (MPa)		248.2
Viscoplastic Exponential Hardening		1.1
Viscoplastic Linear Hardening		20.0
Viscoplastic Power Term		0.15
Viscoplastic Coefficient		0.00000005
Viscoplastic Failure Smoothing Strength		52000
Viscoplastic Creep Failure Strain		0.007
Viscoplastic Fatigue Failure Strain		0.007
Fatigue Damage Power Law Exponent		1.0

Table 8 - GEA SMI Fatigue Model Parameters

Fatigue	
Maximum Allowable Jump Cycles	1000
Damage Allowable per Jump Cycle	0.02
Equivalent Viscoplastic Strain Allowable per Jump Cycle	0.001